Boundary Layer Separation Control on a Salient Back-facing Ramp

Hung-Chi Wang

A thesis

submitted in partial fulfillment of the

requirements for the degree of

Master of Science

University of Washington

2021

Committee:

Dr. Robert Breidenthal, Chair

Dr. Giovanni Nino

Program Authorized to Offer Degree:

Aeronautics and Astronautics

University of Washington

Abstract

Boundary Layer Separation Control on a Salient Back-facing Ramp

Hung-Chi Wang

Chair of the Supervisory Committee:

Dr. Robert Breidenthal

Department of Aeronautics and Astronautics

The research assesses the feasibility and the performance of the serration flow control devices on a salient edge where the laminar boundary layer separation is two-dimensional. Three geometries of serrations: a sharp delta, a double delta and a divergent delta are examined on 15° and 30° deflected, backward-facing ramps. Parameterizing the device spacing and the device-height-to-chord ratio assesses the performance change with different configurations. In addition to the serration geometries, two other improvements, partitioning plates and tip treatments, are investigated. The experiments are conducted in an open-loop wind tunnel with a Reynolds number of 68,000 based on the chord of the flat plate upstream of the ramp edge. In addition to the experimental data, fluorescent oil flow visualization is used to understand the fundamentals of flow physics. This research aims to provide a structurally simpler high-lift-system solution based on the serration devices for general aviation aircraft and UAVs.

TABLE OF CONTENTS

Page

LIST OF FIGURES

Figure Number Page

NOMENCLATURE

h: Device height

c: The chord of the front plate on the ramp model

η: h/c, device height to chord ratio

d: Device base length

s: Device spacing

ξ: s/d, spacing ratio, device spacing to the device base length ratio h: device height

δ: Boundary layer thickness

r: Ramp length

The large device: $\eta = 0.16$

The medium device: $\eta = 0.08$

The small device: $\eta = 0.04$

C_l : Lift coefficient

C_d : Drag coefficient

$C_{l,n}$: Normalized C_l

$C_{d,n}$: Normalized C_d

h': Total pressure loss thickness

H_0 : free stream total pressure

P_0 : free stream static pressure

H: Local total pressure

UAV: Unmanned aerial vehicles

STOL: Short take-off and landing

VG: Vortex generator

VGJ: Vortex generator jet

AOA: Angle of attack

UV: Ultraviolet

CFD: Computational fluid dynamics

DBD: Dielectric-barrier-discharge

Plan form: The two dimensional geometry viewed from above to down

N: Newton

LEBU's: Large-eddy breakup devices

ACKNOWLEDGMENTS

I would like to gratefully acknowledge Dr. Robert E. Breidenthal for his mentoring and guidance during the course of the research and throughout my graduate academic life. I am thankful to Dr.Giovanni Nino serving as a member of my thesis committee and advising me processing the measuring data. Lastly, I want to thank my undergrad mentor, Dr. Chung-Yan “Frank” Lin. His support and encouragement help me reach this far to pursue the truth of physics.

Chapter 1

INTRODUCTION

1.1 General Background

High-lift devices are widely adopted by various fixed wing aircraft to enhance lift in take-off and landing configuration. A typical three-element, high-lift device consists of a leading edge flap, or slat, the main wing, and a trailing-edge flap. The slat and the trailing-edge flap can either work together or separately. To maximize the trailing edge flap performance, it is common to see complex Fowler or triple-slotted flaps on jet airliners along with leading-edge Krueger flaps. The major working principles of these high-lift devices are increasing wing area and injecting momentum into the trailing-edge flow, preventing it from separating from the surface. However, expensive maintenance and heavy mechanisms are the major disadvantages of those high-lift devices, preventing them from being used on smaller aircraft. Alternatively, a simple single-stage, slotted trailing-edge flap is more often deployed on commuter airliners or general aviation aircraft as a compromise of the complexity and the performance [1][2]. On ultralight aircraft, plain and Junkers flaps are essentially the only choices due to the weight requirement [3]. As the weight of the aircraft is reduced, we run out of options for good performance and cost effective, high-lift devices. The complexity of high-lift systems reached the peak around the 1960s, and then they tended to become simpler. Aircraft manufacturers and airline operators have already noticed the derivative problems of complex high lift mechanisms [1]. Many efforts have been made to increase the system efficiency. One of the most promising improvements is using vortex generators (VGs) to prevent the flow separation on the flap. Related research since the 1990's show that properly positioned VGs can dramatically increase the high-lift system performance, enabling mechanically simpler systems.

Due to its simplicity, the plain flap is a popular high lift configuration used on unmanned aerial vehicles (UAVs), ultralight aircraft and some general aviation aircraft. However, the small radius or salient edge also contributes to the main source of the performance loss (Figure 1.1). Due to the costs, many UAVs adopt simple hinge flaperons, as illustrated in Figure 1.2, which forms a salient edge when deployed. Some ultralights (i.e. Aerolite 103, SkyRanger, X-Air "F" Model) just adopt a flat panel (Figure 1.3) on the trailing edge as the flap, which also forms a salient edge when deployed. Many short-take-off-and-landing (STOL) and home-built aircraft (i.e. CH701/801, Kitfox S7) use Junkers flaperons (Figure 1.4) to satisfy both simplicity and high-lift performance, but suffer more drag in cruise. The location of boundary layer separation depends on the nature of the edge. On a salient edge, the boundary layer separation happens at the deflecting edge [4][5]. While most of the past research focused on the smooth-edge ramps to study separation control methods, only a few studies explored separation at a salient edge and how to mitigate it. This research aims to assess the devices' performance near the salient edge. Salient ramp models simulate the upper surface of a plain flap. The first question to ask is how big the device would be required to improve the flap efficiency. This will be determined by the rate of the device length to the ramp chord. To investigate the plan-form geometry's influence on the device efficiency, a sharp delta, a double delta and a divergent delta are used in the experiment. Since the devices are right next to each other, it is natural to ask how adjunct vortices interact with each other. To determine how far the vortices persist in the streamwise direction, we use fluorescent oil visualization to observe the attached distance over the ramp. The drag and lift variations are recorded to evaluate the device performance.

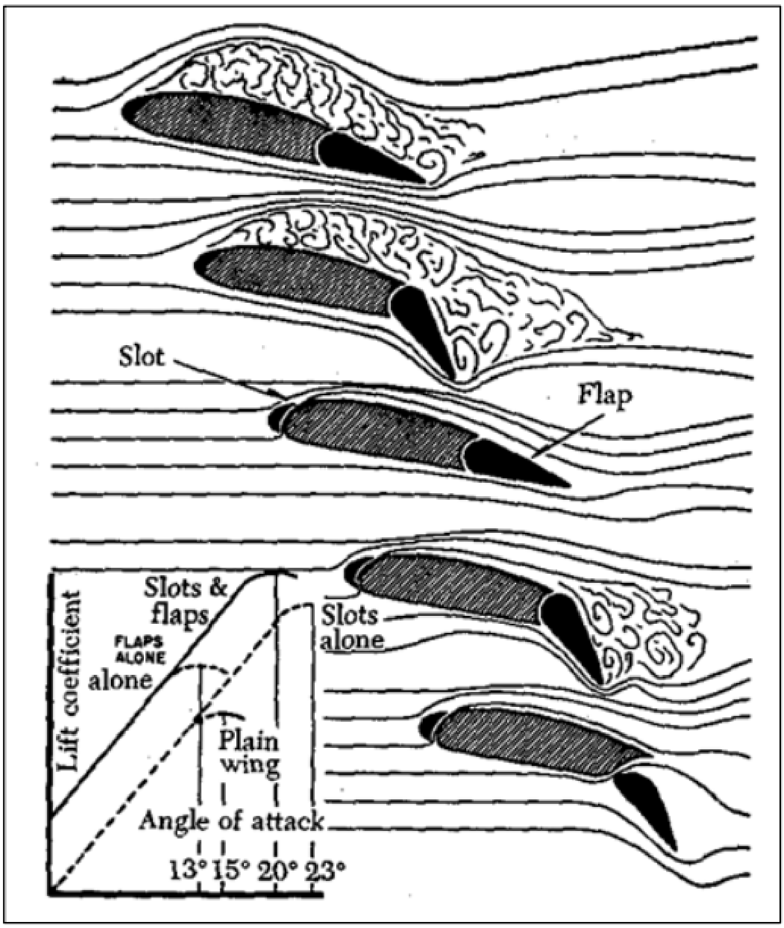

Figure 1.1: The flow conditions over the wing using difference high lift systems [6]

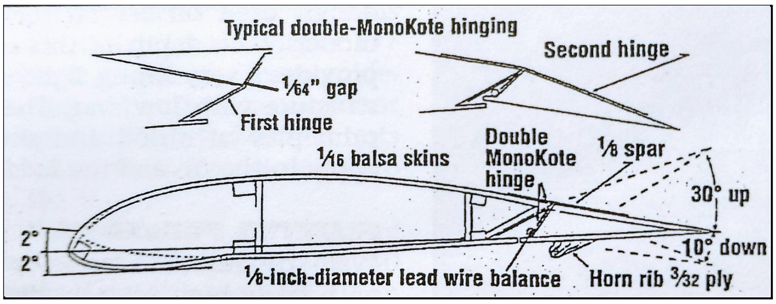

Figure 1.2: The example of a typical control surface hinging used on UAVs [7]

Figure 1.3: The SkyRanger with its plain flap deployed [8]

Figure 1.4: The Kitfox S7 with its Junkers flaperons [9]

1.2 Literature review

Extensive studies have shown that various types of VGs can significantly improve the aerodynamic efficiency[10][11][12]. Two low profile, submerged vortex generators (sub-δ VGs) were proposed by Wheeler [13][14], called Wheeler's doublet and wishbone VGs, and were later studied by Lin et al. [15]. From Lin's sketch (Figure 1.5), the flow downstream of a doublet VG shows a pair of counter-rotating streamwise vortices descending toward the surface. Similarly, the wishbone VG in laminar flow also generates a pair of counter-rotating vortices and a periodic horseshoe vortex structure. Note that there is a low momentum region in between the vortex pair for both the doublet and the wishbone vortices. We will revisit this phenomenon later in section 3.2.1. The experiments were conducted in a low-speed wind tunnel. The height of the wishbone VGs was 0.2δ (δ is boundary layer thickness). The VGs were placed 2δ upstream of the separation point on a backward-facing ramp.

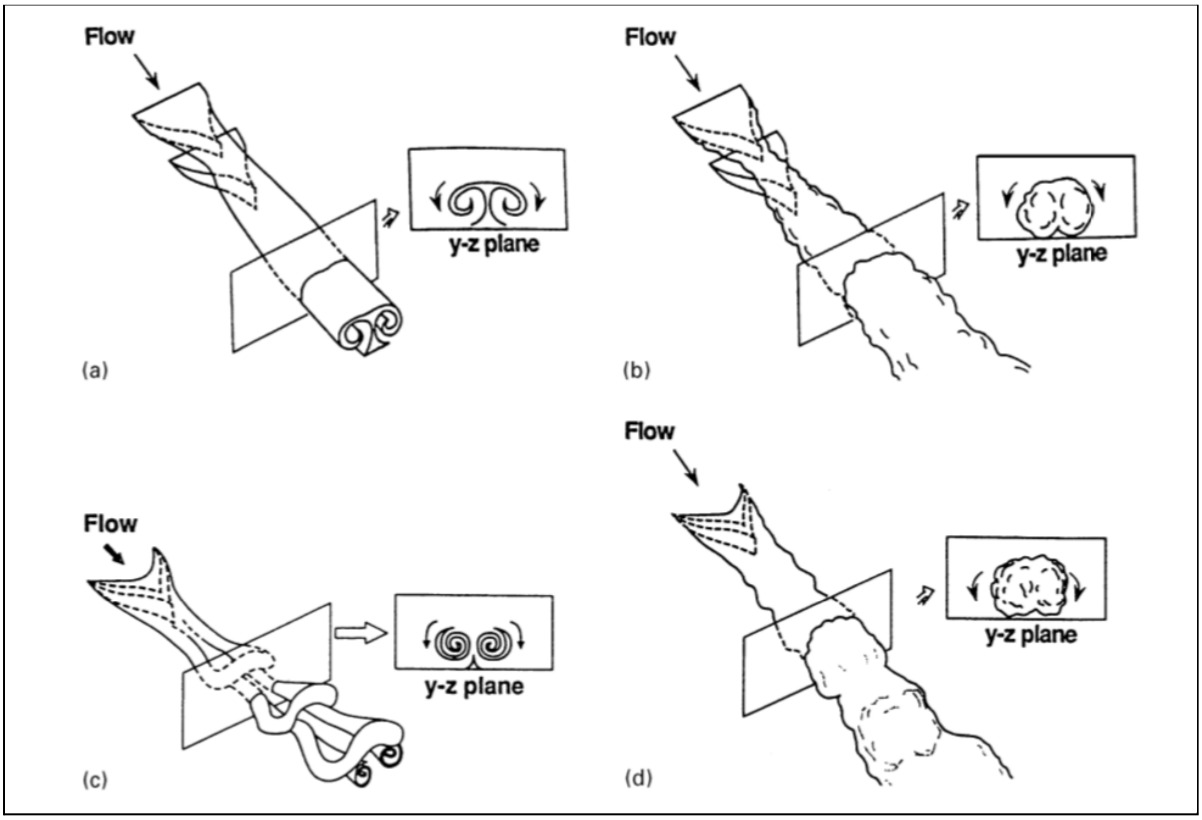

Figure 1.5: The vortex structures of wishbone and doublet VGs under laminar and turbulent flows [15]

Lin conducted a series of tests on a 0.71 m (28”) width backward-facing ramp with a 25° deflection angle (Figure 1.6) [16]. The ramp used in the experiment has a rounded shoulder of 0.20 m (8”) radius. The model produced reasonably two-dimensional boundary layer separation. The boundary layer ahead of the ramp was verified to be fully turbulent. The boundary layer thickness (δ) is 32.51 mm (1.28”) ± 1.7%, and the momentum thickness is 3.43 mm (0.135”). The Reynolds number based on the momentum thickness is about 9100. The research investigated many methods and devices for the boundary layer separation control, including: a passive porous surface, longitudinal, transverse, & swept grooves, longitudinal riblets, the sub-δ VG, δ-scale vortex generators (δ-scale VGs), vortex generator jets (VGJs), Viets’ fluid flappers, arches**,** large-eddy breakup devices (LEBU’s), spanwise cylinders, Helmholtz resonators and surface cooing. Beside the experiments conducted in the NASA Langley 0.51 m by 0.71 m (20” by 28”) Shear Flow Control Tunnel, Lin also investigated some devices in the NASA Langley 0.41 m by 0.61 m (16” by 24”) Water Tunnel to perform the dye-flow visualization studying. We mainly focus on the results of the passive sub-δ VGs and the δ-scale VGs. The author placed different sizes of sub-δ VG (h/δ= 0.1, 0.2, 0.4, 0.8) and δ-scale VGs in front of the shouldered ramp, on a flat surface. The device distance to the streamwise baseline separation location varies between different devices. The pressure distribution and oil flow visualization were documented to analyze the device performance. The results show that generally the VGs have better performance of pressure recovery if the device is closer to the stream-wise baseline separation location. The author also pointed out that the submerged vortex generators such as doublet, wishbone, and vane-type with h/δ= 0.1 to 0.2 have effective separation control performance located at between 5 to 10 device height (h) upstream of separation. If properly placed, those configurations perform almost as well as δ-scale vortex generators with h = δ. Vane-type vortex generators with h about 0.2 δ reduced the extent of separation by almost 90%. The passive VGs work almost as well as the active VGJs in terms of reduction in stream-wise separation region and delaying the flow separation.

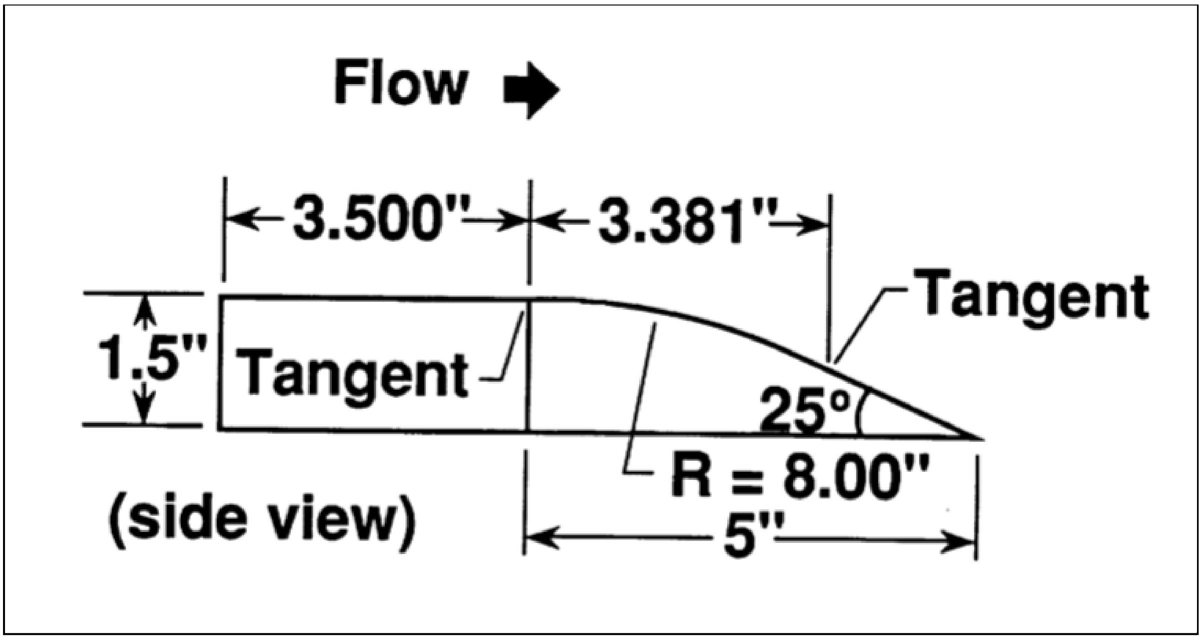

Figure 1.6: The ramp used in Lin's experiment [16]

Research at near flight conditions by Lin et al. found that the micro vortex generators placed on the proper position of the trailing edge flap can effectively increase trailing edge flap lift-to-drag ratio and reduce drag [17]. A narrow-body aircraft model was placed in a low-speed wind tunnel at M= 0.20, Reynolds numbers 5×10^6 and 9×10^6 for testing. A two-dimensional, single slotted flap and a three-element high-lift system were examined with counter-rotating and co-rotating vane-type VGs. Two vane geometries, delta and trapezoidal, on sub-δ VGs were mounted at 19%, 25%, and 33% of the flap chord locations . The flap angle was set at 35°s. It was found that the sub-δ VGs have optimum performance at streamwise locations of 25% and 33% of the chord, relatively close to the baseline separation at 45%. This result is in accord with Lin's previous research in 1992 [16]. Co-rotating VGs persisted longer in the streamwise direction than the counter-rotating ones. The results show that trapezoidal sub-δ VGs can increase the lift-to-drag ratio by 80%, with a 10% increase in lift, and a 40% reduction in drag. Furthermore, adding sub-δ VGs will not have a detrimental effect on the region where the flow is already attached. One fact that Lin does not particularly bring up is the 0.1" h (h is device height) co-rotating VGs showed much less performance improvement than the 0.04" h placed at the same 19% flap chord location.

Jukes and Choi used dielectric-barrier-discharge (DBD) VGs to control boundary layer separation on a 20° deflecting flat panel in low Reynolds number (90×10^3 and 700×10^3) laminar flow [18]. Instead of a rounded edge in Lin's research in 1992, the flap has a salient edge connecting to the upstream flat plate (Figure 1.7).

The DBD vortex VGs were placed about 75 mm upstream from the salient edge. The results show that both counter-rotating and co-rotating DBD vortex generators are effective in attenuating flow separation on the backward-facing ramp, provided that the spacing of the vortex generators and plasma-induced velocity are properly set. Even if the plasma-to-freestream velocity ratio is as low as 7%, the separation control is still achievable by using counter-rotating DBD vortex generators. Many studies of active VG control over a back-facing ramp have been done, but active control is generally out of the scope of the thesis research.

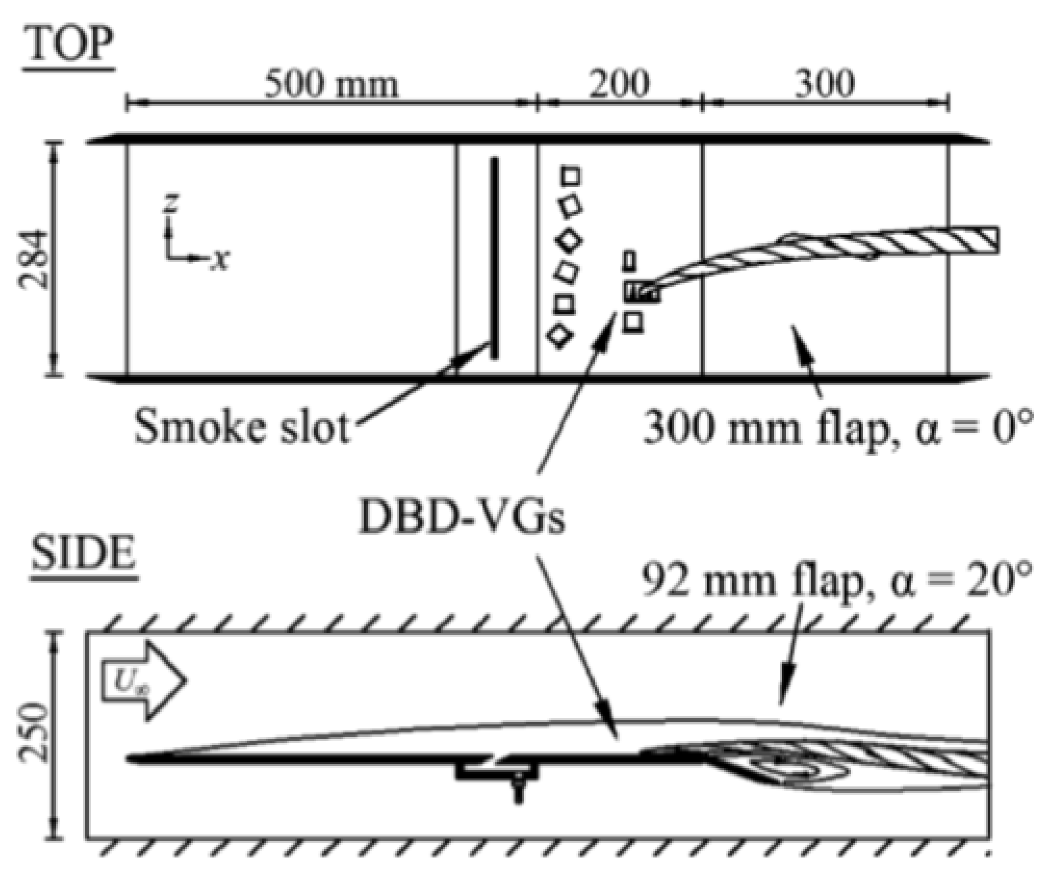

Figure 1.7: The ramp used in Jukes and Choi's experiment [18]

Kourta et al. tested a flat-top model with a 25° backward-facing ramp with incident laminar boundary layer (Figure 1.8) [19]. The Reynolds number of the ramp height is 1.85×10^5. The result shows that the separation bubble extends downstream of the coordinate origin shown in Figure 1.8 about twice the ramp length, corresponding to about six times the ramp height. From this result, we have a general idea how big the separation bubble would be, and we want to reduce the size of the separation region.

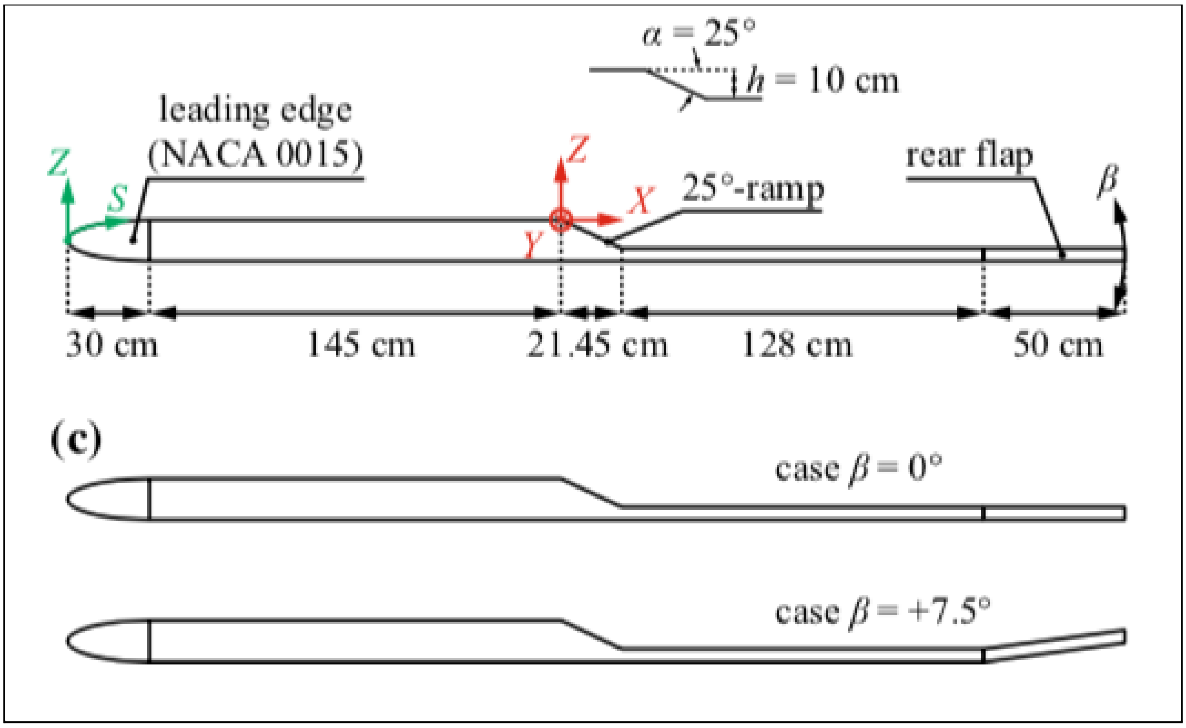

Figure 1.8: The ramp used in Kourta et al.'s experiment [19]

During the preliminary experiments of this thesis research, it was found that the serrations at the salient edge can serve as an effective device to re-invigorate the momentum of the flow on the ramp surface. The serrations are sawtooth-like geometry extending out of the straight-trailing edge of wing sections. In this thesis research, the serrations are extending out of the straight-salient edge of the ramp. There is much research related to trailing-edge serrations on airfoil sections that have revealed the aerodynamic and aeroacoustic benefits [20][21][22][23][24]. The improvement depends on the type of airfoil and the geometry of the serrations. It has been observed that the flow from the pressure side of the airfoil passes through the serration valleys to the suction side forming tornado-like vortices jet stream toward the downstream. This significantly reduces the wake thickness [25].

Liu et al. conducted experiments and computational fluid dynamics (CFD) simulations of sawtooth and slotted-sawtooth serrations on NACA 65(12)-10 and NACA 0012 airfoils (Figure 1.9) [25]. The Reynolds numbers based on the chord length of the airfoil were 3×10^5 and 5×10^5, corresponding to flow velocities 30 m/s and 50 m/s, respectively. For the sawtooth serrations case, the experimental results of both NACA 0012 and NACA 65(12)-10 airfoils present a reduction in lift coefficient up to 15% for angle of attack (AOA) ranging from $-5°$ to $10°$ comparing to the baseline airfoils (with straight trailing edge). The slotted-sawtooth serrations show greater reduction in lift coefficient up to 30%, but both types of serrations generate more lift than the blunt trailing edge cases.

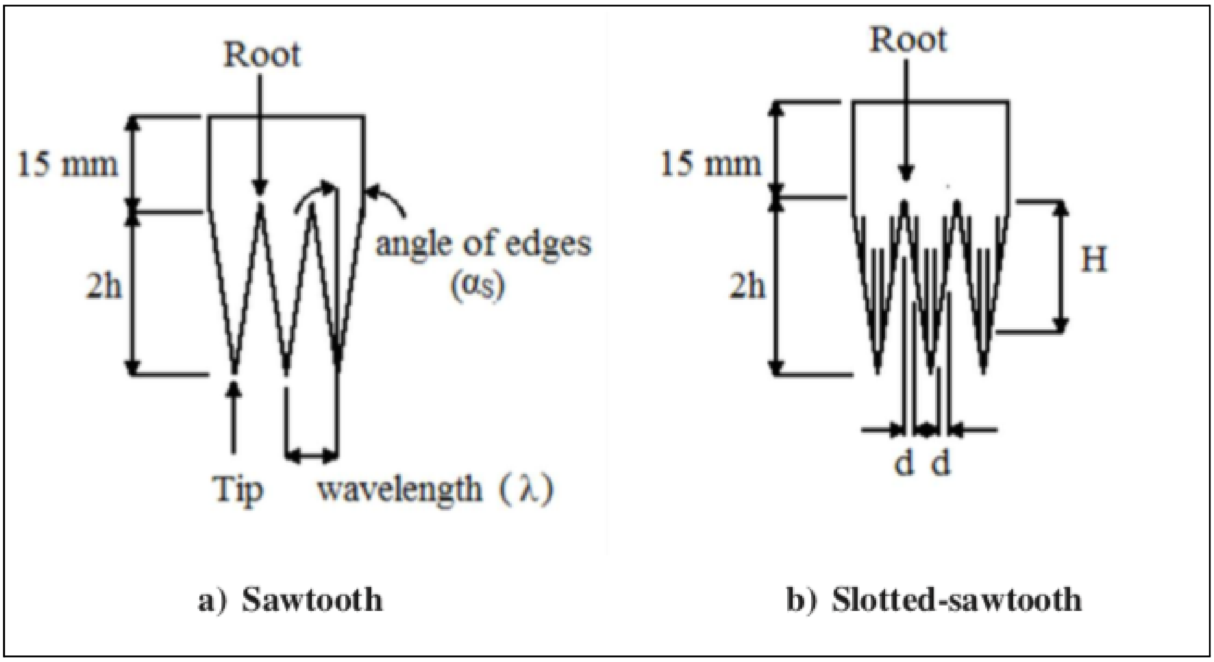

Figure 1.9: The serration plan forms used in Liu et al.'s experiment [25]

While most of the trailing-edge serration research has focused on the wake and noise reduction for turbine blades or aircraft wings, there is no known literature that specifically applies this technique on ramp boundary layer separation control. We can roughly borrow the concept of forming the vortices by the flow passing through the serration valleys from the pressure side to the suction side, but the suction side in our case is stationary airmass. According to Dr. Breidenthal's analogy [26], it seems the NACA duct is a better existing reference for us. The analogy is that the serrations act like many NACA ducts. The vortices forming on both sides of the serrations pump the airmass near the ramp surface (Figure 1.10). This leads to further improving methods that adopt the NACA ducts' features to optimize the serration efficiency.

A NACA duct, or also known as a NACA inlet or NACA scoop, is a submerged, low-drag air inlet. It was originally developed by the U.S. National Advisory Committee for Aeronautics (NACA) for the state-of-the-art jet fighter projects [27][28][29]. During the 1940's and 50's, many experiments were conducted related to this subject, but it was soon no longer of interest until the 1990's. With the progress of CFD algorithms and the improving hardware capability, many numerical efforts revisited this subject, and some improvements were proposed with the help of additional VGs [30]. Nowadays, a NACA duct is commonly used on automobiles or on aircraft serving as auxiliary air inlets.

A typical NACA duct consists of a deflected ramp submerging into the surface with an opening entrance at the end of the ramp. The ramp is bounded by divergent walls. The wall faces are generally but not always perpendicular to the ramp floor. We will later discuss this detail when we talk about Figure 1.14. Some terminologies are worthy to carefully illustrate here. Two important parameters are related to the performance of the duct. First, we define the *maximum pressure recovery coefficient*, or the *ram recovery ratio*, as the duct-entrance total pressure minus free-stream static pressure over the freestream dynamic pressure. The second parameter is the *velocity ratio*, which is the duct-entrance flow velocity over the freestream flow velocity. If we look at the ramp from the top with our view perpendicular to the surface, the top view of the ramp floor is called the *ramp plan form* (Figure 1.11). The width of the entrance over its submerging depth is defined as *width-to-depth ratio*. The angle between the ramp floor to the surface is *ramp angle*. If we look at the duct from the side view, the side view of a NACA duct is called the *ramp floor shape*, or the *ramp profile* (Figure 1.11). In combination with the curved diverging ramp plan form, the straight ramp profile works better to gain higher pressure recovery [27]. On the top of the entrance, closing the opening is called the *lip*. It is a flap plate with rounded leading edge or airfoil-like shapes. Frick et al. tested different lip configurations in 1945. On the top of the ramp walls, we can place small ridges or deflectors to increase the inlet-velocity ratio and the maximum pressure recovery coefficient [31]. We call this extruded device the *deflector plate* (Figure 1.12). Besides improving the performance, tests indicated that deflectors can be used to avoid flow separation if the center-line of the duct system is disturbed by the near flow field [28].

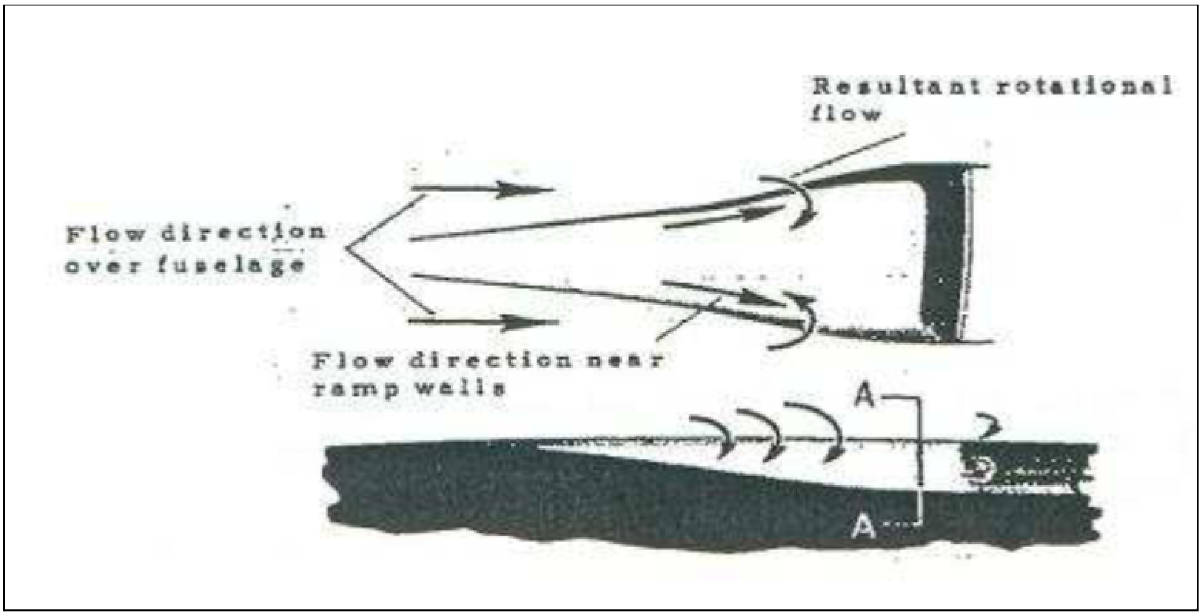

Figure 1.10: The flow structure of a typical NACA duct [29]

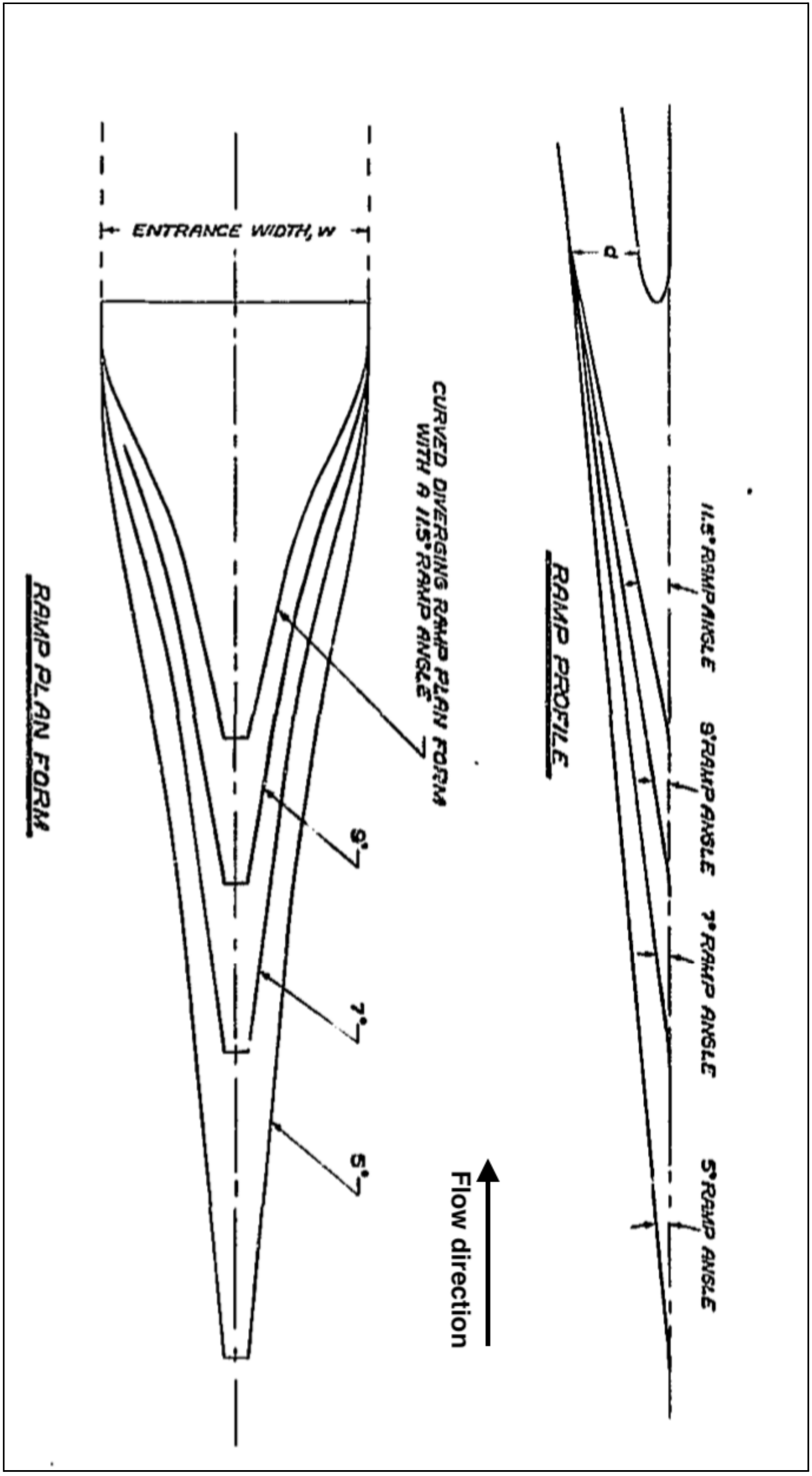

Figure 1.11: The top and side view of a typical NACA duct [27]

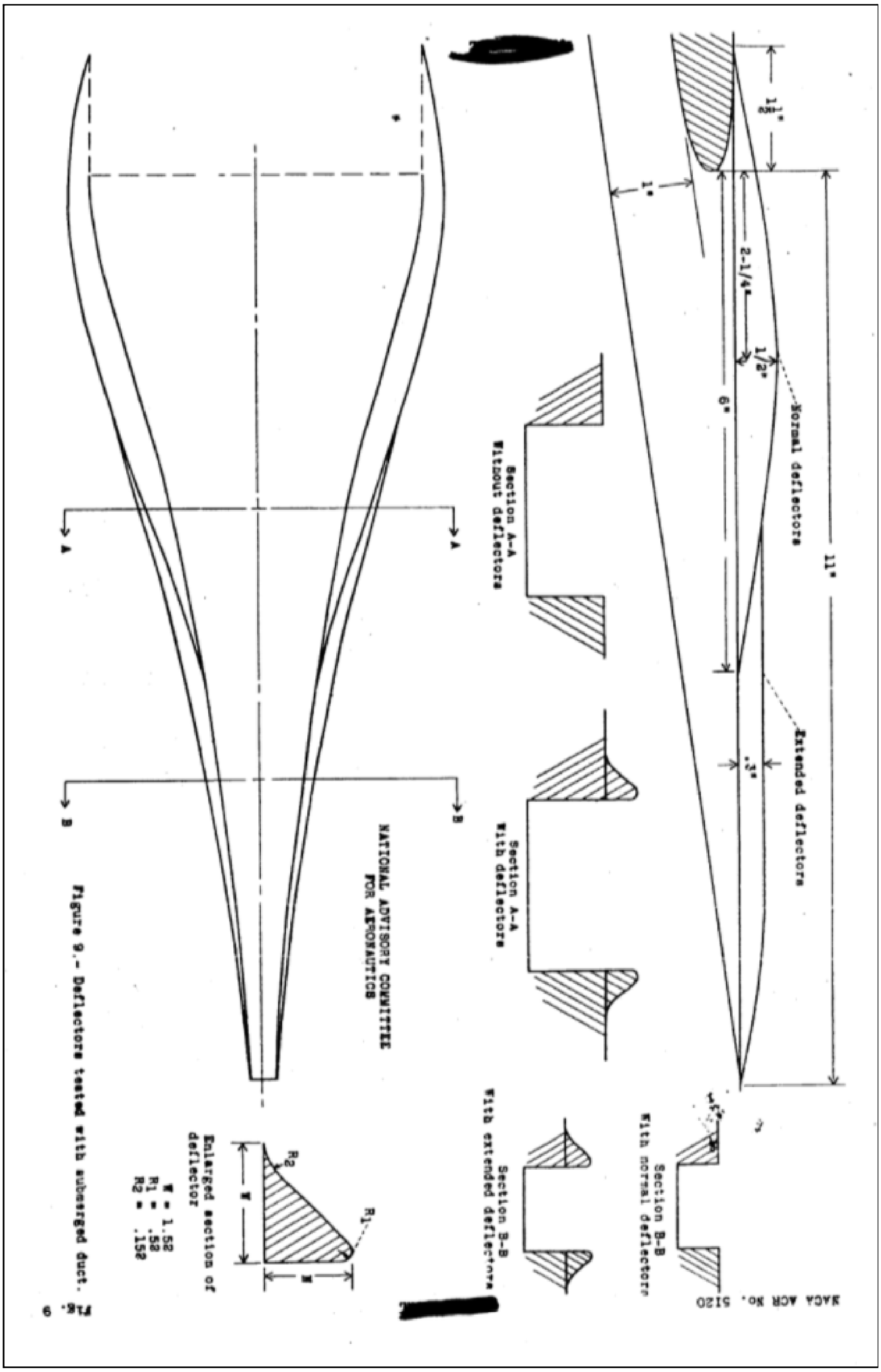

Figure 1.12: The deflector plate mounted on a typical NACA duct [31]

In the early stage of NACA duct development, the wall was designed as a pair of parallel straight style. The ramp plan form looks like a rectangular shape as the "divergence = 0.0" shown in Figure 1.13. However, the pressure recovery was disappointingly low, with a maximum value of only 57%. Later it was found that with a divergent ramp plan form (the case no. 4 showing in Figure 1.13), the best pressure recovery can be obtained of about 78% at an inlet velocity ratio of 0.4 [31]. Furthermore, the divergent ramp planform works better at higher Mach numbers than the parallel walls, with higher pressure recovery. This is due to the difference of the boundary layer characteristics over the ramp. The three-dimensional flow through the divergent walls has a slower boundary layer accumulation over the ramp surface. Compared to the quasi-two-dimensional flow in the parallel walls case, the inlet tends to ingest a thicker boundary layer [27]. Besides modifying the ramp plan form to increase the inlet performance, Taylor proposed a divergent wall concept shown in Figure 1.14. Instead of placing the walls perpendicular to the ramp surface, the modified walls are 134° and 146° away from the ramp surface. As Figure 1.14 indicates, the inlet will ingest less boundary layer at the corners [32].

It has been found that the optimal combination of a NACA duct employs curved diverging ramp plan form, 5° to 7° ramp angle and 3 to 5 width to depth ratio. It is also pointed out that the intersection of the upper ramp walls and the outer flat surface has to be done in a sharp and crisp manner, facilitating the generation of vortex sheets along the ramp walls [27][33]. The boundary layer thickness has a significant influence on the duct performance. The thicker the boundary layer, the less the pressure recovery for all configurations. A correlation factor of the change in pressure recovery to the change in boundary layer thickness was set up to calculate the approximation of the pressure recovery loss. The total pressure loss thickness h' is the height that contains the amount of free stream total pressure loss in the boundary layer, and therefore the free stream dynamic pressure (H_o - P_o) times h is the total pressure that could be lost in the boundary layer. h' can be expressed as:

$$h' = \int_0^{\delta} \frac{\Delta H}{H_0 - P_0}\, dy$$

The change in ram recovery ratio due to the change in the boundary layer thickness can be formulated as:

$$\Delta\left(\frac{H - P_0}{H_0 - P_0}\right) = \left(\frac{H - P_0}{H_0 - P_0}\right)_a - \left(\frac{H - P_0}{H_0 - P_0}\right)_b$$

In Mossman's experiments, the total pressure thickness of the natural boundary layer was 5.77 mm (0.227"), and 13.46 mm (0.530") for the thick boundary layer [27]. With the velocity ratio of 0.4 to 1.2 and the duct entrance width-to-depth ratio of 2.0 to 6.0, the pressure recovery loss coefficient was about 0.10 to 0.12. The calculation of the approximated pressure recovery loss has about 2% deviation from the measured data [27]. In conclusion, there are five important factors influencing the performance of a NACA duct: They are the duct entrance width-to-depth ratio, ramp plan form, ramp angle, deflector plate and the boundary layer thickness.

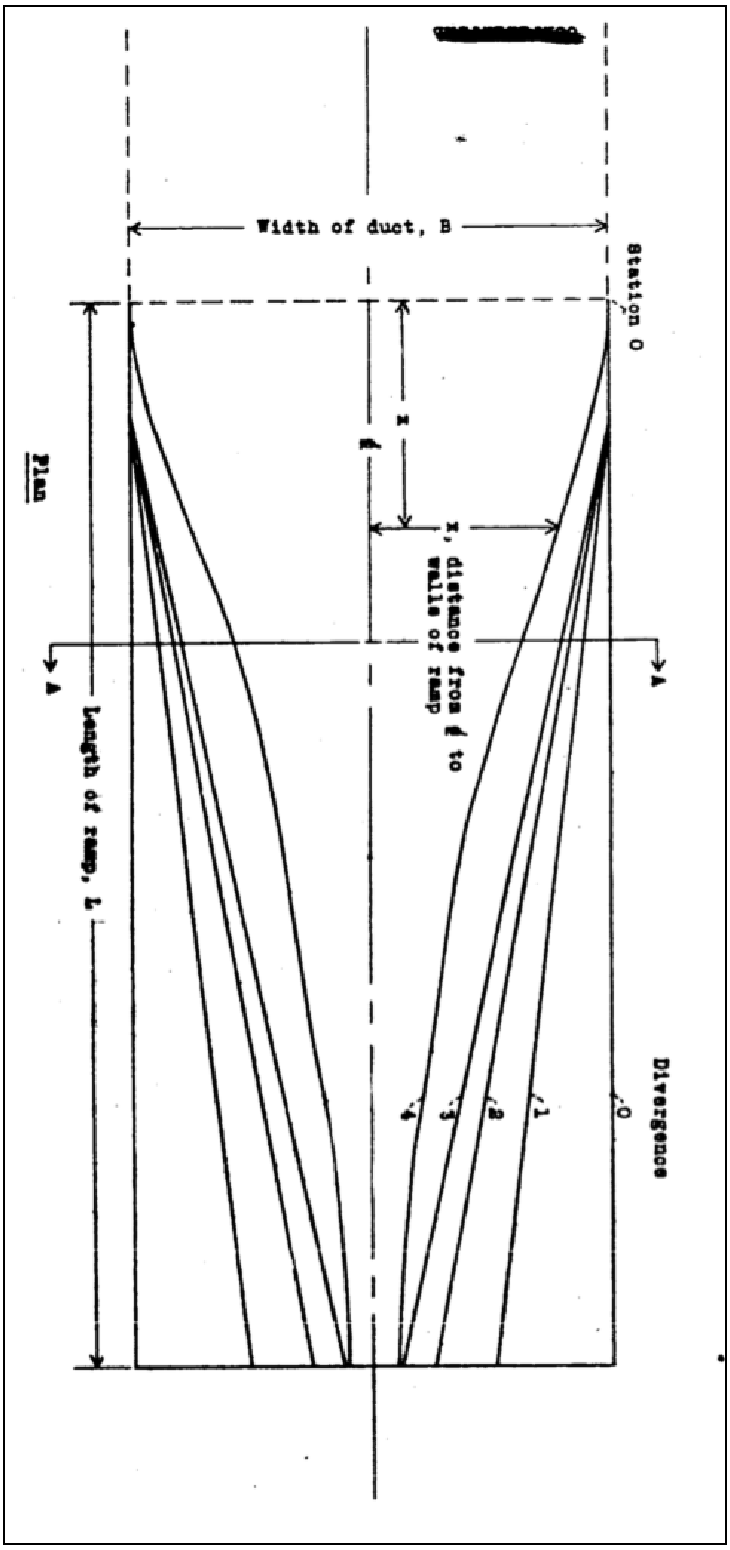

Figure 1.13: Different plan forms of NACA duct design

(from divergence = 0.0 to 0.4) [31]

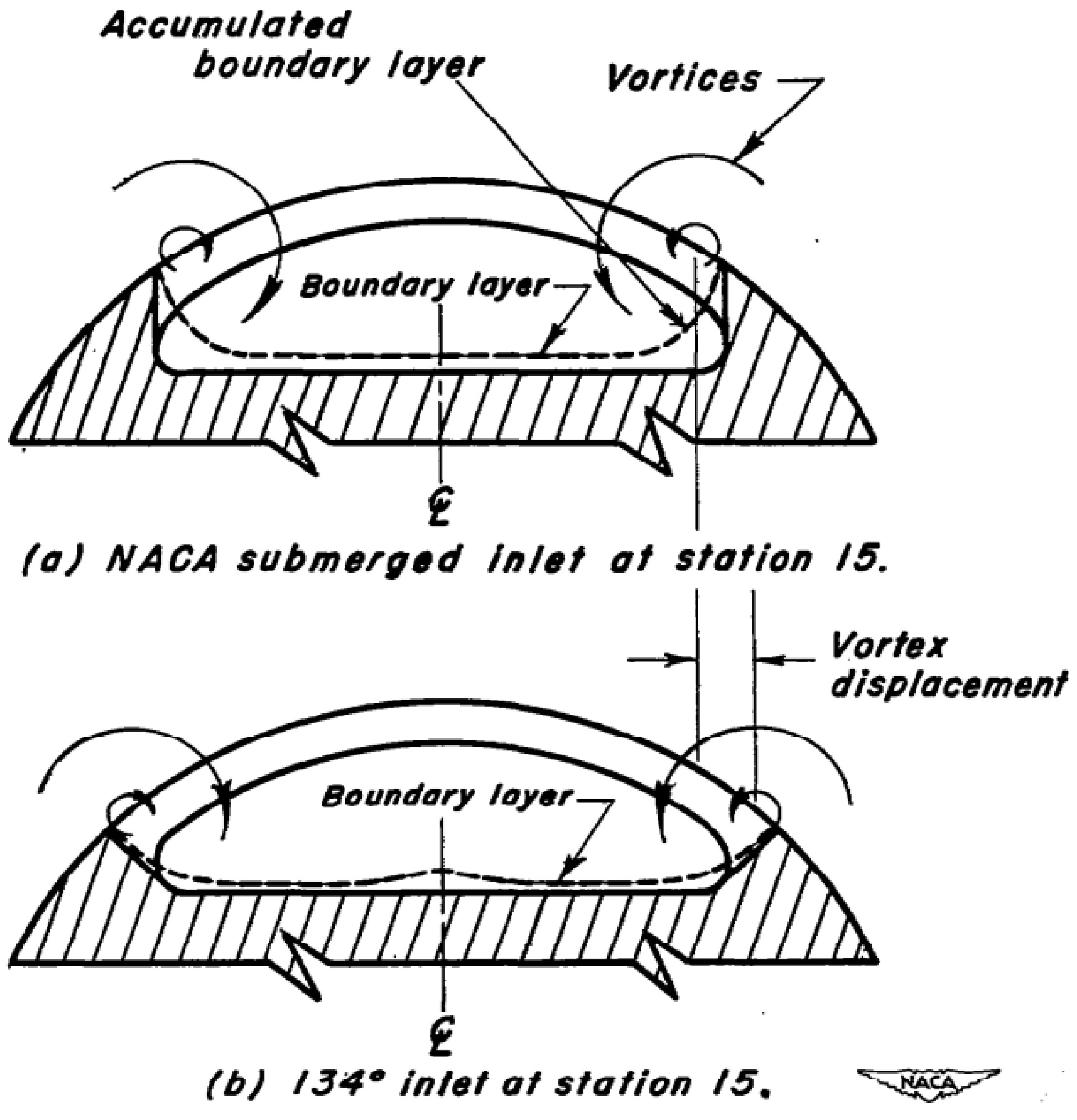

Figure 1.14: a) The typical NACA duct with 90° ramp walls, b) the divergent ramp walls [32]

1.3 Research Objective

From the existing literature, the pair of counter-rotating vortices seems to have great potential to re-invigorate the boundary layer over the trailing-edge flap. This research pursues the serrations over the salient edge of the ramp to explore the performance of the devices. The principal objectives of this study are to investigate 1) the effective size of the devices, 2) the interaction of the adjunct vortices, 3) the shape of the devices, and 4) the flow physics downstream of the devices. For the first three, we would like to know how these parameters influence the performance of any given airfoil section. Two simple backward-facing ramps with a flat plate in front of the ramp edge are used in substitute of the two-dimensional wing section with the high-lift system in the research. The maximum C_l variation and lift-to-drag ratio variation are the main performance indicators.

In the following content, we treat each of the individual serraiton (i.e. a tooth of the "sawtooth" serrations) as a device. The device length (h) to the flat plate chord (c) ratio is defined as $\eta = h/c$, with values of 0.16, 0.08, and 0.04 in this study (Figure 1.15). From previous research, we know that the interaction of downstream vortices is a function of VG spacing and vortex rotation direction [17]. To mathematically express the device spacing, we define the non-dimensional ratio $\xi = s/d$, where s is the separation between adjunct devices and d is width of the base of the device (Figure 1.15). Values explored are ξ = 0.00, 0.25, 0.5, 0.75, and 1.00. The geometry of devices could play such an important role in generating vortices. Three shapes are chosen in this investigation: They are a) sharp delta, b) double delta, and c) divergent delta, shown in Figure 1.16.

Engine oil mixed with ultraviolet (UV) dye will be used to observe the flow physics over the ramp with and without the devices. We would like to know how far vortices persist in the streamwise direction and the pattern of the downstream flow. Denote the ramp length as r.

In comparison to the NACA duct analogy, we add a partitioning plate along the centerline of a divergent delta serration, underneath the serration (Figure 1.17), and therefore each serration looks much like an individual duct. The correlation of the serrating device parameters to the NACA duct parameters is as follows: 1) ξ and the ramp angle determine the entrance width-to-depth ratio, 2) the duct ramp angle determines the optimal deflection angle of the flap, 3) η and the device shapes determine the ramp planform. We use these relationships to optimize our device by adapting the research results for the NACA duct.

During the course of the study, it was found that a pair of vortices forms along the edge of the serrations and eventually collide with each other near the tips. This phenomenon creates a strong stagnation point near the tip and wastes flow energy. In addition to the partitioning plate method, two tip treatments of serrations are also investigated on sharp delta serrations to assess the performance reducing the stagnation realm (Figure 1.18).

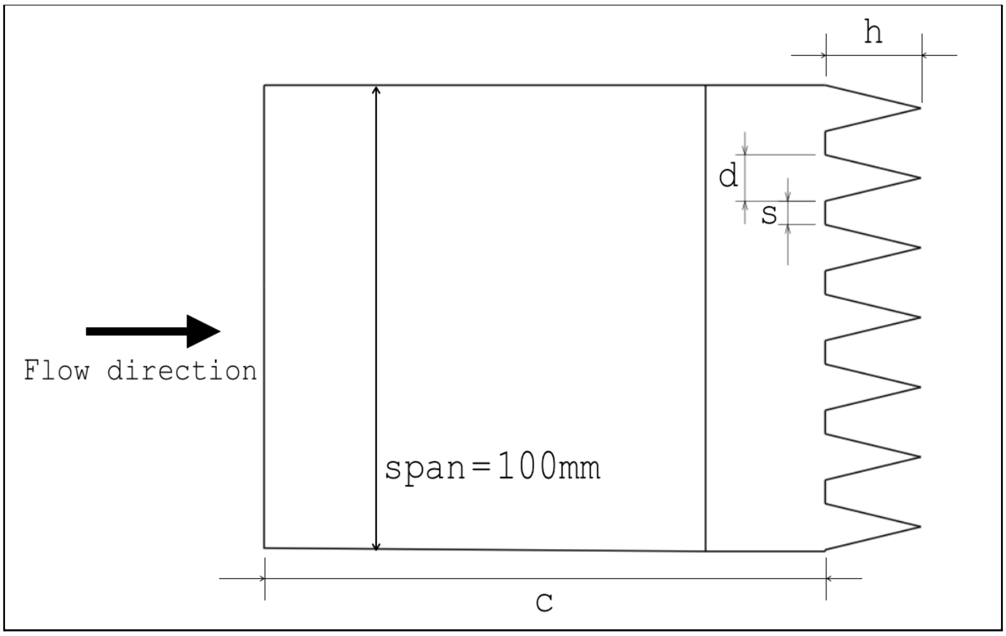

Figure 1.15: The definition of geometrical parameters

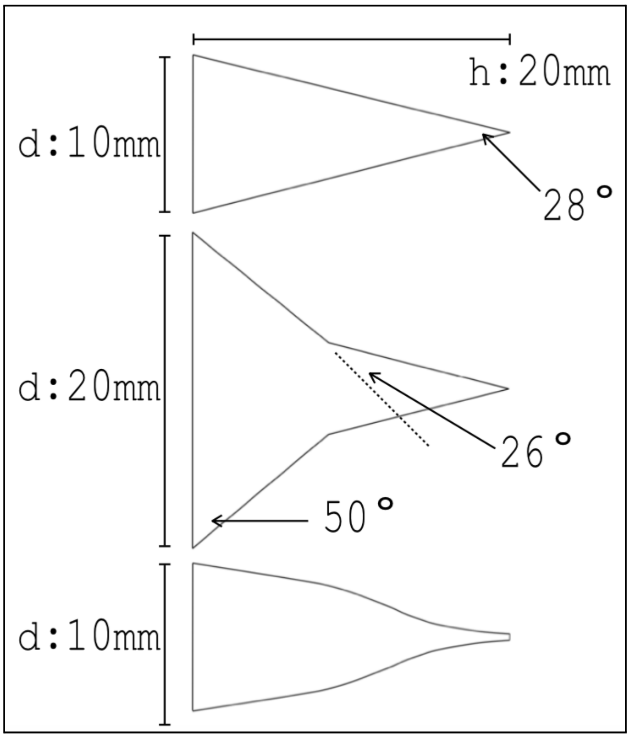

Figure 1.16: The plan form of the serrations. From the top to down is sharp delta, double delta and divergent delta.

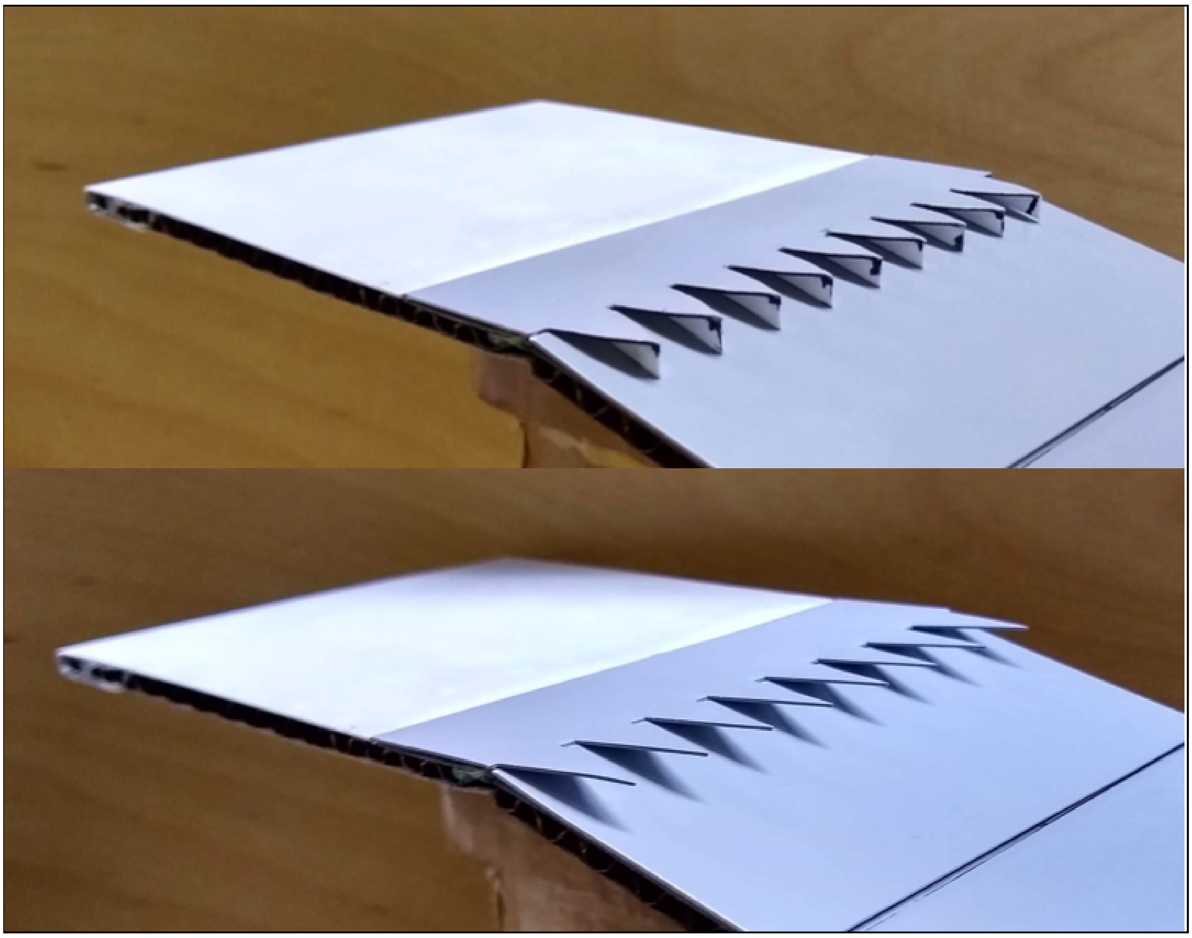

Figure 1.17: Serrations with partitioning plates (top) and serrations without partitioning plates (down)

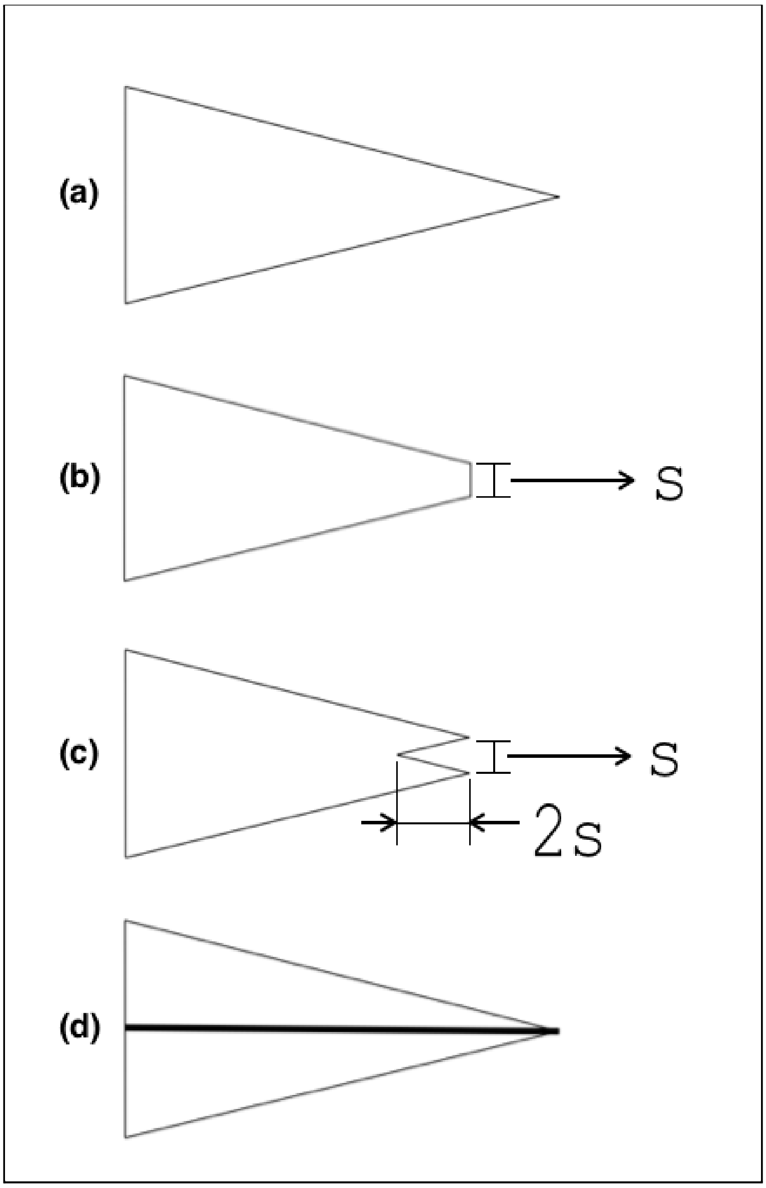

Figure 1.18: The configurations of tip treatment. a) the regular sharp delta device, b) the cut-tip treatment, c) the slotted-tip treatment, d) the sharp delta device with partitioning plate

Chapter 2

EXPERIMENTAL APPARATUS AND TESTS

2.1 Test facilities

The wind tunnel used in the research is an open loop, low-speed, mini wind tunnel with a cross section of 0.102 m by 102 m and the top speed of 8.5 m/s (Figure 2.1). The wind tunnel is powered by a VORNADO circulator fan and a TerraBloom booster fan mounted in series. The flow angularity has been checked by using a flat plate with rounded leading edge and 0° of AOA. By connecting the flat plate to a force balance, we can measure how much additional lift and drag need to be taken out or to be added in the latter experiments testing different serrations. Two ramps with 15° and 30° deflection will be placed 0.30 m downstream of the end of the tunnel converging inlet. The breadth of the flat plate on the ramp models to the wind tunnel floor is 40 mm. The Reynolds number based on the flat plate in front of the ramp is 68,000. Using the laminar boundary layer thickness equation, the thickness is estimated to be about 2.5mm at the salient edge [34].

$$\delta = \frac{5.2x}{\sqrt{Re_x}}$$

Since the ramp creates an asymmetric divergent flow path behind the flat plate, it is important to make sure that no boundary layer separation happens on the wind tunnel ceiling. Before formally starting the experiments, all devices have been tested in the wind tunnel and used mini tufts attached on the ceiling along the salient edge location to check the boundary layer condition. No separation was observed on the ceiling.

The force balance is made by a KUBEI electronic scale with a weighting range of 0.01 N ~ 29.40 N and a "L" shape fixture to support the scale (Figure 2.2, Figure 2.3, Figure 2.4). The electronic scale is positioned on one side of the L-shape fixture with two perpendicular walls. When the lift was measured, the stainless steel platform of the scale is facing up, perpendicular to the flow direction. The fixture was flipped 90°s when measured the drag, using the other wall of the fixture against the table to support the scale. Each ramp has a linkage extended out of the wind tunnel floor. An adapter connects the linkage and the scale using hot glue (Figure 2.5), and the magnets on the adapter connect to the electronic scale's platform. The magnets were checked to be able to lift five times more than the maximum force measured throughout the experiments, and the magnetic force doesn't cause any interference to the load cell under the platform. The force balance is shown in Figure 2.6, Figure 2.7 and Figure 2.8.

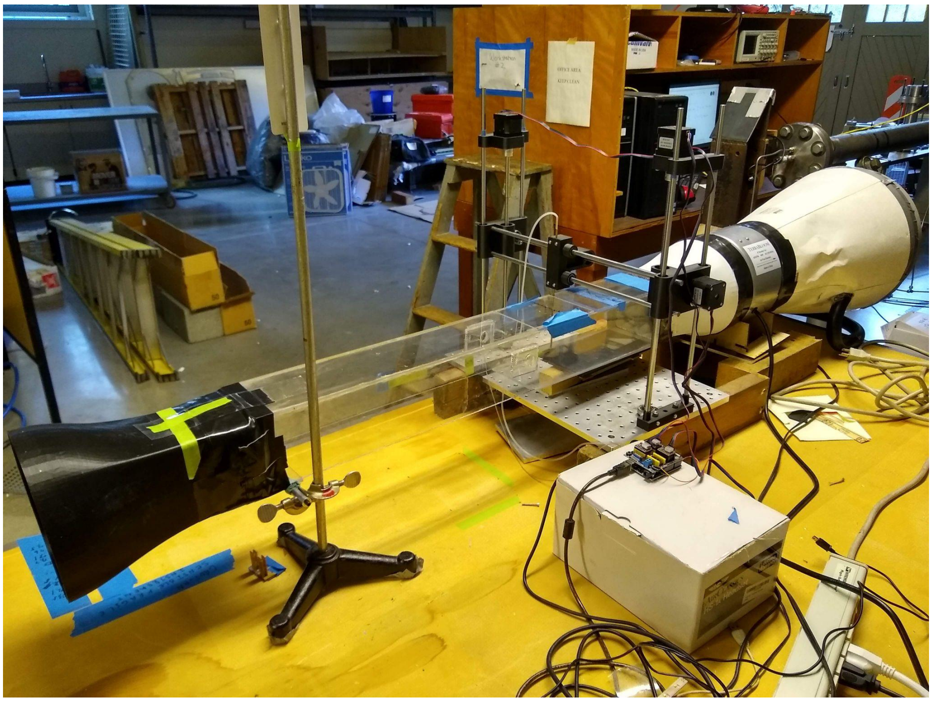

Figure 2.1: The mini wind tunnel

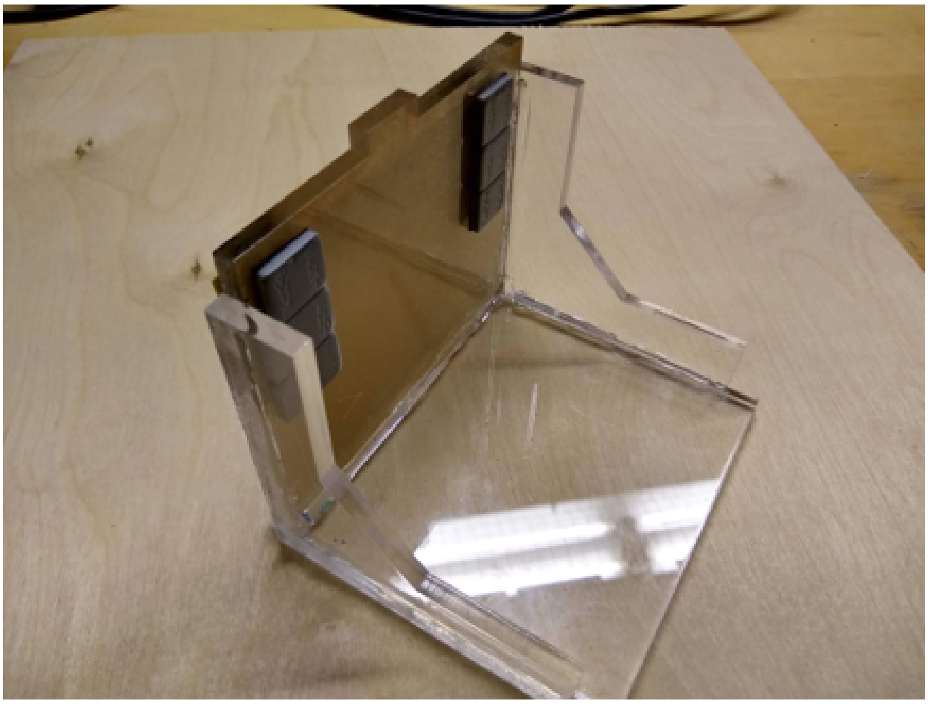

Figure 2.2: The L-shape fixture

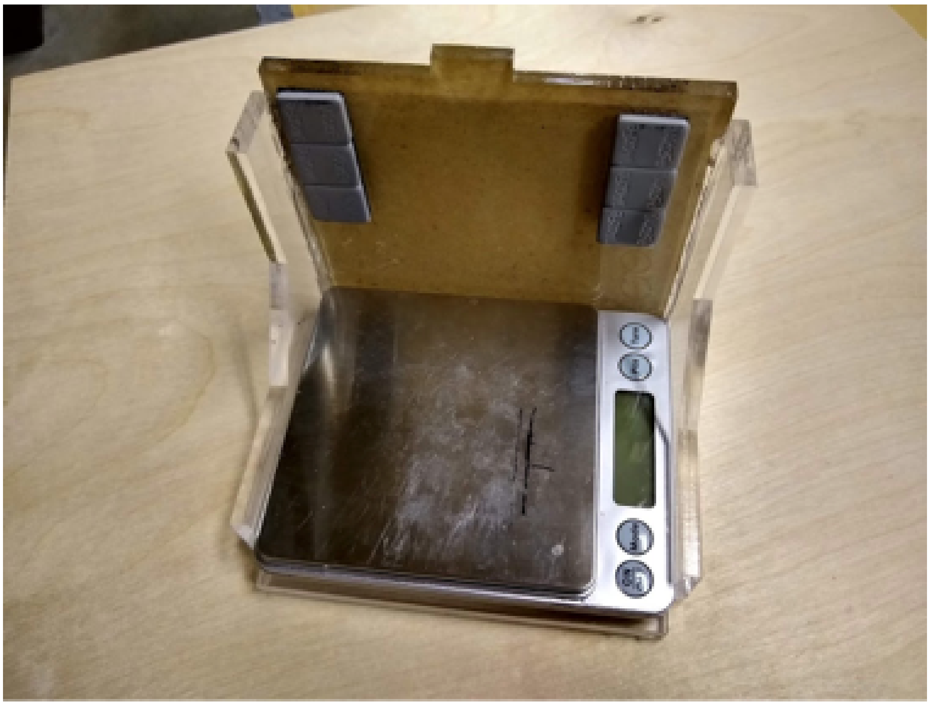

Figure 2.3: The L-shape fixture under lift-measuring configuration

Figure 2.4: The L-shape fixture under drag-measuring configuration

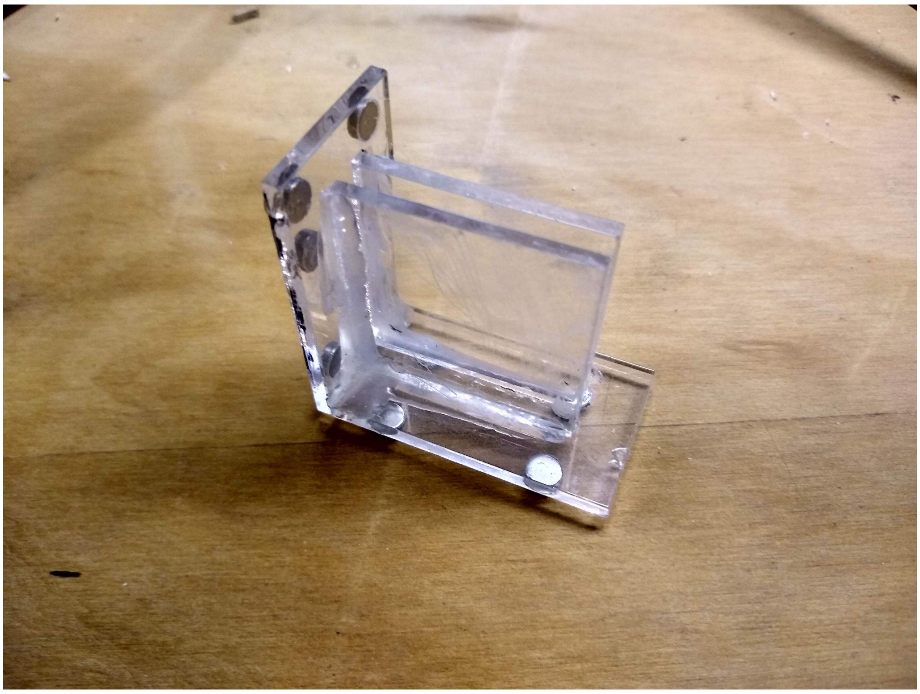

Figure 2.5: The adapter

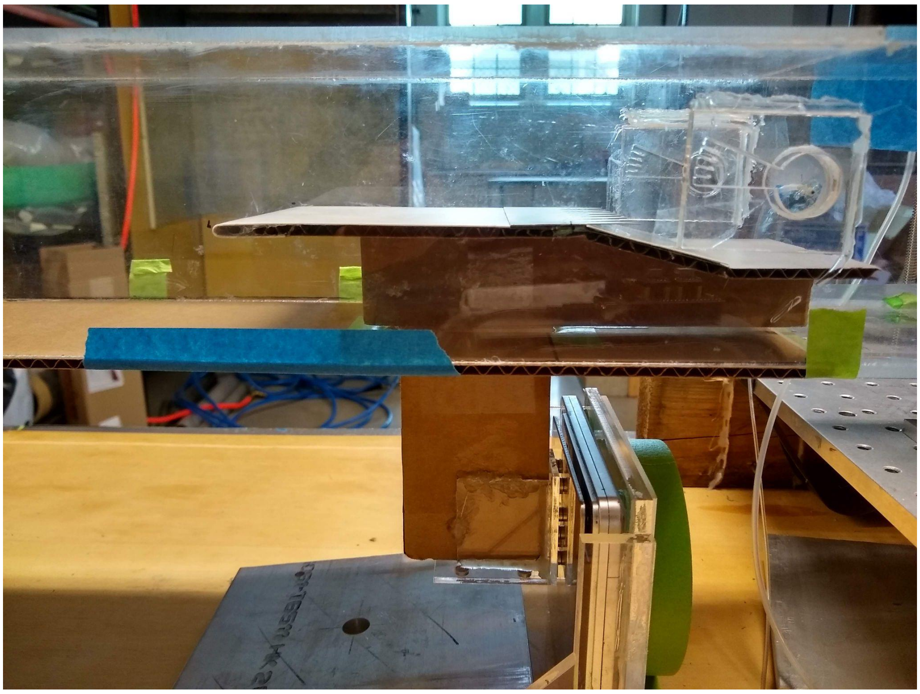

Figure 2.6: The force balance under drag-measuring configuration

Figure 2.7: The force balance under lift-measuring configuration

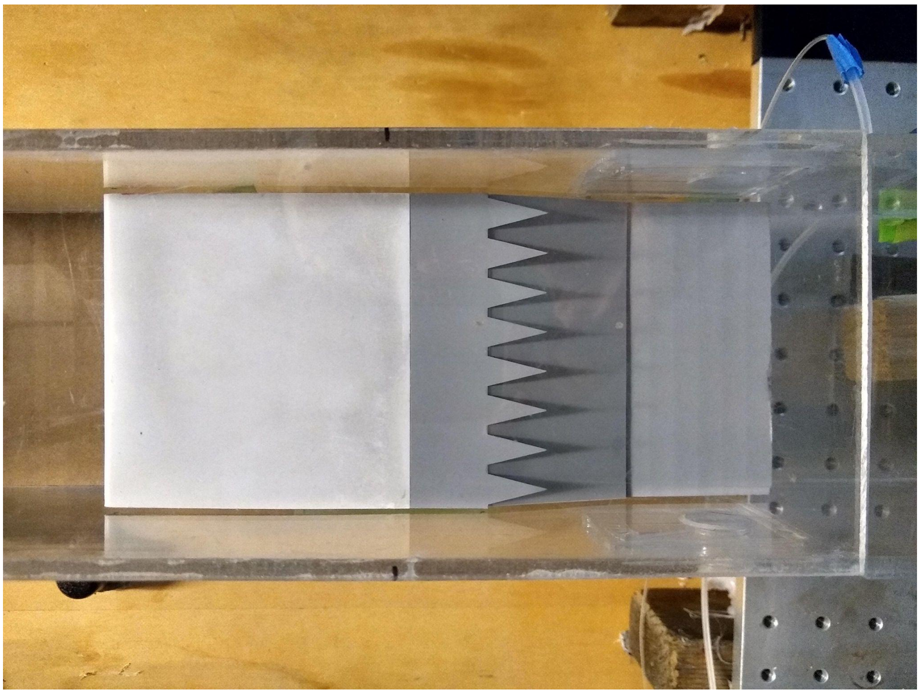

Figure 2.8: The top view of the ramp.

The gap of the ramp model to the wind tunnel wall is 1 mm.

2.2 Serration Sheet Construction

The serration is fabricated from polystyrene sheets of 0.5 mm thickness. As mentioned in section 1.3, the dimensionless parameters are ξ, η, and the device geometry. Combinations of different parameters are drawn using CATIA, and then the serrations are cut from sheets with an Epilog Fusion M2 laser cutter. The serrated sheets on the ramp models were attached using blue clay or double-sided adhesive tape. For consistency, all serrations have sharp edges with minimum rounded corners due to removing the flash.

2.3 Ramp Models Construction

Each of the ramp models consist of 1) a separation ramp, 2) a front flat plate, 3) a rear flat plate and 4) a balance linkage. The front flat plate is in front of the salient ramp edge. This flat plate is 120 mm in chord length and 100 mm in width with a rounded leading edge of 2.5mm radius. The rear flat plate is right after the trailing edge of the separation ramp to prevent undesirable flow interaction in the wind tunnel. The dimensions are shown in Figure 2.9 and Figure 2.10. The body of the ramp model is made of high quality B flute cardboard with sufficiently high structural rigidity. The front flat plate is wrapped with an additional 0.5 mm Polystyrene sheet to form the rounded leading edge and to provide a smoothly flat surface (Figure 2.11). Since the boundary layer separation is by nature an unstable phenomenon, it is sensitive to the boundary condition [35][36]. The front flat plate surface is sanded with 1000# sandpaper to maintain the surface quality being consistent to the serration sheets and the ramp surface. The 0.5 mm Polystyrene sheet only extends 95mm from the leading edge and forms a step between the sheet and the cardboard surface. The serration sheets sit behind this step maintaining a smooth surface. More examples of the serration sheets installed on the ramp model are shown in Figure 1.17 and Figure 2.12.

2.4 Fluorescent Oil Flow Visualization

The 5W engine oil mixed with UV dye will be used for indicating the momentum transport on the ramp surface to evaluate the flow attached distance and observing vortex interactions. Due to limitation of the facility size, the oil dot method would cause the surface tension force dominating the oil flow pattern. This problem results in incorrect indications or worse, altering the surface flow field (Figure 2.13). Therefore, the author evenly applied a thin film of oil on the ramp surface to reduce the domination of the surface tension to get more detailed images (Figure 2.14). Furthermore, it was found that coat the Polystyrene surface with Gunz 1000# surfacer and polish it with 1000# sandpaper can reduce the oil surface tension. The surfacer would not reflect too much UV blacklight, and therefore enhance the image quality. The blacklight used in the experiment is TaoTronics TT-FL002, which is mounted as Figure 2.15 shows. All pictures are taken by a Nikon D3300 camera using the following settings: a) Time of exposure: 1/160 second, b) Aperture: F/4, and c) the ISO: 800. Some necessary adjustments have to be performed afterward to extract more surface flow details and to compensate for ambient lighting interference. The adjustment parameters are: 1) Saturation: 0.55 ~ 0.65, 2) Contrast: 0.40 ~ 0.46, and 3) Brightness: -0.60 ~ -0.55.

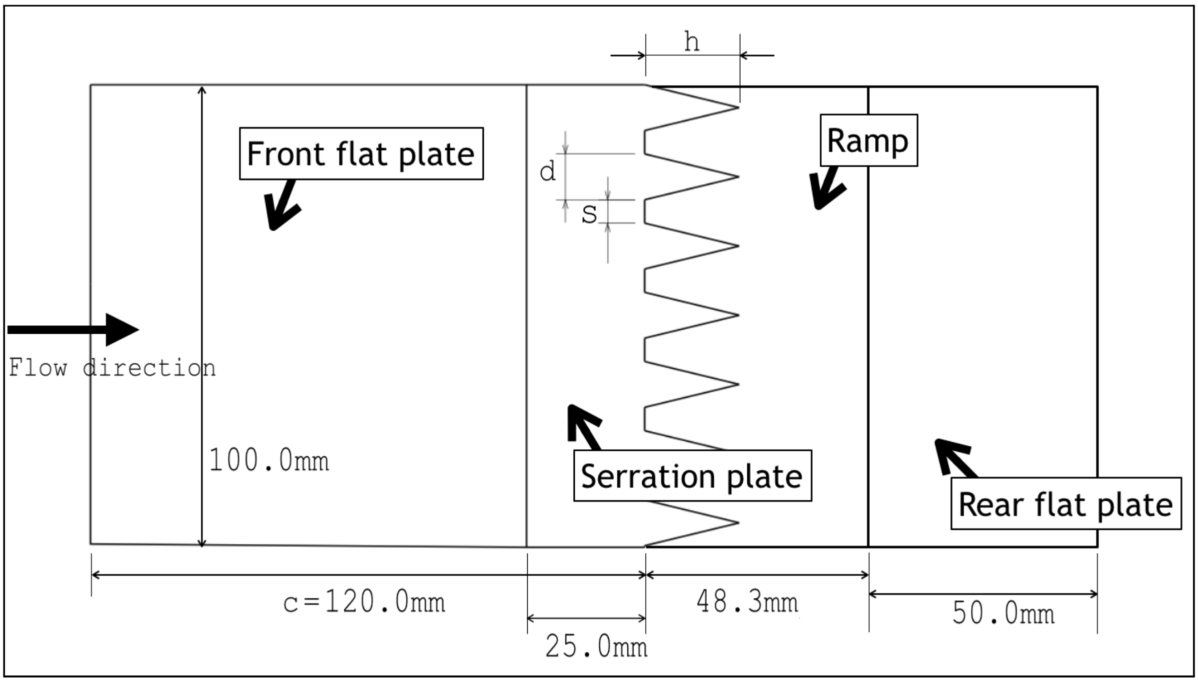

Figure 2.9: Top view of the ramp

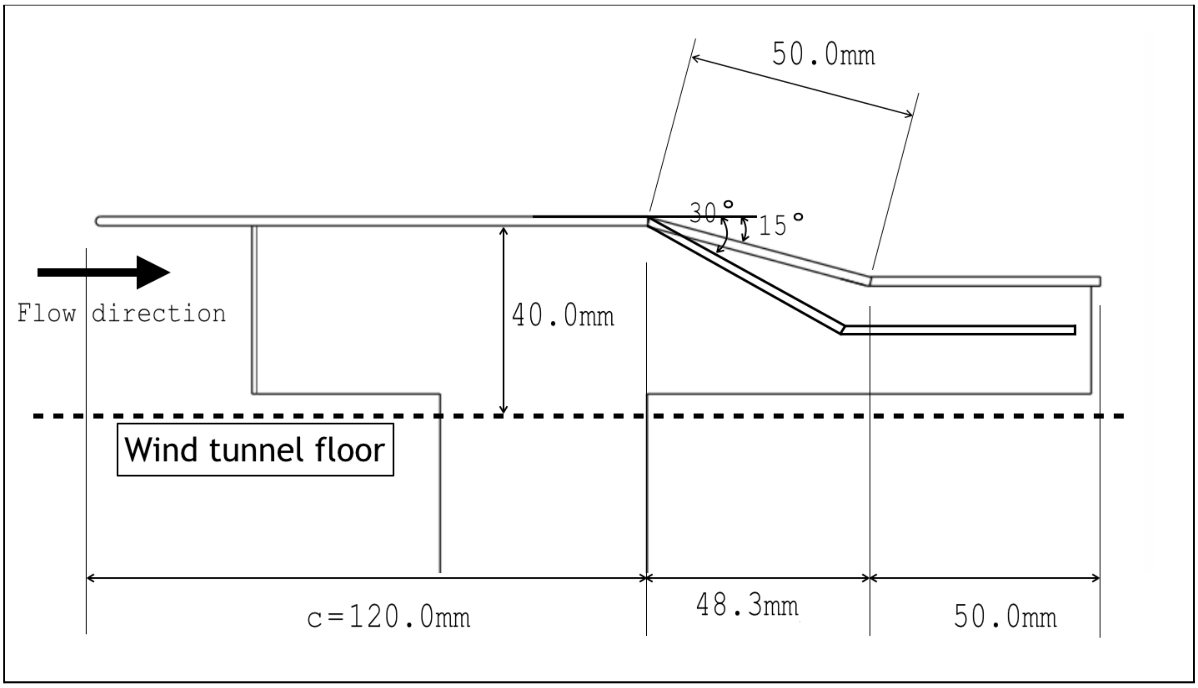

Figure 2.10: Side view of the ramp

Figure 2.11: The rounded leading edge

Figure 2.12: The invariant (no serrations) installs on the testing position

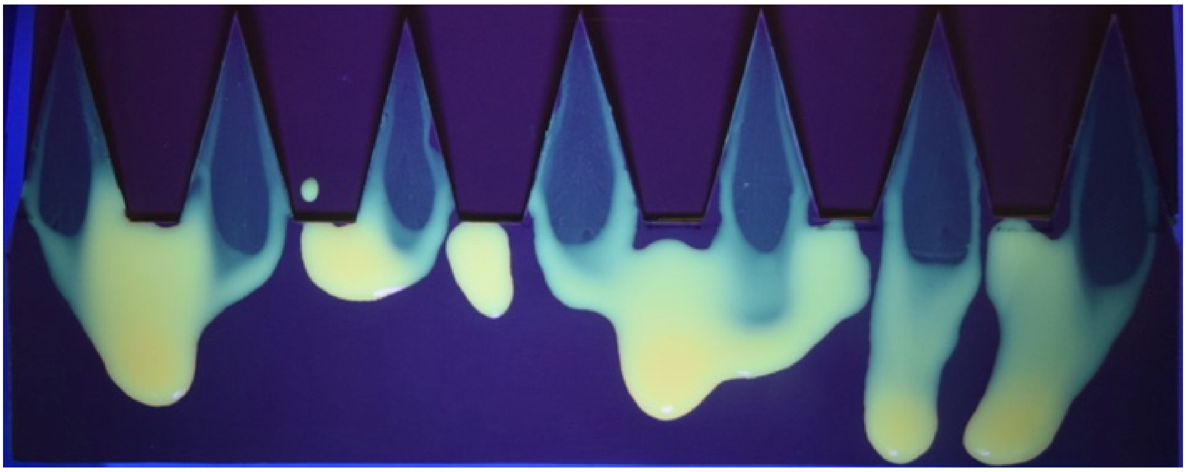

Figure 2.13: Flow visualization of using the oil dot method. The oil surface tension interferes with the observation. (Note: it is a demo figure that is not related to the research topic. The top is the upstream direction)

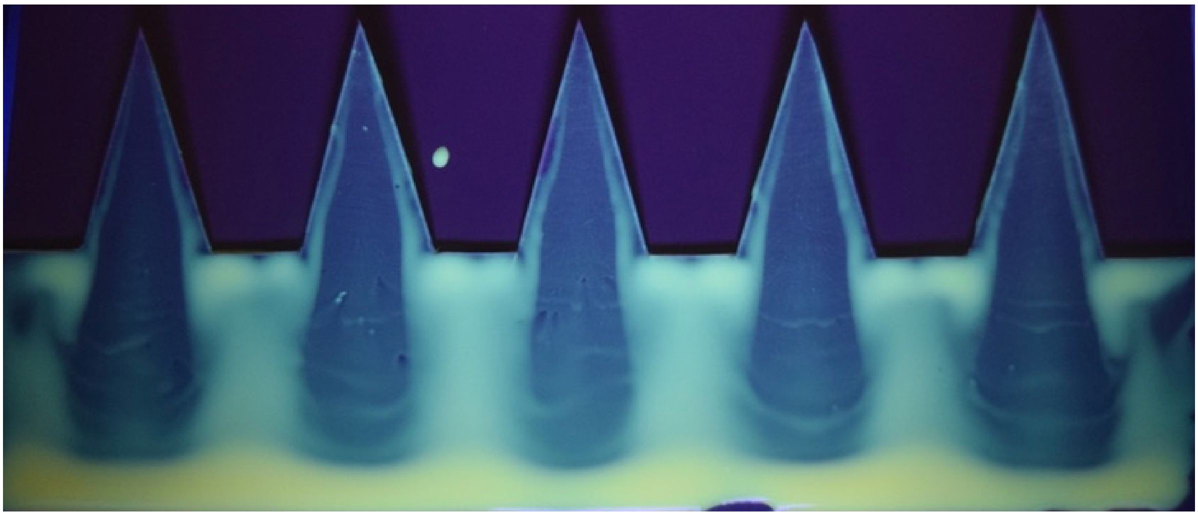

Figure 2.14: Flow visualization of using the thin oil film method. More details of the surface flow pattern can be observed. (Note: it is a demo figure that is not related to the research topic. The top is the upstream direction)

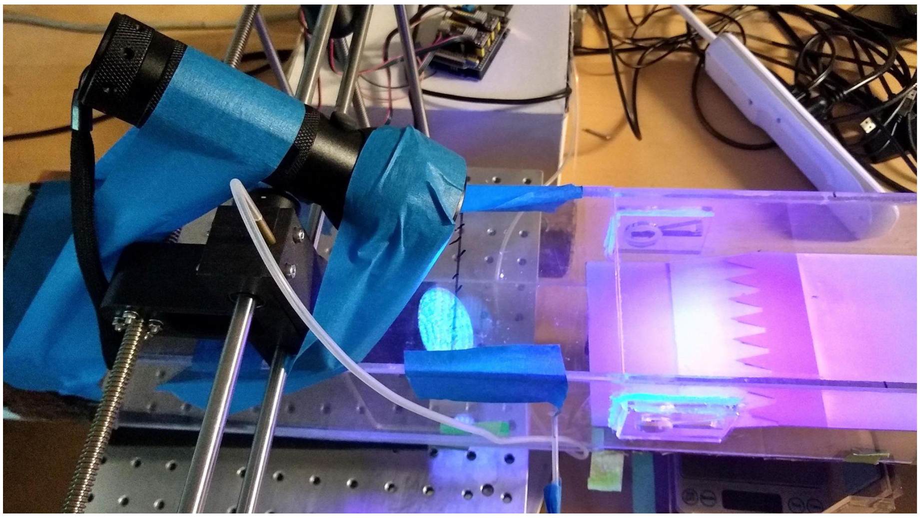

Figure 2.15: The black light setup

Chapter 3

EXPERIMENTS AND RESULTS

3.1 Test Procedures and The Road Map of Testing

Before starting the measurements, the electronic scale was calibrated using calibration weights. To reduce measurement errors, the adapter sits at the same location on the scale platform throughout the experiments. The gap between the balance linkage and the wind tunnel floor opening is maintained 2 mm in all directions. The ramp models have to ensure 1 mm intervals to both sides of the wall, as well as the balance linkage gap to the floor that we have mentioned previously. This precaution ensures the leading edge of the ramp model is perpendicular to the flow path. Ensuring four corners of the adapter is fully contacting the scale platform to maintain the ramp front plate parallel to the flow path. The ambient temperature variation is also recorded to calibrate the lift and drag coefficients. The tests are done by variant - invariant pair method for measuring the lift and drag. For every combination of parameters, an invariant of the Polystyrene sheet with a straight trailing edge will be tested first to establish a baseline, and then it is quickly replaced by a serration sheet to obtain the data variation. The time interval of the lift and drag measuring was controlled in a short period no more than 7 minutes to prevent the lift-to-drag ratio data to be affected by the ambient temperature change. Since the wind tunnel is small and it takes only 10 ~ 12 seconds to fully accelerate the tunnel flow, we limit every test running no more than 45 seconds to reduce the influence of the ambient temperature variation during the test.

The flow visualization uses the thin oil-film method to overcome the surface tension force issue. The oil film is applied on the ramp and quickly installed in the wind tunnel to prevent the gravity pulling it down. The run time for the flow visualization is much longer, 2 minutes, to ensure a fully developed flow pattern. This difference does not conflict with the previous 45 seconds limitation, since the force measuring is not taking place during the flow visualization tests. After taking the picture, the oil film has to be evenly reapplied for the next test.

The road map of the experiments is illustrated in Figure 3.1. Three types of devices, a) sharp delta, b) double delta and c) divergent delta, are tested on two ramp models with 15° and 30° ramp deflection, respectively. For each type of devices, we plot ξ on the horizontal axis and the lift variation, the drag variation, and the lift-to -drag ratio variation on the vertical axis. Repeat the plots for all of the three η values. Since the $\eta = 0.04$ for the divergent delta serration is too small to be accurately manufactured by the laser cutter, this parameter was not tested for the divergent delta geometry. After finishing the above basic data sets, two modifications of the serrations, 1) adding the partitioning plates and 2) performing tip treatments, are tested on the 15° ramp using divergent delta serrations and sharp delta serrations, respectively.

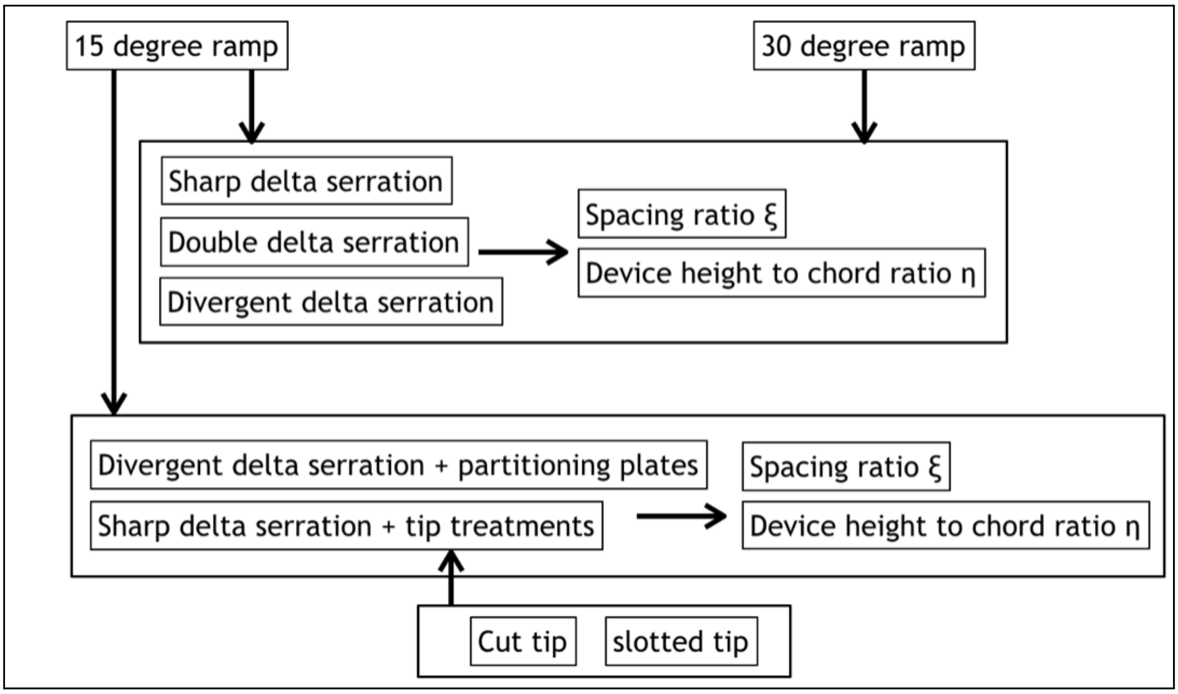

Figure 3.1: The testing road map of the research

3.2 Experimental Results on 15° Ramp

From section 3.2.1 to section 3.2.3, we discuss the results measured by the force balance and the flow visualization images on the 15° ramp.

3.2.1 Sharp Delta Serrations on 15° Ramp

The devices are distributed over the full span of 100 mm. We want to know how the device spacing influences the lift and drag, but the span is not big enough to swallow the possible data deviation caused by the difference of the device amount. In this sharp delta serration tests, there are 10 devices over the span when $\xi = 0.00$, but there are only 3 devices over the span when $\xi = 1.00$. It is over three times the difference. To accurately reflect the influence of the spacing, the C_l and C_d variation over the ramp span will be divided by the amount of the serration gaps (Noted not the amount of the serrations, but the gaps between a pair of serrations. The gap between a serration to the wall is not included), and present as normalized C_l and C_d variation, denoted as $C_{l,n}$ and $C_{d,n}$, respectively. The baseline error also shrinks down from ±1% about the zero C_l and C_d variation over the span by the denominator of the gaps amount. A table of normalized baseline errors is provided in the Appendix A for reference. For the convenience of the discussion, we call the device at $\eta = 0.16$ the large device, $\eta = 0.08$ the medium device, and $\eta = 0.04$ the small device in the following discussion.

In Figure 3.2(A), the large sharp delta device shows $C_{l,n}$ reduction throughout the entire ξ range. As the ξ increases, the $C_{l,n}$ reduction grows from -0.16% at ξ = 0.00 to -0.43% at ξ = 0.75, and the slightly increase to -0.37% at ξ = 1.00. The medium device has a $C_{l,n}$ rise of +0.14% at ξ = 0.50 and the small device has a $C_{l,n}$ rise of +0.10% at ξ = 0.25. The medium device at ξ = 1.00 seems having a $C_{l,n}$ gaining of +0.17%, but it is also considered not too far from the normalized baseline error. The small device shows a constant invariant $C_{l,n}$ from ξ = 0.50 ~ 0.75. The lift barely increases due to the presence of the device, which means the spacing has little influence on the device $C_{l,n}$ changing at this range. However, it has an impressive $C_{l,n}$ gain of +0.1% at ξ = 0.25, which is about three times more than the baseline uncertainty.

Figure 3.2(B), the large sharp delta device shows great $C_{d,n}$ increment throughout the entire ξ range. It has a minimum $C_{d,n}$ increment of +0.26% at ξ = 0.25 of all ξ. The largest $C_{d,n}$ increment appears at ξ = 1.00, which is +1.29%. The medium sharp delta device, similarly to the large device, shows $C_{d,n}$ increment throughout the entire ξ range, but the magnitude is much less than the large device. The minimum $C_{d,n}$ increment of +0.13% appears at ξ = 0.25 and the largest $C_{d,n}$ increment of +0.31% appears at ξ = 0.50. The small device shows a constant invariant Cdn from ξ = 0.00 ~ 0.50, and is followed by about +0.08% $C_{d,n}$ increment at ξ = 0.75 & ξ = 1.00.

Combining the above results, only the small device at ξ = 0.25 gains some lift increment, but in general the existence of the sharp delta device does not gain much increase in the maximum C_l. However, as we can find in the Figure 3.2(C), the small device can increase the lift-to-drag ratio up to 3% at ξ = 0.00 & ξ = 0.25. It is interesting why the serration does not perform well to enhance the performance. In the preliminary research, the mini tufts indicated attached flow over the ramp surface with the presence of the serration. The results of the oil flow visualization might be able to answer this baffling question.

The Figure 3.3 (A) shows the oil flow visualization of the salient ramp without any serration device. We found a stripe of the separation bubble downstream of the salient edge, but there is an attached region followed by the stripe covering about 0.43r of the ramp length. This attached distance is relatively long compared to other cases with serrations. This reattached phenomenon is caused by the character of low-Reynolds-number laminar flow. Between Reynolds numbers of 10^4 to 10^6 , the laminar boundary layer has a lower momentum, the transition to turbulent flow occurs in a free shear layer, which entrains higher momentum fluid from the outside of the laminar separation bubble and reattaches the flow to the surface [37][38][39]. With the baseline setting such a high standard, it is not surprising that lift and drag improvement of the serration devices are not so obvious. In fact, as shown in Figure 3.3 (B), (C), (D), the darker regions are extending polystyrene sheets without serrations, each of the sub-figures representing different values of η. Only when $\eta = 0.04$ is the attached distance short. In the cases of $\eta = 0.16$ and $\eta = 0.08$ do not have any attached flow over the ramp. It has been preliminarily measured that all combinations of serrations have much more performance improvement if we compare the results with these non-attached-flow baselines. It is possible the serration could gain more benefits if working at a higher Reynolds number. With that being said, Liu et al. [25] found lift coefficient reduction using the wing trailing edge serration. The sawtooth serration in the paper is very similar to the sharp delta geometry in our research. Perhaps there are some similarities in the flow physics causing this phenomenon as well. By examining the flow visualization images, we found obvious stagnation regions near the serration tips throughout all cases. This phenomenon might be caused by a pair of vortices forming on each side of the serration colliding with each other as they develop toward the tip. Since the vortex pair is counter-rotating, the collision may neutralize each other's energy and form a stagnating region. Recall the vortex structure mentioned in the beginning of section 1.2. The doublet and the wishbone VGs produce a pair of counter-rotating vortices, leaving a low energy realm in between. We can observe this low energy "walkway" right after the tip stagnating spot between two serration gaps. (Figure 3.4). In the large devices, as the spacing of each device increases, we can find another walkway forming along the centerline of the gap, causing even more complex downstream flow fields (Figure 3.5, Figure 3.6). It is also found that as the size of the devices gets smaller and closer to each other, the stagnation points merge to each other forming a stripe much like the Figure 3.3 (A), and the flow field over the ramp is closer to two dimensional structure. For the small devices, the stripe is downstream further away from the tips (Figure 3.7). The flow visualization images of all parameters are in Appendix B-1.

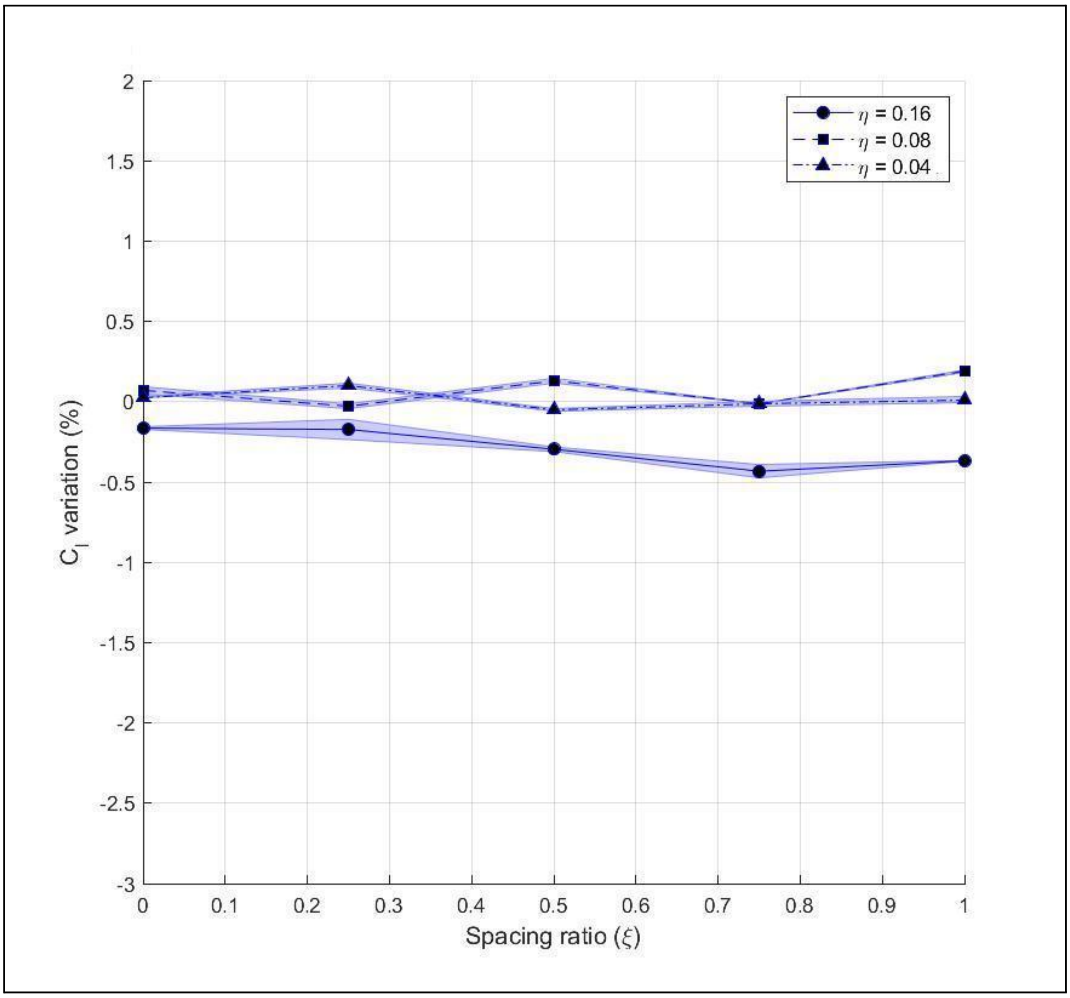

Figure 3.2(A): Normalized C_l variation of sharp delta serrations on 15° ramp

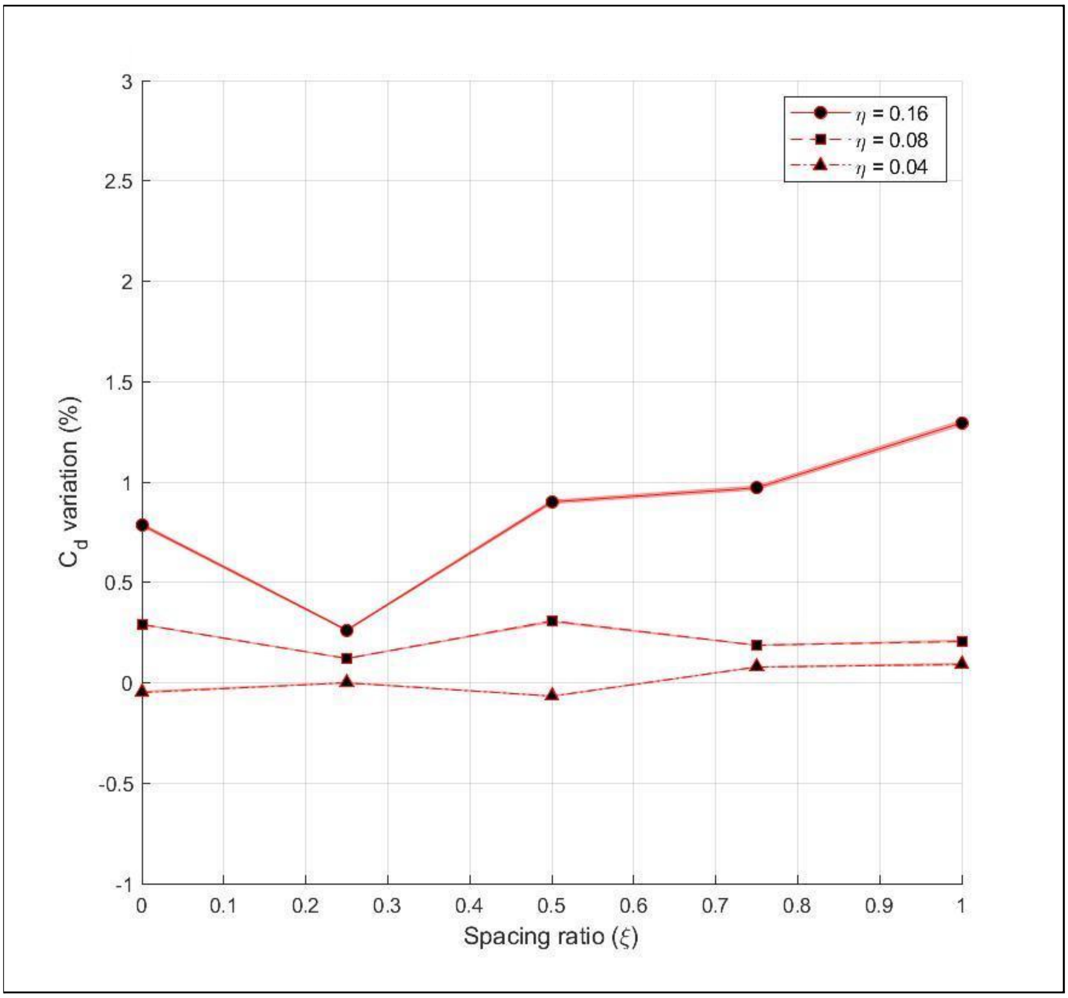

Figure 3.2(B): Normalized C_d variation of sharp delta serrations on 15° ramp

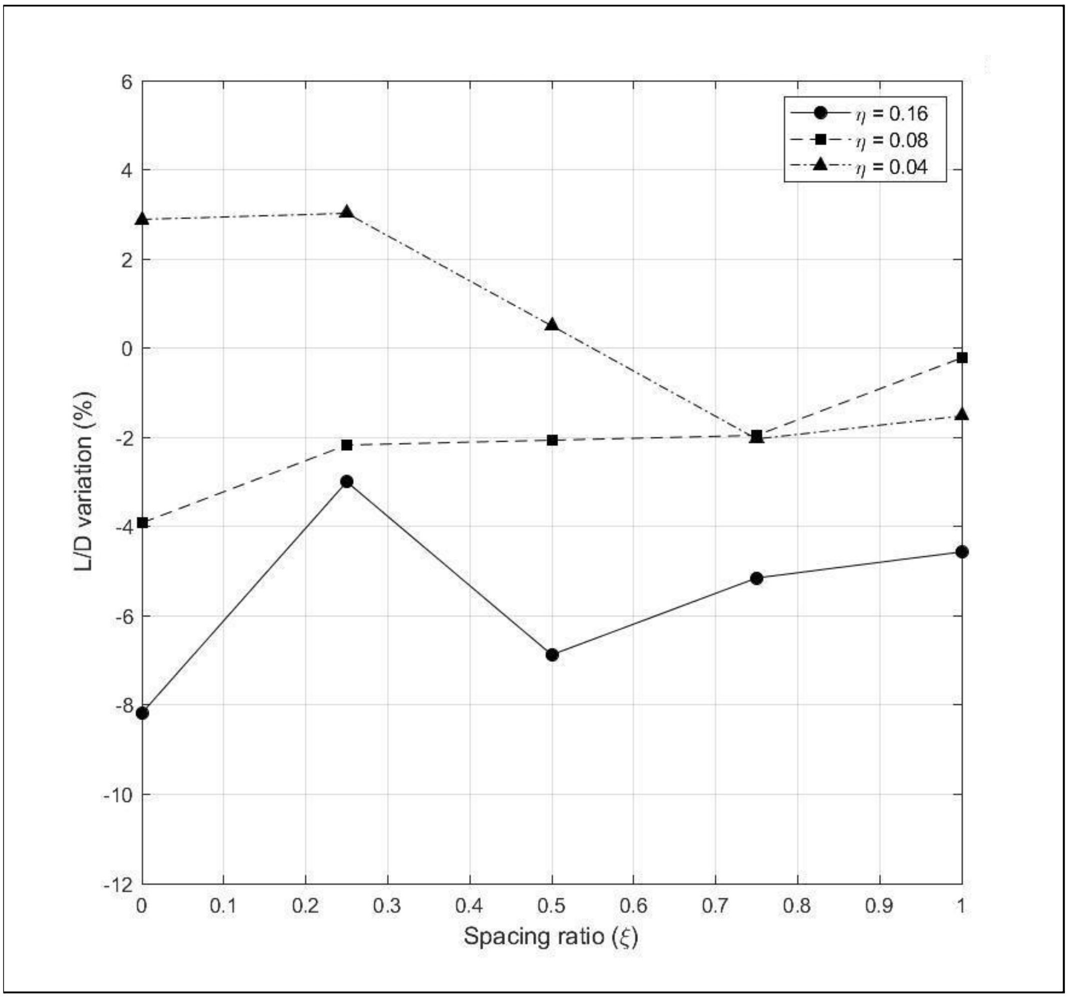

Figure 3.2(C): Lift-to-drag ratio variation of sharp delta serrations on 15° ramp

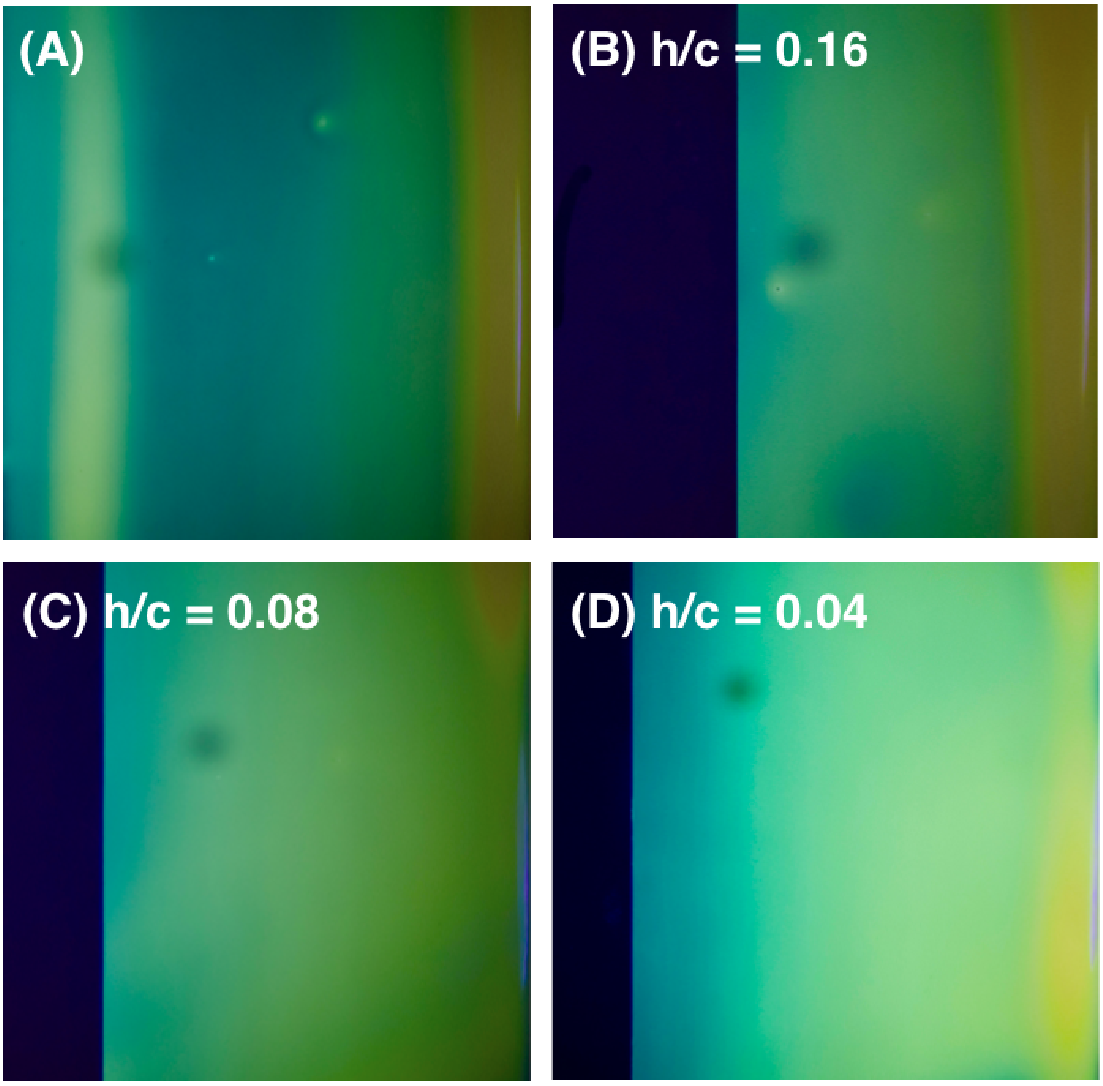

Figure 3.3: The flow visualization of the baseline (A) on 15° ramp and extending polystyrene sheets without serrations (B), (C), (D)

Figure 3.4: The tip stagnation spot and the low-energy walkway

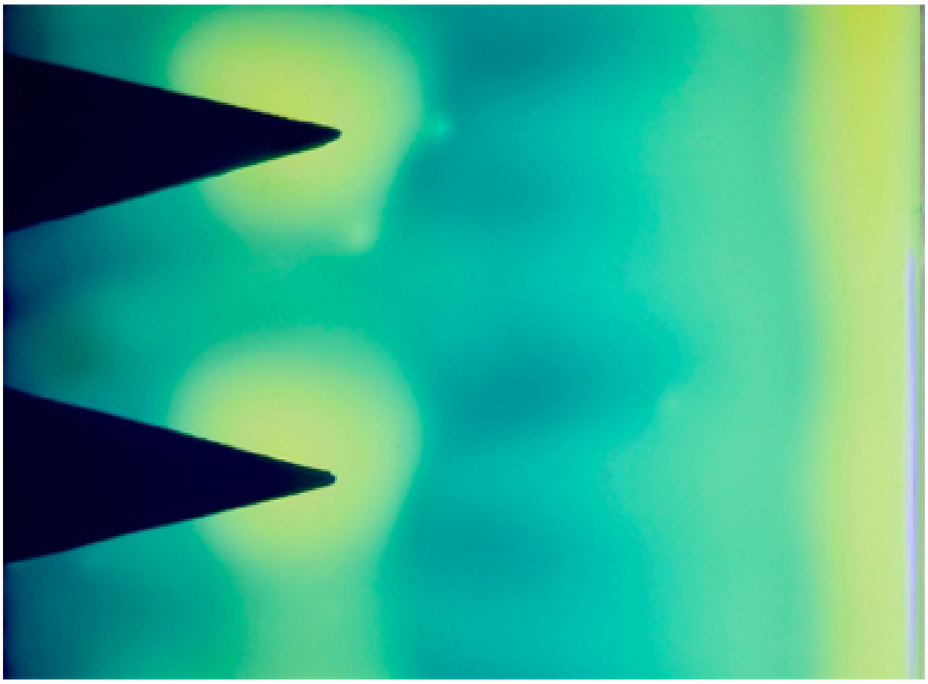

Figure 3.5: Flow visualization of the sharp delta devices at $\xi = 0.75$, $\eta = 0.16$

Figure 3.6: Flow visualization of the sharp delta devices at ξ = 1.00, η = 0.16

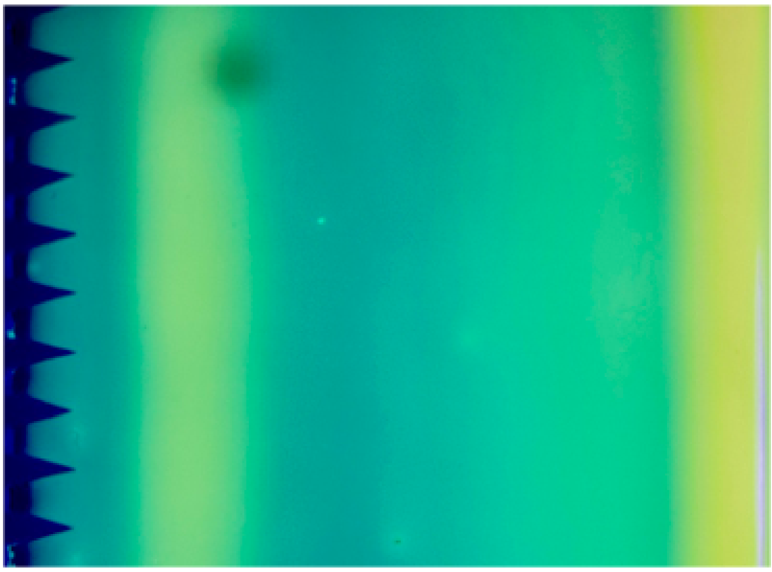

Figure 3.7: The stripe is further away from the tips as the η becomes smaller

3.2.2 Double Delta Serrations on 15° Ramp

In Figure 3.8(A), the large double delta device shows a significant reduction in $C_{l,n}$ at $\xi = 0.75$ & 1.00, whereas $C_{l,n}$ gains +1.02% at $\xi = 0.50$. Similarly, the optimum $C_{l,n}$ increment of the small device happens at $\xi = 0.50$ with $C_{l,n}$ gaining +0.23%, and then the reduction followed. Interestingly, the $C_{l,n}$ variation of the medium device increases as ξ increases. The optimum case happens at $\xi = 1.00$, with $C_{l,n}$ gaining +1.06%.

In Figure 3.8(B), the large double delta device suffers an even greater $C_{d,n}$ increment compared to the sharp delta device. The greatest $C_{d,n}$ increment is +1.80% at $\xi = 0.25$, and then it decreases. This pattern is very different from not just the medium and small double delta devices, but also the sharp delta ones.

As Figure 3.8(C) shows, the best lift-to-drag ratio increment is at $\xi = 0.50$, with the lift-to-drag ratio gaining +4.7%. Even though a reduction followed, but for the medium and small devices, the lift-to-drag ratio increment generally increasing more from $\xi = 0.50$ to $\xi = 1.00$ comparing to the small spacing ratios.

Observing the flow visualization, we can clearly see why the higher spacing ratio of the large device works better than the small spacing ratio one. From Figure 3.9(A) to Figure 3.9(C), the low-momentum flow walkway increases as the spacing increases. However, when $\xi = 0.75$ as shown in Figure 3.9(D), the walkway "breaks" in the middle, replaced by a zone of higher momentum content. We can also clearly see the sidewall effects on the outer two devices, which have longer stagnation regions near the tips. It is unclear if this phenomenon is caused by the sidewall induced vortices. In Figure 3.9(E), the sidewall effect seems much less than the previous case, but the breaking walkway can still be observed. This phenomenon gives much higher attached area over the ramp at ξ = 0.75 and 1.0 than at ξ = 0.0. The flow visualization images of all parameters are in Appendix B-2.

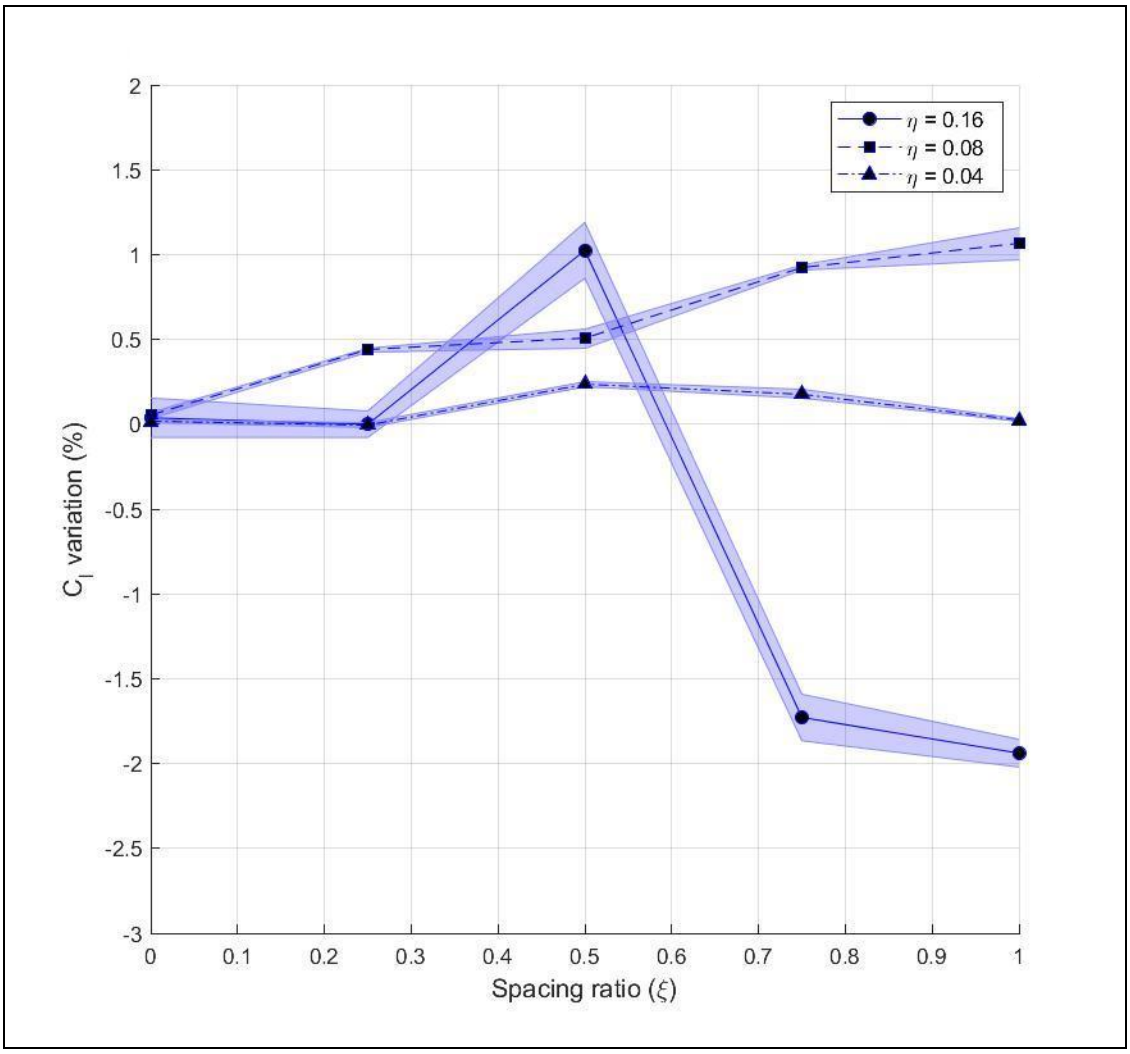

Figure 3.8(A): Normalized C_l variation of double delta serrations on 15° ramp

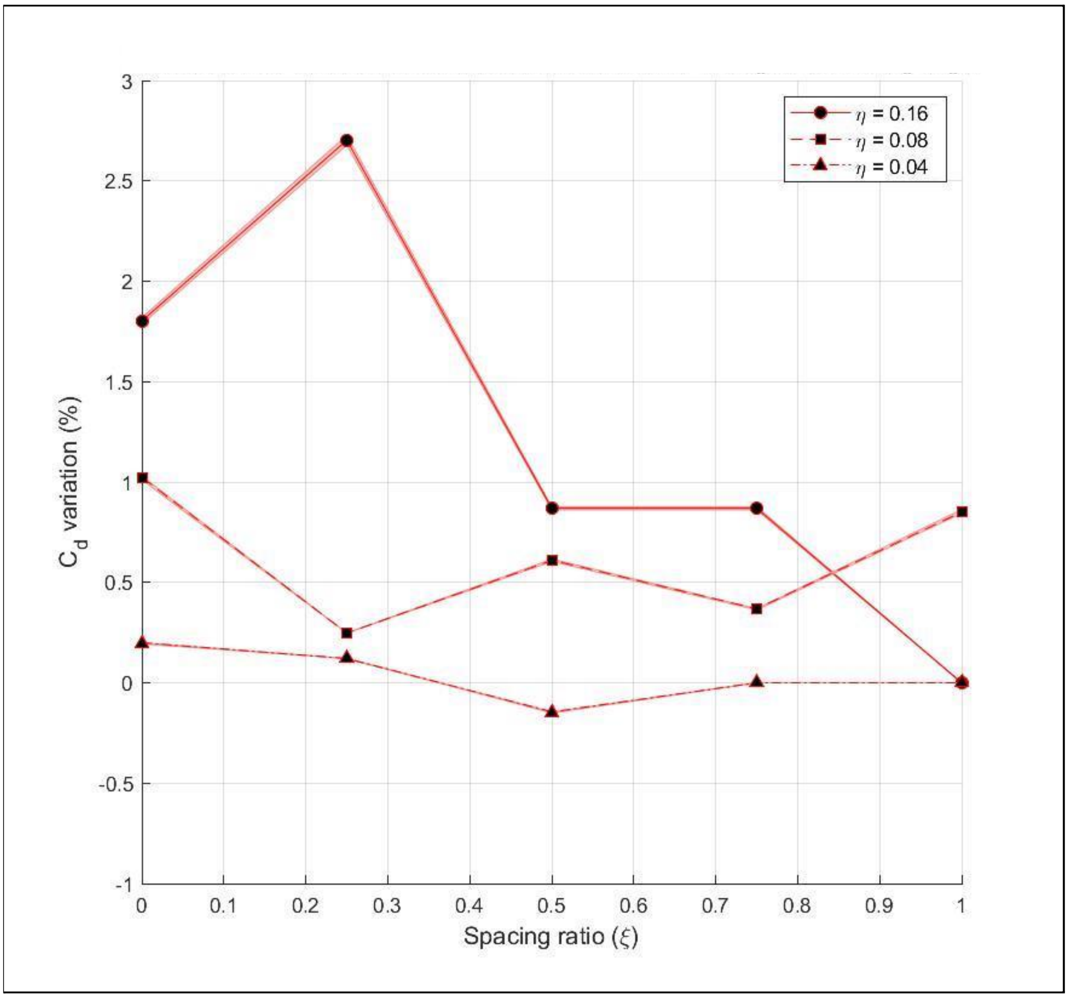

Figure 3.8(B): Normalized C_d variation of double delta serrations on 15° ramp

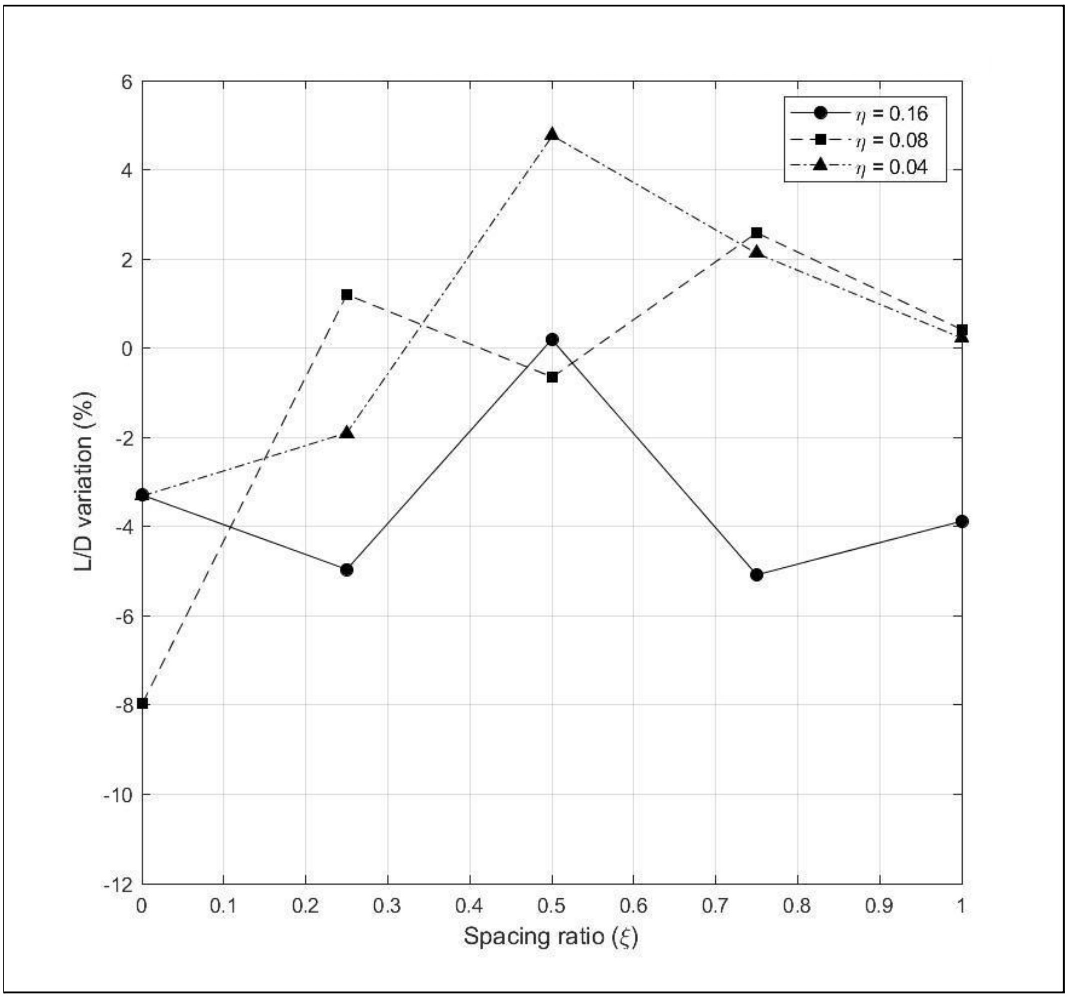

Figure 3.8(C): Lift-to-drag ratio variation of double delta serrations on 15° ramp

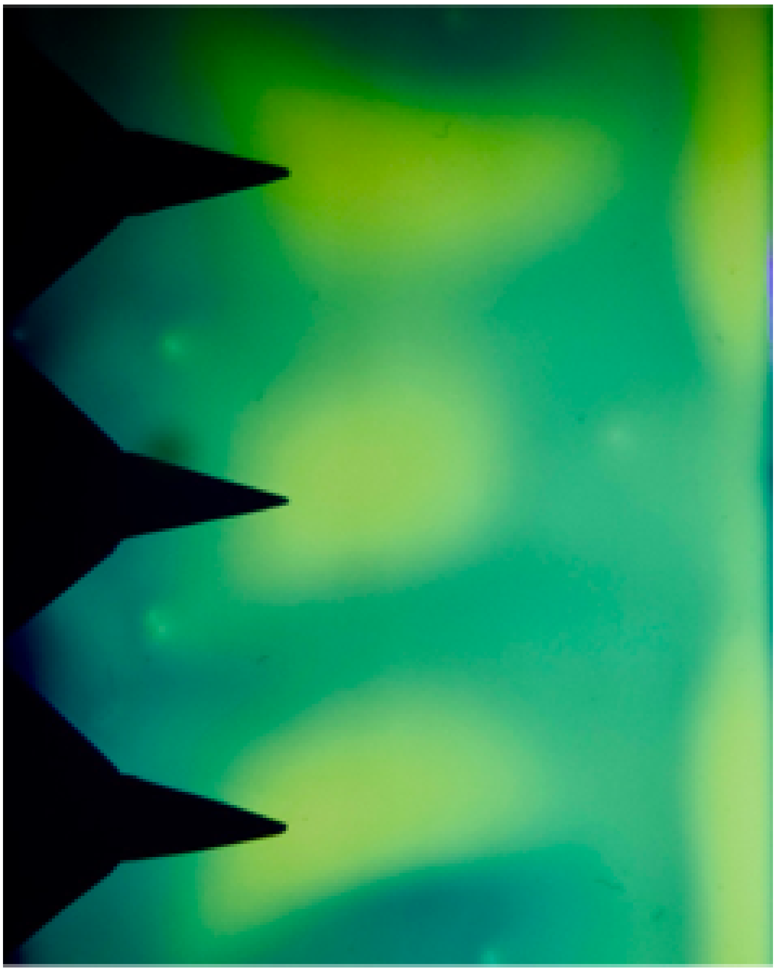

Figure 3.9(A): Flow visualization of the double delta devices at ξ = 0.00, η = 0.16

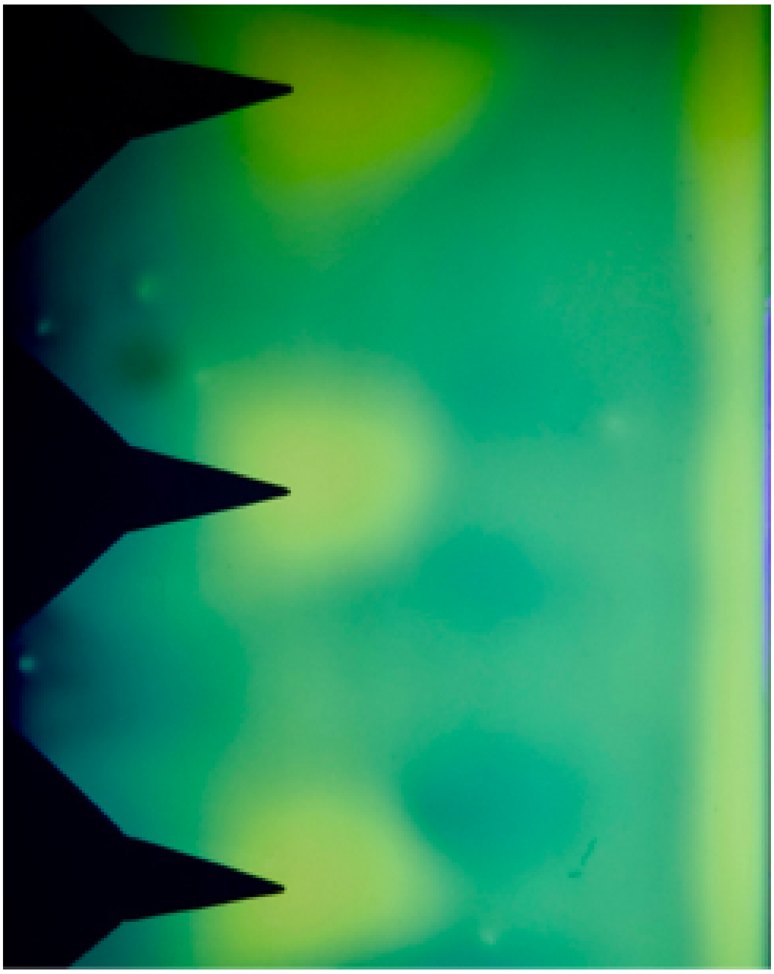

Figure 3.9(B): Flow visualization of the double delta devices at $\xi = 0.25$, $\eta = 0.16$

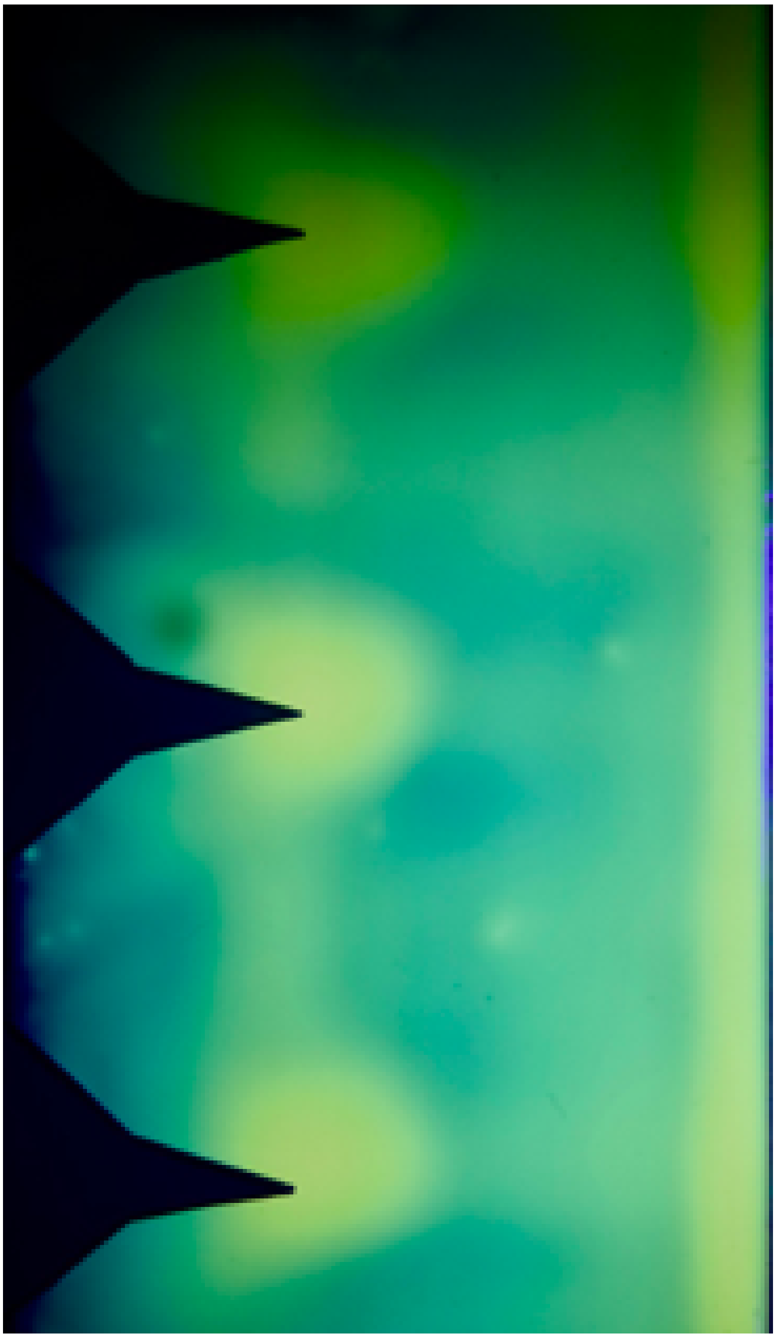

Figure 3.9(C): Flow visualization of the double delta devices at ξ = 0.50, η = 0.16

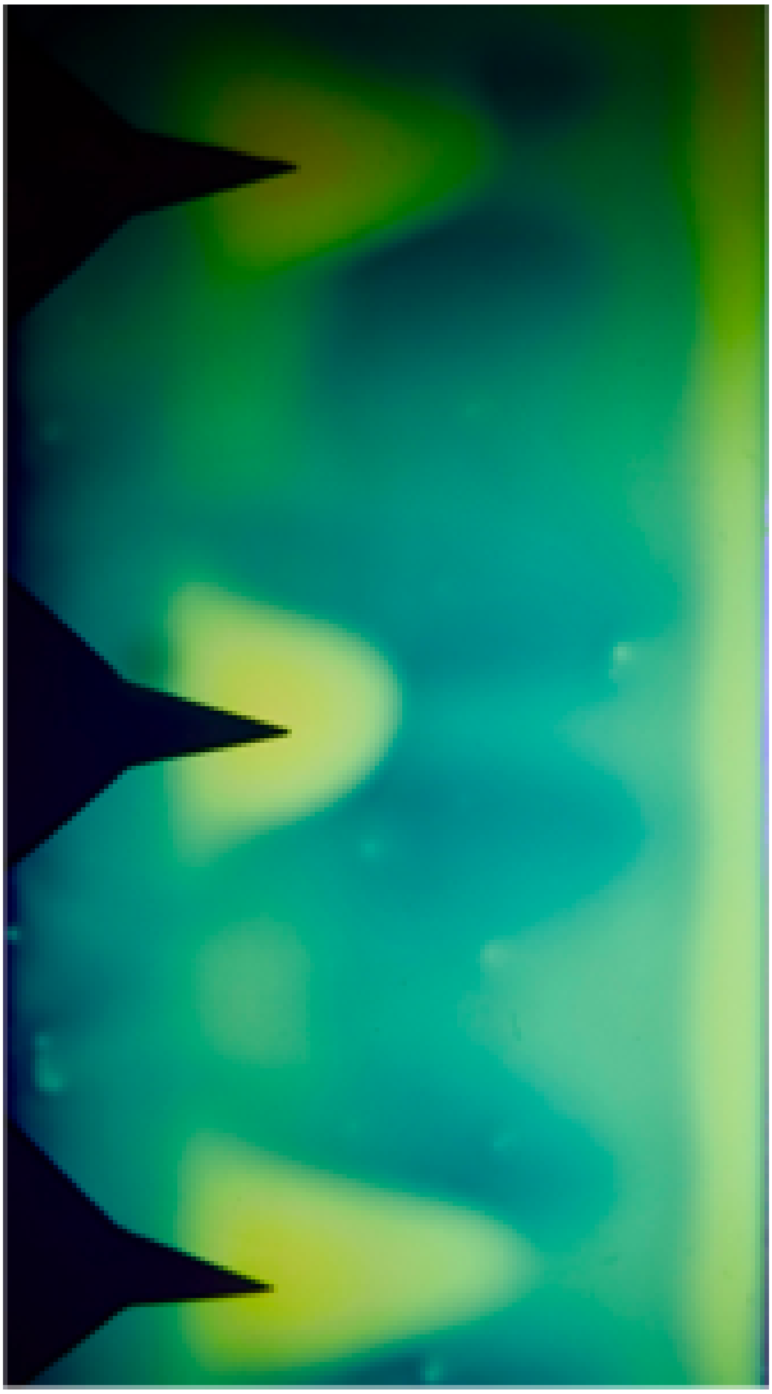

Figure 3.9(D): Flow visualization of the double delta devices at ξ = 0.75, η = 0.16

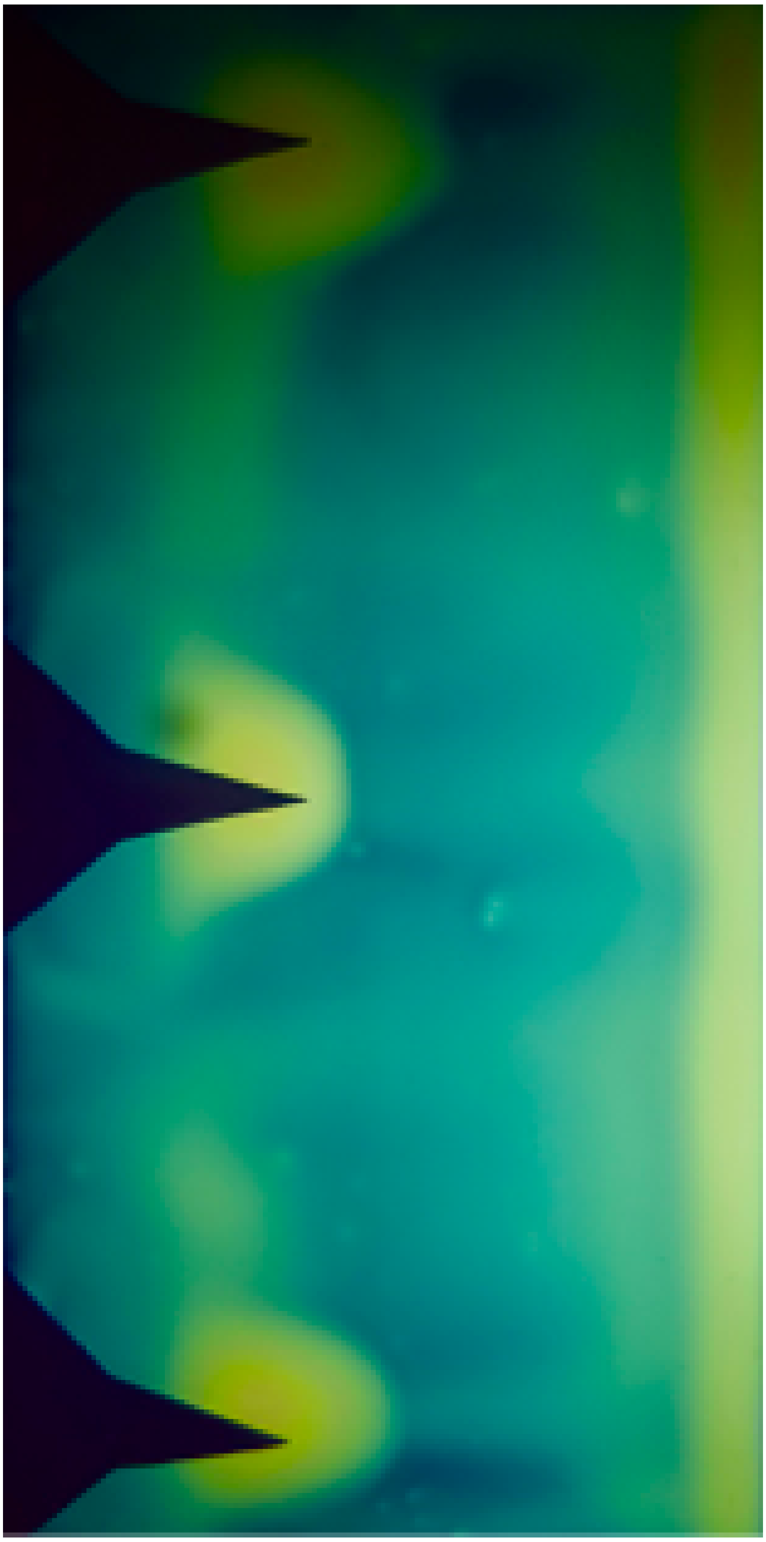

Figure 3.9(E): Flow visualization of the double delta devices at ξ = 1.00, η = 0.16

3.2.3 Divergent Delta Serrations on 15° Ramp

From Figure 3.10(A), (B), and (C), the large divergent delta device at $\xi = 0.50$ shows a $C_{l,n}$ increment of +0.57%. The best $C_{l,n}$ increment of the medium device is the same at $\xi = 0.50$ with +0.25%. The same, for the large and the medium devices, the best $C_{d,n}$ reduction appear at $\xi = 0.50$ with +0.17% and 0.00%, respectively. The median device has a better lift-to-drag ratio increment of +2.5%. At $\xi = 0.50$ for the large and the medium devices, the divergent delta device has the best lift-to-drag ratio increment than the sharp delta and the double delta geometry.

As the Appendix B-3 shows, the large device has a more organized downstream flow field over the ramp compared to the sharp delta and double delta geometry. The higher momentum flow results in higher vortex magnitude and slightly longer attached distance.

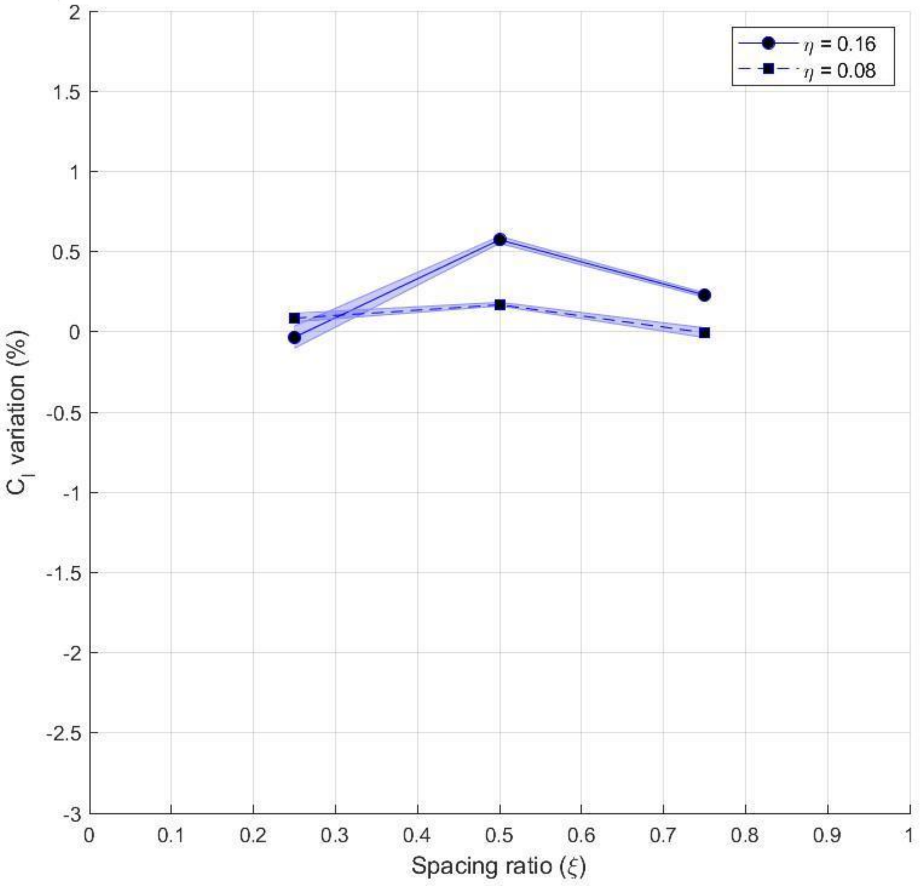

Figure 3.10(A): Normalized C_l variation of divergent delta serrations on 15° ramp

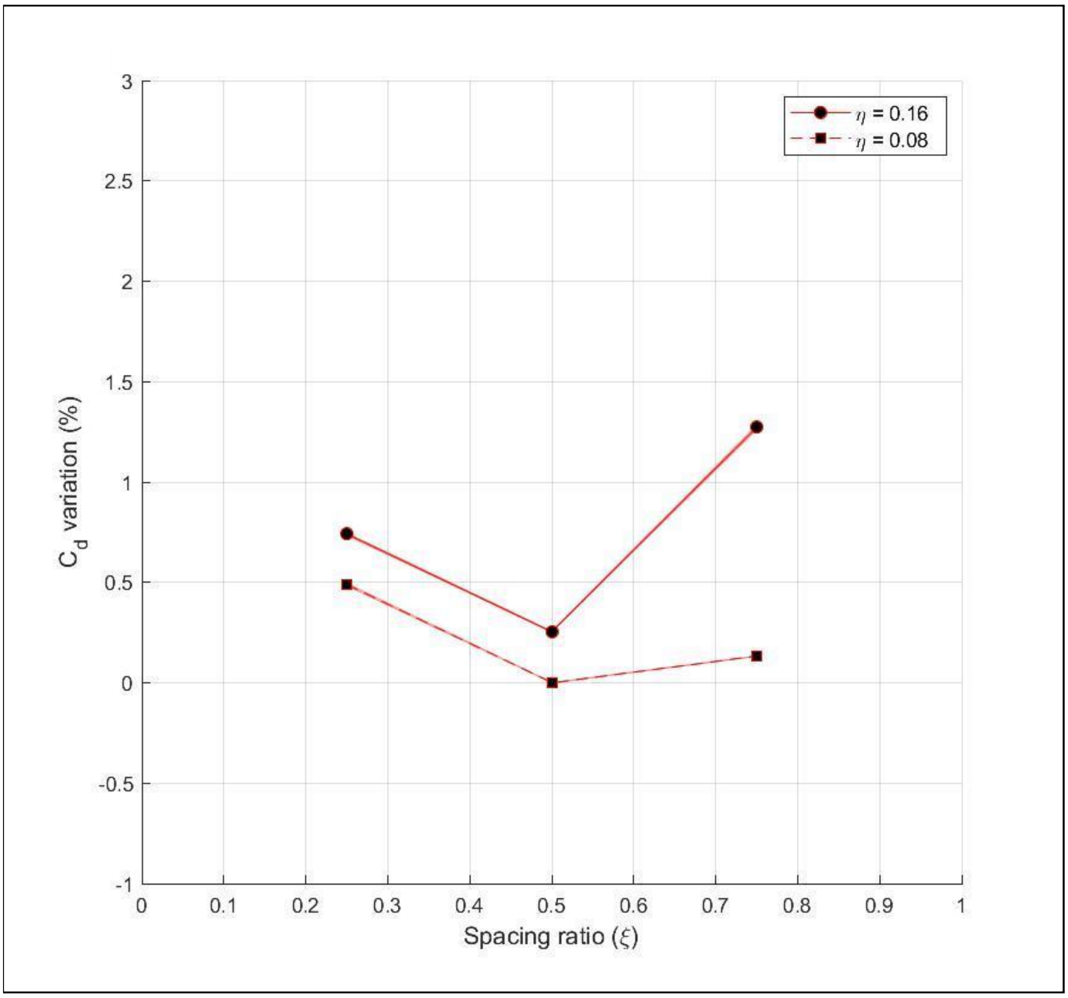

Figure 3.10(B): Normalized C_d variation of divergent delta serrations on 15° ramp

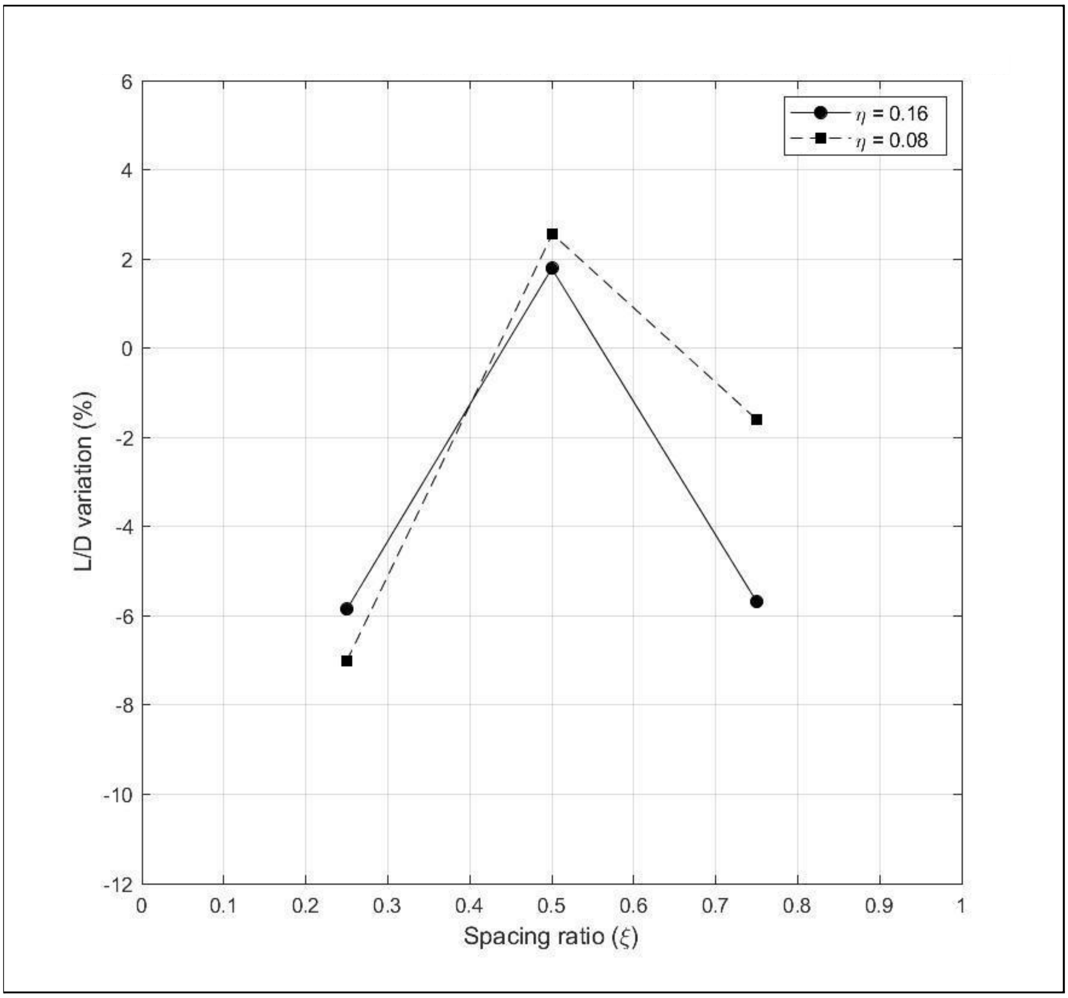

Figure 3.10(C): Lift-to-drag ratio variation of divergent delta serrations on 15° ramp

3.3 Experimental Results on 30° Ramp

From section 3.3.1 to section 3.3.3, we discuss the results measured by the force balance and the flow visualization images on the 30° ramp.

3.3.1 Sharp Delta Serrations on 30° Ramp

In Figure 3.11(A), the large device has a maximum $C_{l,n}$ reduction at $\xi = 1.00$. The trend of the $C_{l,n}$ is increasing as ξ increases. The medium device has a maximum $C_{l,n}$ reduction of -0.13% at $\xi = 0.25$, and then the reduction is constant at about -0.09% from $\xi = 0.50$ to $\xi = 1.00$. The small device does not show appreciable changes in $C_{l,n}$.

Figure 3.11(B), the minimum $C_{d,n}$ increment of the large device occurs at $\xi = 0.25$ with a change of -0.41%, and then a relatively large increase up to +0.54% followed. The minimum $C_{d,n}$ increment of the medium device appears at $\xi = 0.50$ with a change of -0.41%, and then it trends up to about 0.0%. The small device is similar to the large device and has a minimum Cdn increment of -0.06% at $\xi = 0.25$.

Figure 3.11(C), the medium device has the best lift-to-drag ratio increment of +4% at $\xi = 0.50$. The best lift-to-drag ratio increment of the large and the small device are both at $\xi = 0.25$, but the large device suffers from a reduction in the increment for all ξ. The small device at $\xi = 0.25$ increased the lift-to-drag ratio by about +1.8%.

As Figure 3.12 (A) shows, we could not observe any laminar separation bubble over the ramp surface due to the high ramp angle. From the flow visualization images presented in Appendix B-4, the magnitude of the vortices for all devices are smaller compared to the same parameters on the 15° ramp. Even though the vortices just barely reach the surface, we can still observe the attached distance. Some images show a radiating pattern near the root of the serration devices. For example, the image presented in Figure 3.13.

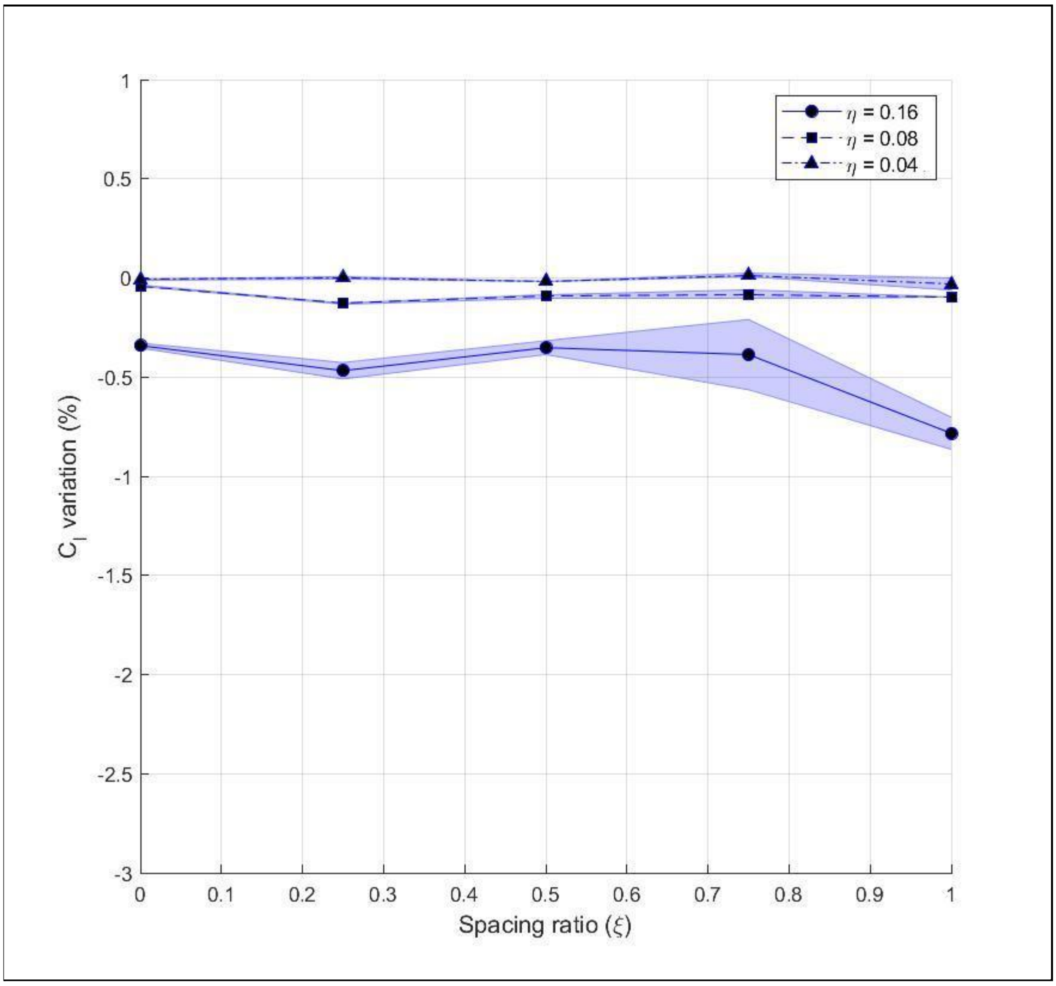

Figure 3.11(A): Normalized C_l variation of sharp delta serrations on 30° ramp

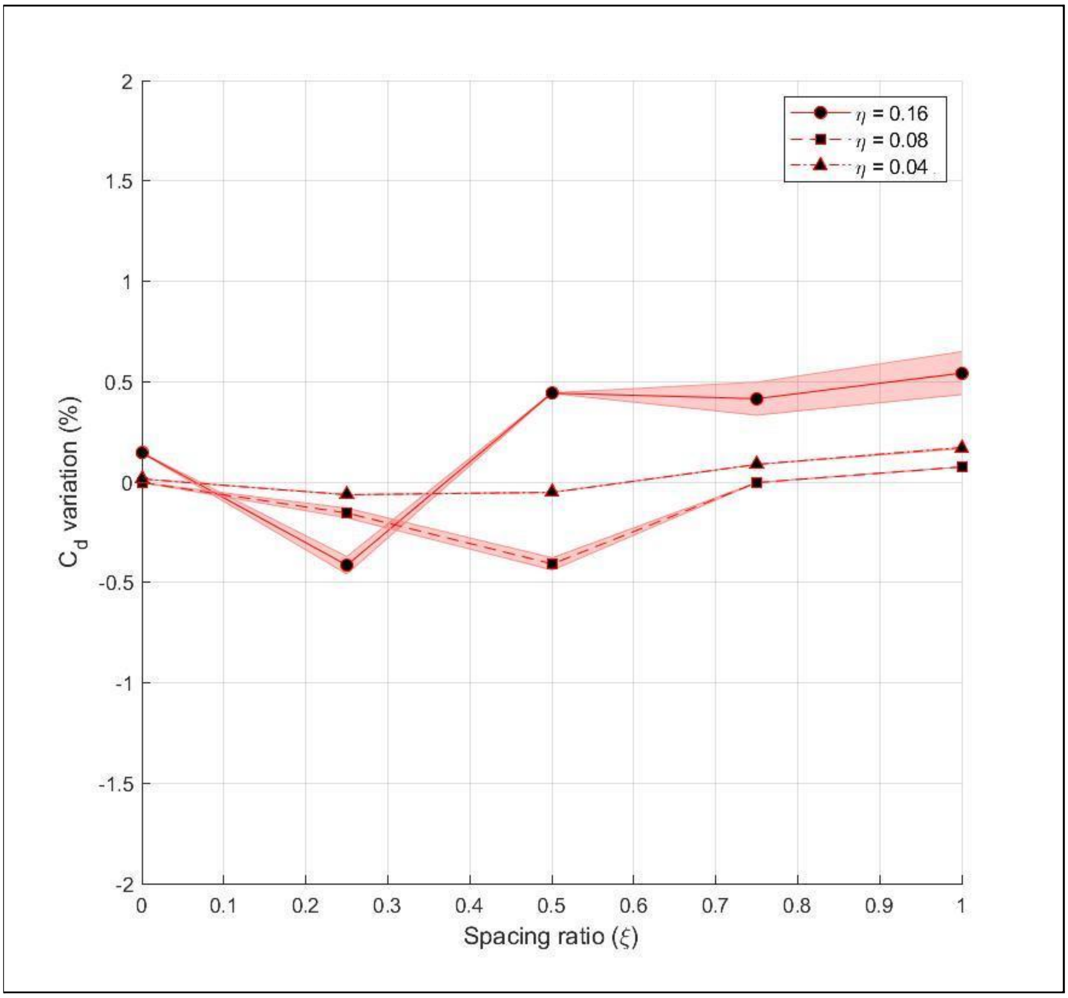

Figure 3.11(B): Normalized C_d variation of sharp delta serrations on 30° ramp

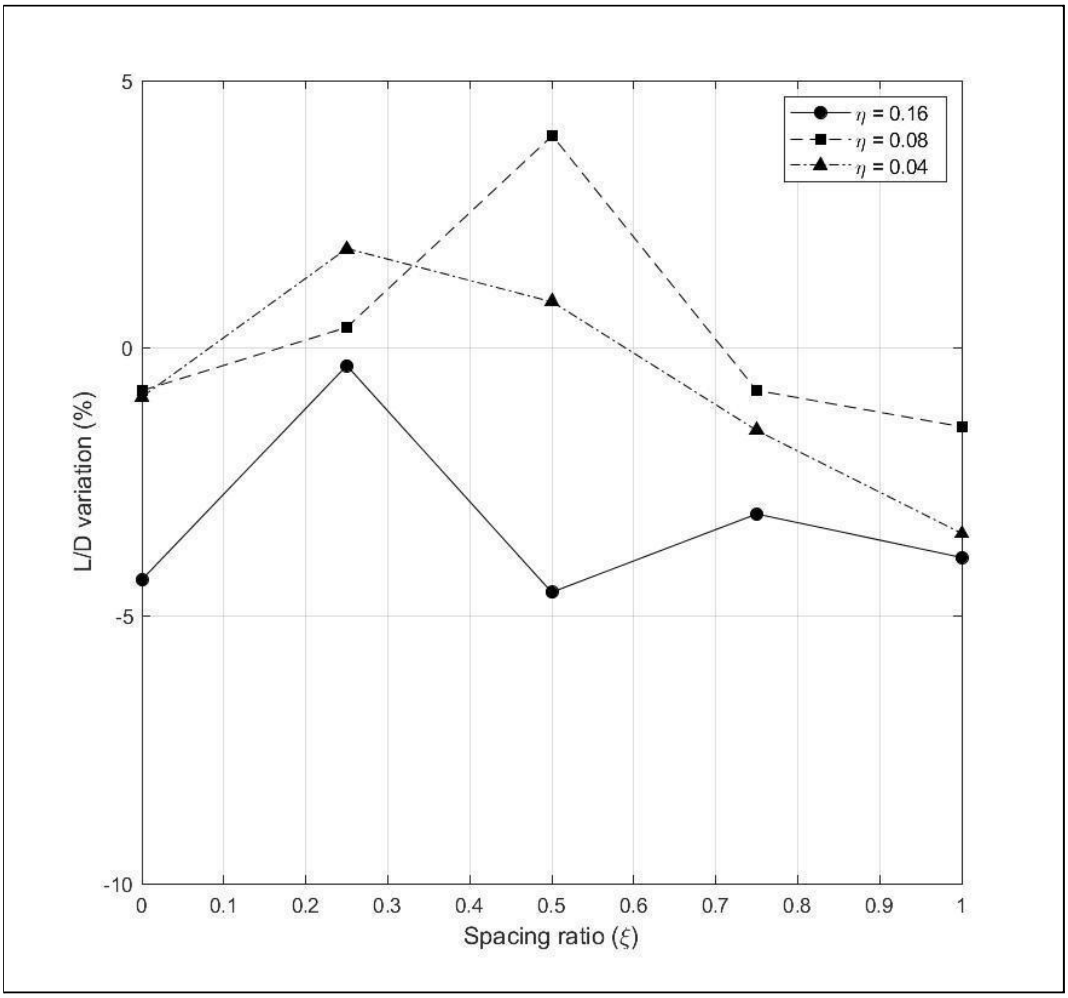

Figure 3.11(C): Lift-to-drag ratio variation of sharp delta serrations on 30° ramp

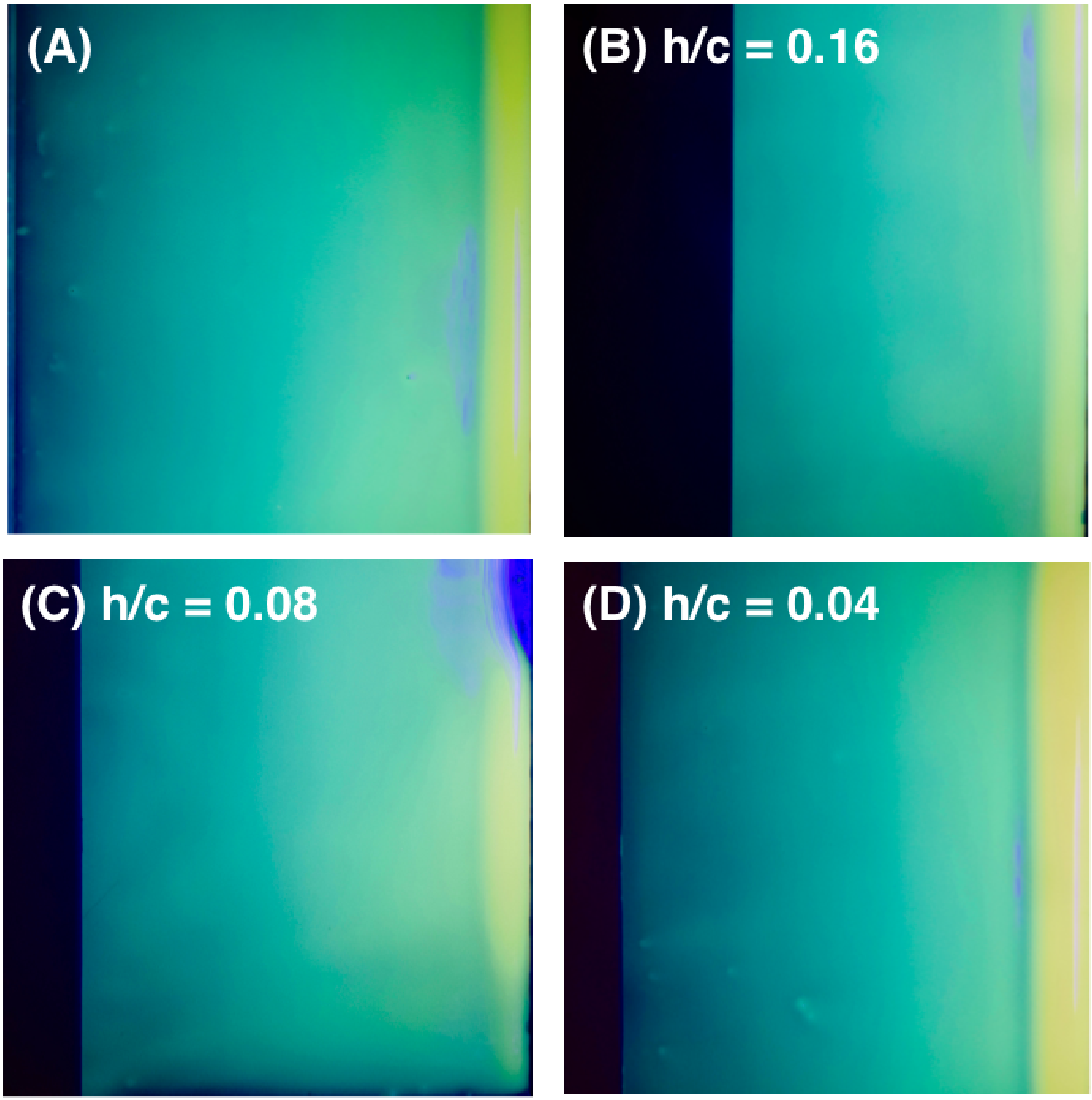

Figure 3.12: The flow visualization of the baseline (A) on 30° ramp and extending polystyrene sheets without serrations (B), (C), (D)

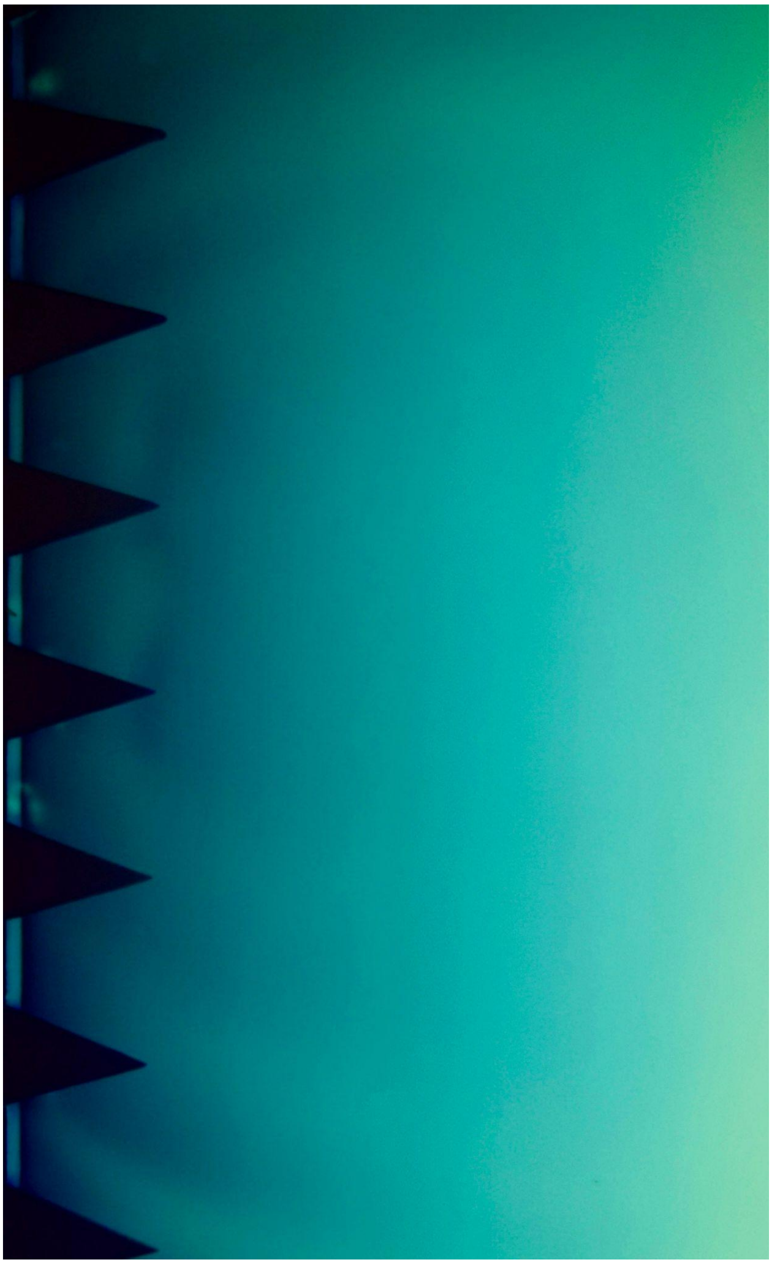

Figure 3.13: The radiating pattern near the root of the serration devices

3.3.2 Double Delta Serrations on 30° Ramp

As Figure 3.14(A) shows, the large device suffers the largest $C_{l,n}$ reduction of -2.67% and $C_{d,n}$ increment of 2.03% at $\xi = 0.00$. As ξ increases, $C_{l,n}$ increment increases near 0.00%. The $C_{l,n}$ variation of $\xi = 0.75$ and $\xi = 1.00$ are about -0.31%, but they are within the baseline uncertainty of 0.5%. The medium device has no obvious $C_{l,n}$ increment from $\xi = 0.00$ and $\xi = 0.50$. A +0.5% increment appears at $\xi = 0.75$, but it is soon followed by a reduction to -0.22% (within the baseline uncertainty of 0.25%). The small device has a best $C_{l,n}$ increment of +0.12% at $\xi = 0.00$, and a largest reduction of -0.18% at $\xi = 0.50$. As the spacing increases beyond $\xi = 0.50$, the small device has no obvious variation in $C_{l,n}$.

In Figure 3.14(B), the large device has a maximum $C_{d,n}$ reduction of -0.71% at $\xi = 0.25$. The $C_{d,n}$ variation of the medium device from $\xi = 0.00$ to $\xi = 0.75$ is basically within the baseline uncertainty, and at $\xi = 1.00$ it has the maximum $C_{d,n}$ reduction of -0.64%. The small devices has about +0.12% $C_{d,n}$ increment at $\xi = 0.75$ and $\xi = 1.00$.

In Figure 3.14(C), the large device has greater $C_{d,n}$ reduction except the $\xi = 0.0$, which results in generally higher lift-to-drag ratios from $\xi = 0.25$ and $\xi = 1.00$. However, the medium device at $\xi = 0.75$ has the greatest lift-to-drag increment of +0.75%. The flow visualization images of all parameters are in Appendix B-5.

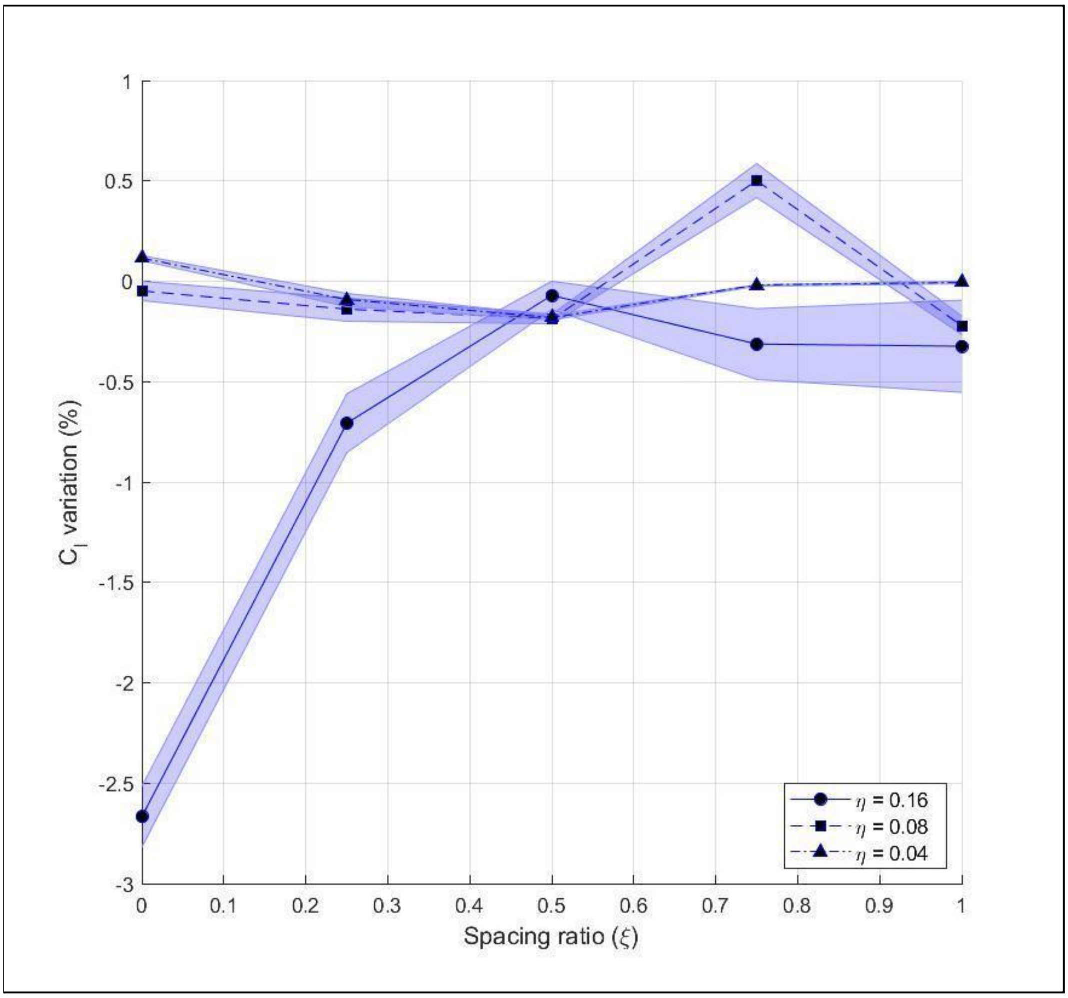

Figure 3.14(A): Normalized C_l variation of double delta serrations on 30° ramp

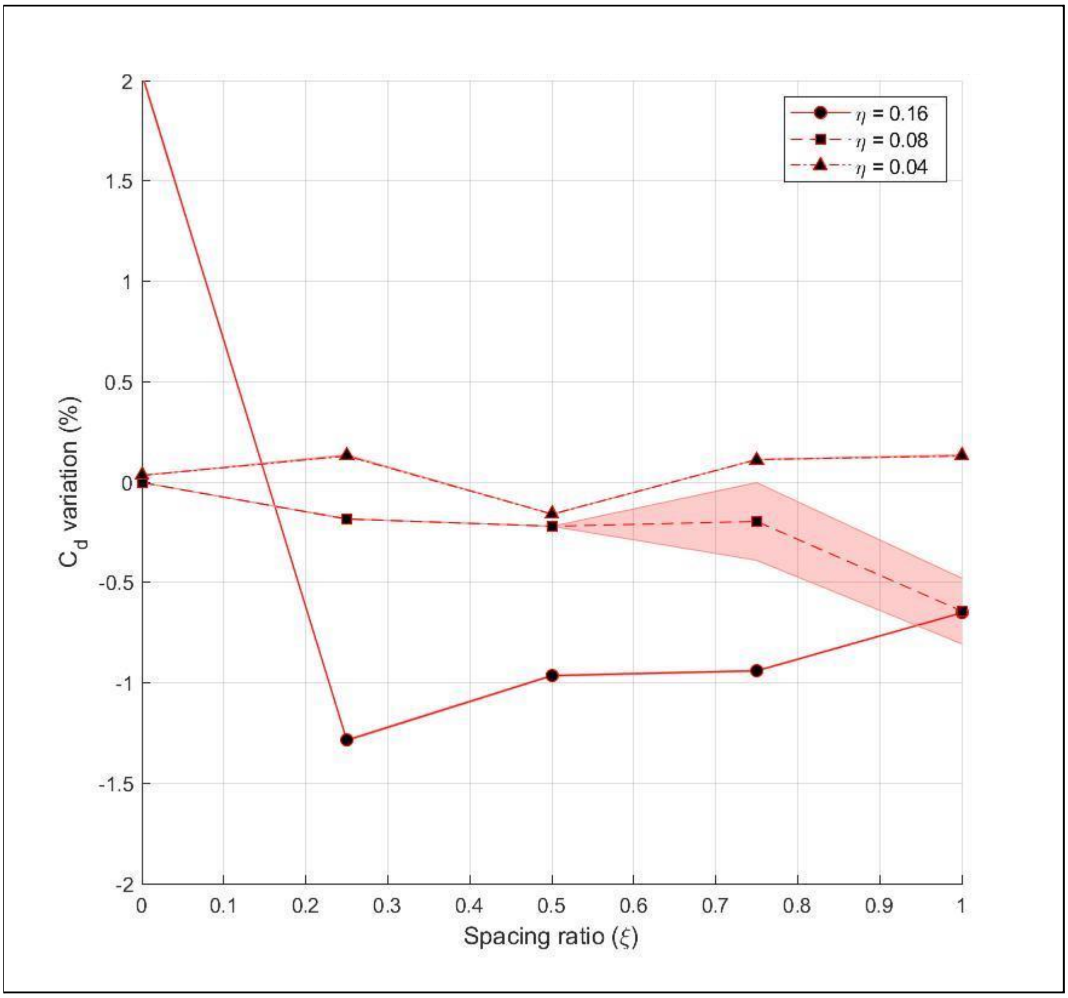

Figure 3.14(B): Normalized C_d variation of double delta serrations on 30° ramp

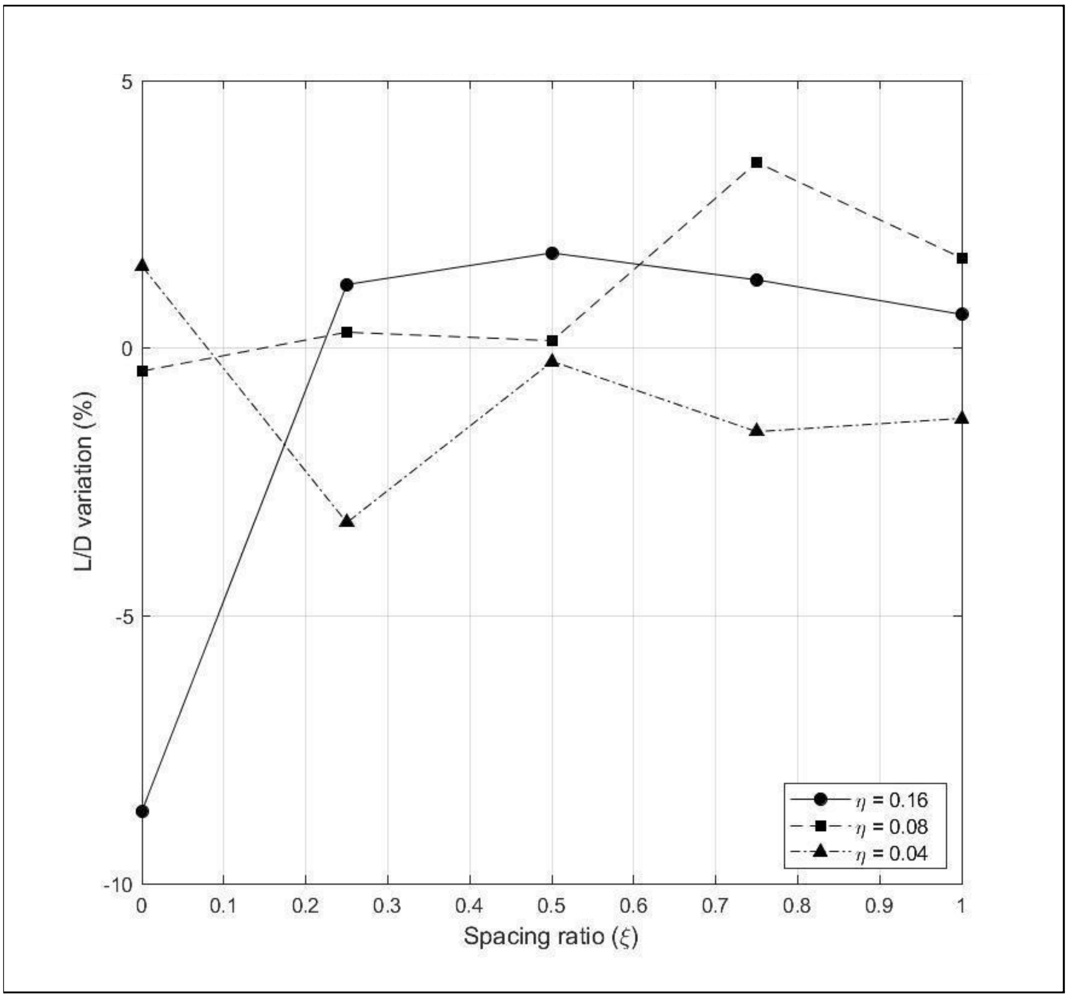

Figure 3.14(C): Lift-to-drag ratio variation of double delta serrations on 30° ramp

3.3.3 Divergent Delta Serrations on 30° Ramp

From the plots of Figure 3.15(A), (B), and (C), none of the divergent delta devices gain performance increments at this deflecting angle, but the optimum case of $C_{l,n}$ appears at $\xi = 0.50$. The $C_{d,n}$ increments are small or negative. Except the large device at $\xi = 0.75$, which has a $C_{d,n}$ increment of +0.45% , the rest of the data shows that the $C_{d,n}$ variation is near the baseline uncertainty. It is obvious that as the ramp angle increases, the divergent delta does not improve the aerodynamic performance, causing the lift-to-drag ratio to decline.

The flow visualization images of all parameters are in Appendix B-6.

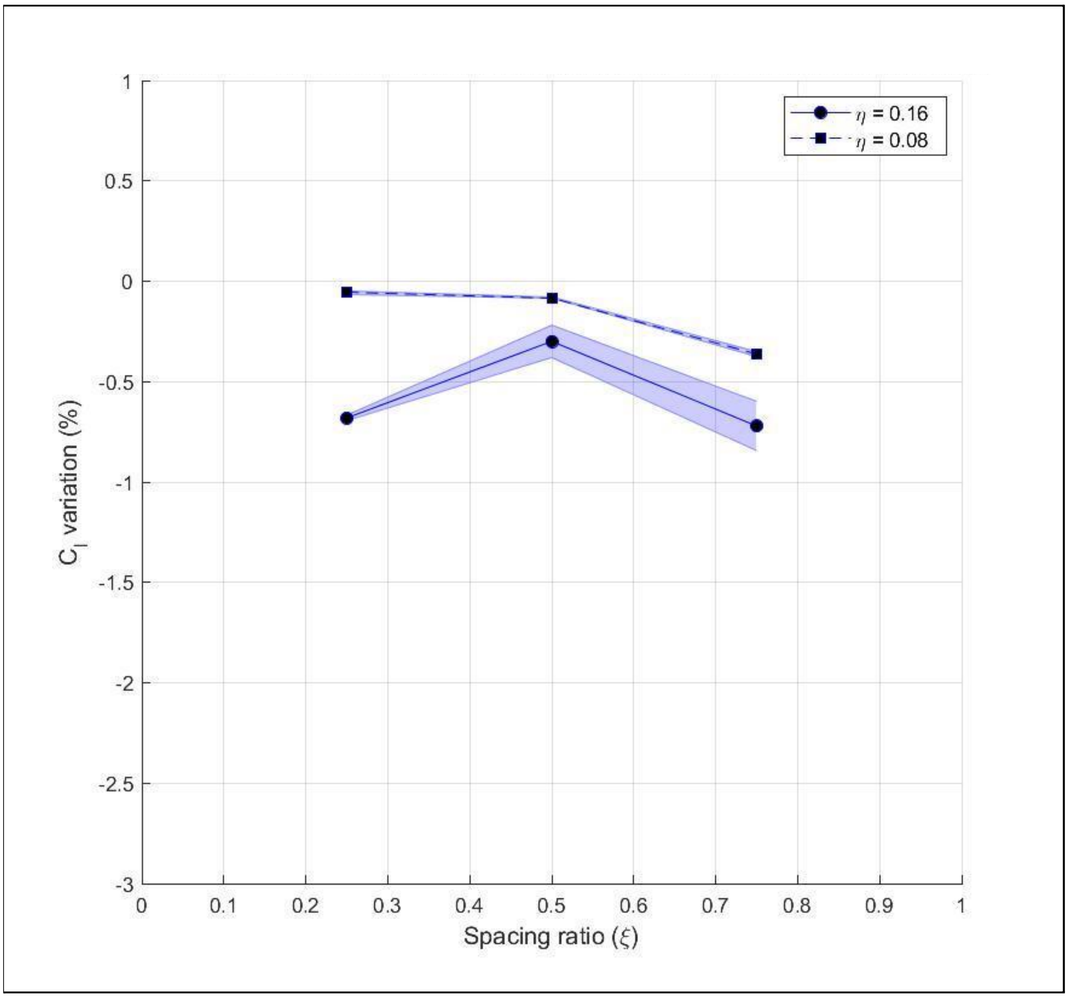

Figure 3.15(A): Normalized C_l variation of divergent delta serrations on 30° ramp

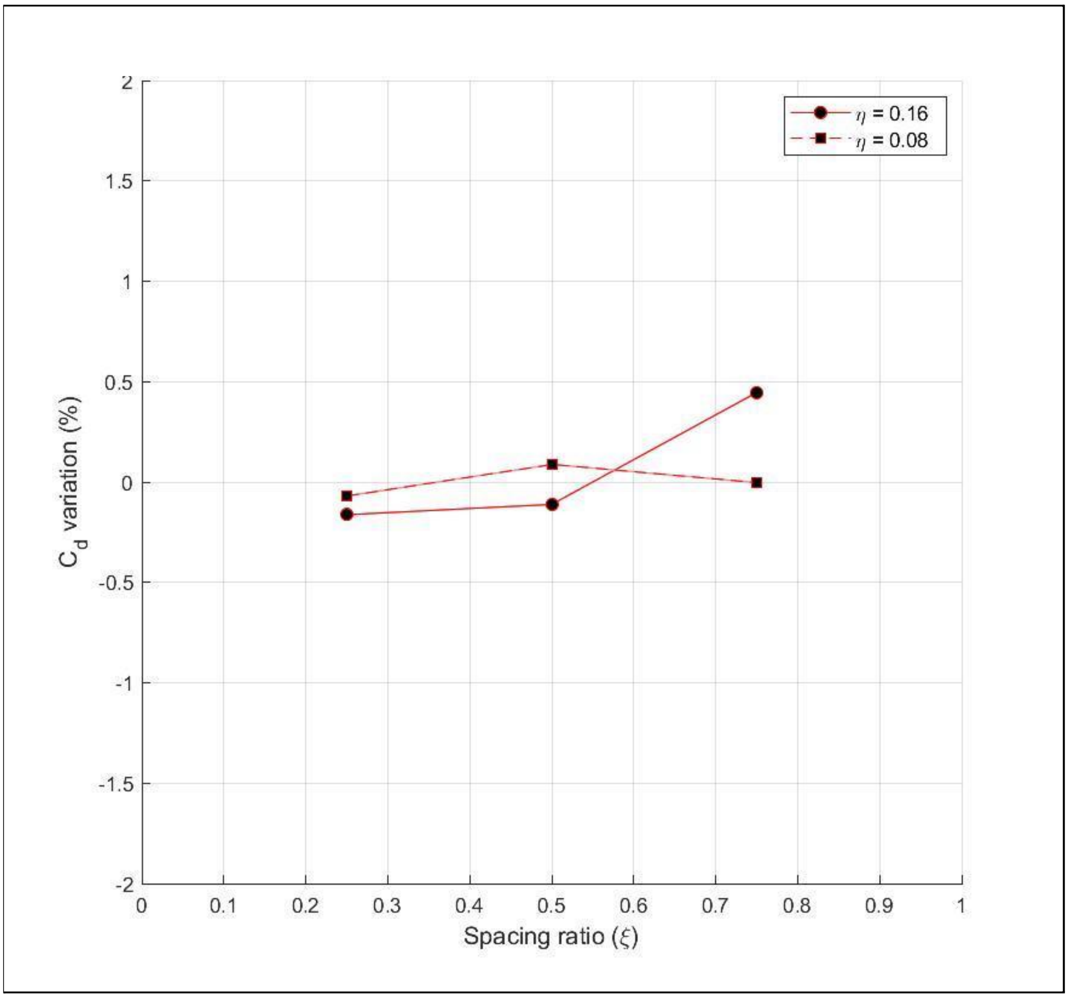

Figure 3.15(B): Normalized C_d variation of divergent delta serrations on 30° ramp

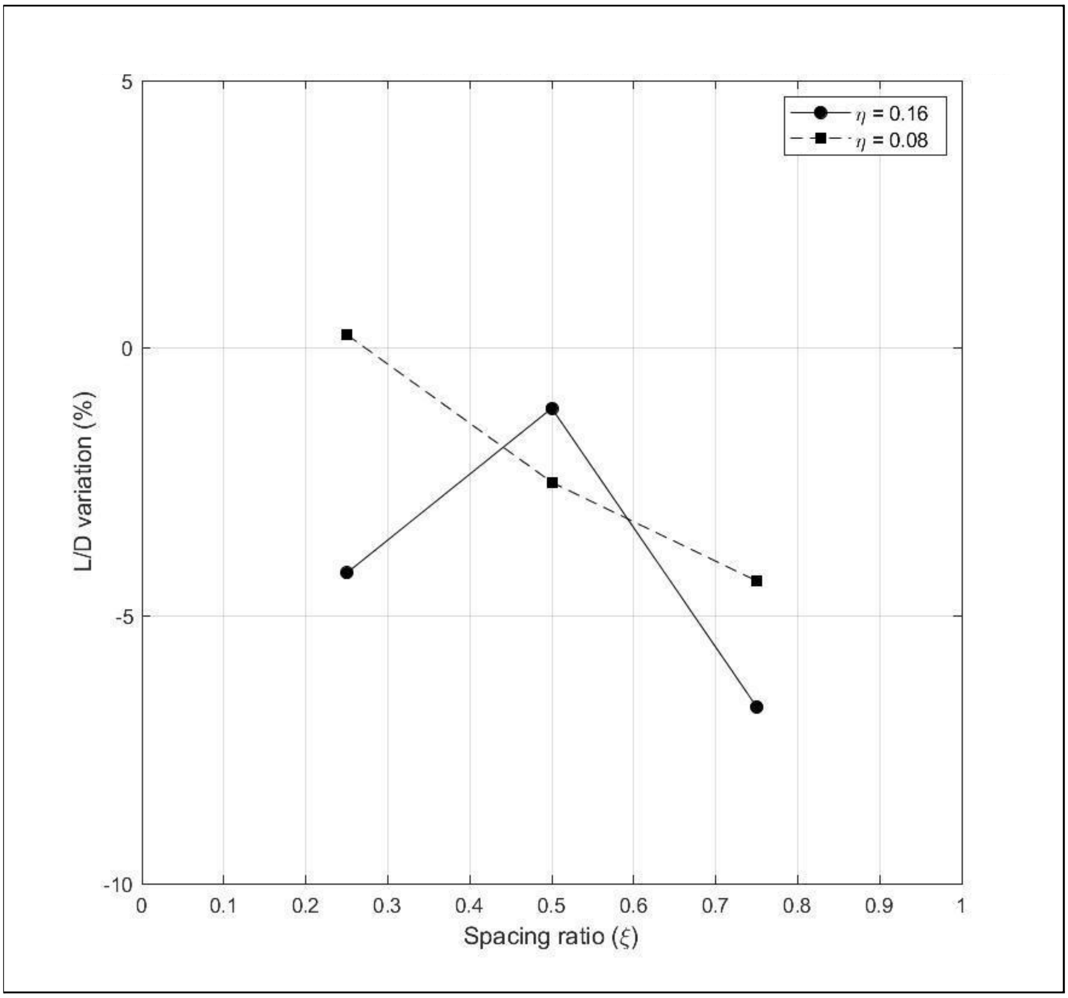

Figure 3.15(C): Lift-to-drag ratio variation of divergent delta serrations on 30° ramp

3.4 Device improvement by partitioning plates on 15° Ramp

From the results of section 3.2 and section 3.3, we observed the vortex pairs colliding with each other near the serration tips. To eliminate this unfavourable phenomenon, a partitioning plate was placed underneath the serration. The vertically sitting partitioning plate is aligned to the center line of each serration geometry as shown in Figure 1.17. Due to size limitations of the test model, the partition plate was only added to the large devices. Borrowing from the NACA duct design experience, the $\xi = 0.25$ case was selected for the optimal geometry, except the ramp angle is twice as large as the recommended 7°s.

As Figure 3.16(A) shows, the serration with the plate does not increase $C_{l,n}$ much when $\xi = 0.50$, but it does increase $C_{l,n}$ at $\xi = 0.25$ compared to Figure 3.10(A). At $\xi = 0.75$, due to the larger spacing ingesting more boundary layer fluid, $C_{l,n}$ declines -0.5%.

In Figure 3.16(B), $C_{d,n}$ declines at $\xi = 0.25$ to 0.0%, but suffers a much higher $C_{d,n}$ increment at $\xi = 0.50$ and $\xi = 0.75$.

In Figure 3.16(C), with partitioning plates at $\xi = 0.25$, we appreciably increase lift-to-drag ratio, which increases from -5.9% shown in Figure 3.10(C) to +3.2% (with partitioning plates). It is a significant improvement to balance the performance of maximum C_l and the aerodynamic efficiency.

As Figure 3.17 shows, the partition plate can effectively eliminate the stagnation spots by isolating each adjacent vortex to reduce the cancellation near the serration tip and along the serration center line. The width of the low-energy walkway is also narrower, and the attached distance over the ramp is longer compared to the regular serrations.

Some vortex pairs did not stay apart toward the downstream, and still formed the brighter stagnation points as shown in Figure 3.18 by the arrow. This problem could be a result of many factors, such as manufacturing flaws or model misalignment. For example, in Figure 3.19, we can see the brighter spots pointed by the red arrows are slightly leaning toward the inner side of the center line labeled by the solid red line. The outer vortices might be blown toward the inner vortices due to the air from the pressure side slipping through the gap between the model and the wall, causing two vortices colliding together. The flow visualization images of all divergent delta devices with the partitioning plates are presented in Appendix C.

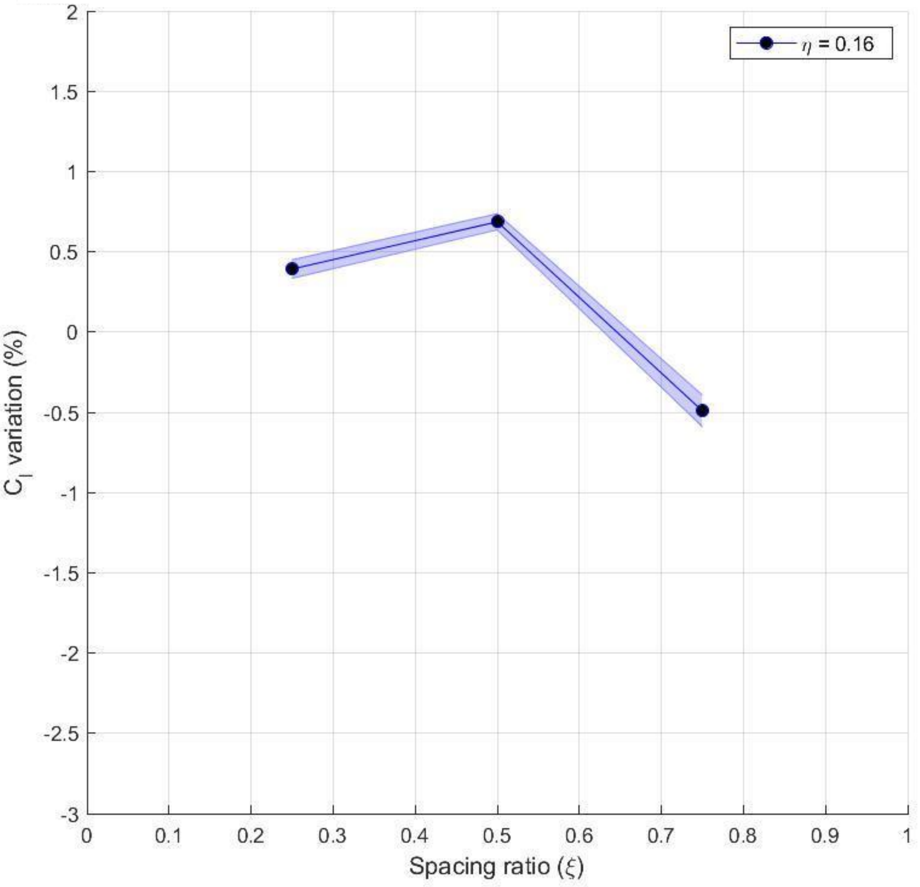

Figure 3.16(A): Normalized C_l variation of divergent delta serrations with partitioning plates on 15° ramp

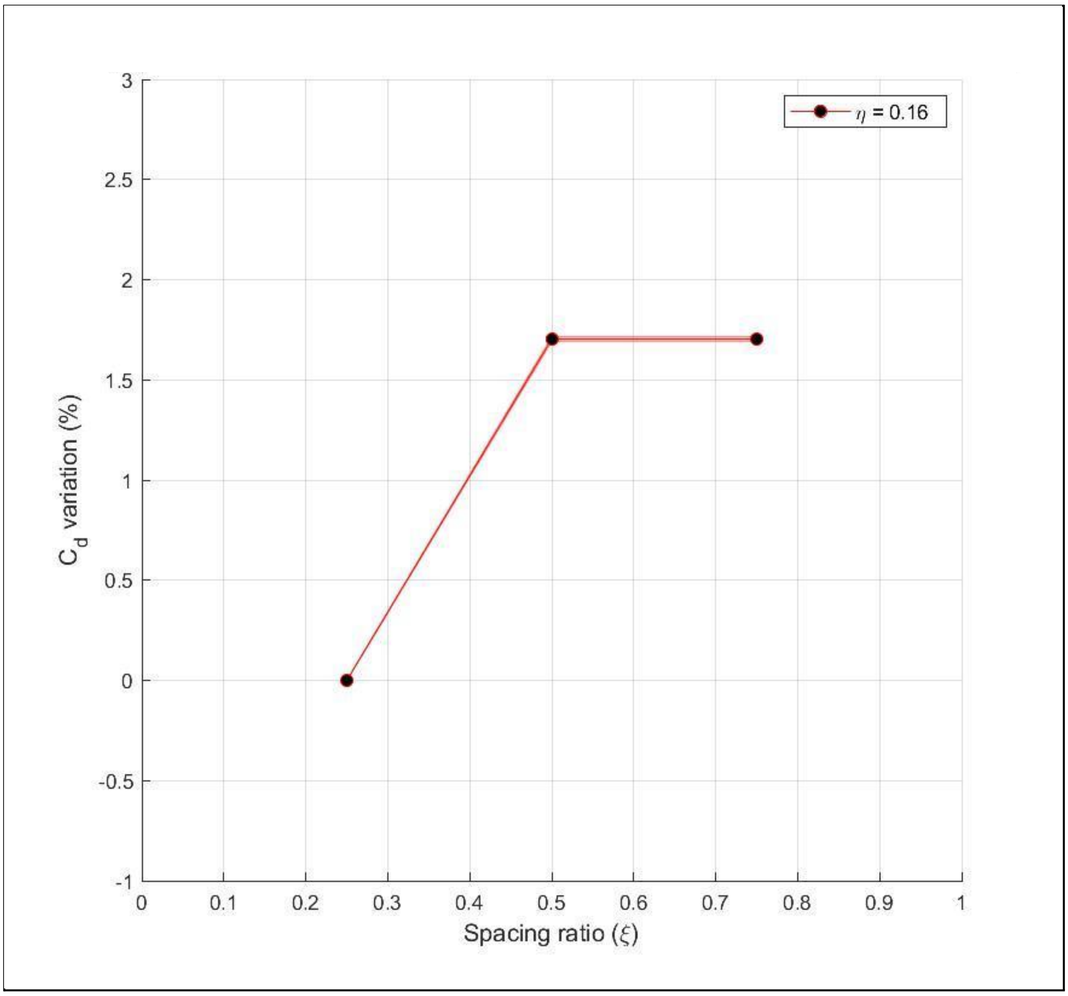

Figure 3.16(B): Normalized C_d variation of divergent delta serrations with partitioning plates on 15° ramp

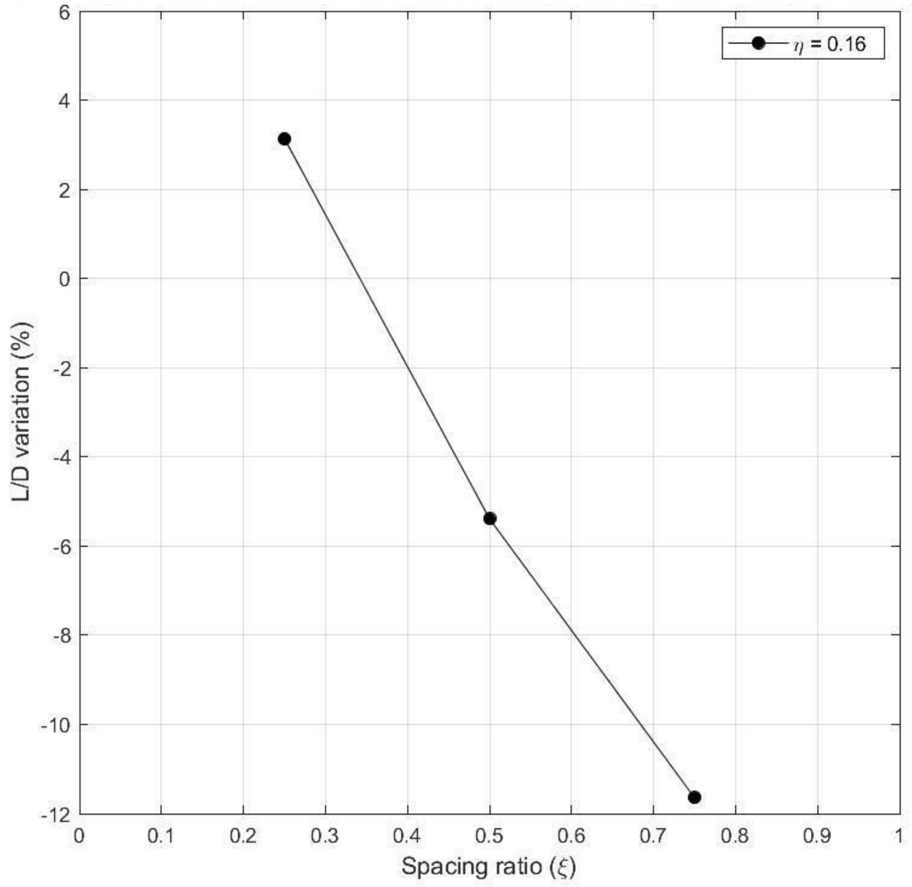

Figure 3.16(C): Lift-to-drag ratio variation of divergent delta serrations with partitioning plates on 15° ramp

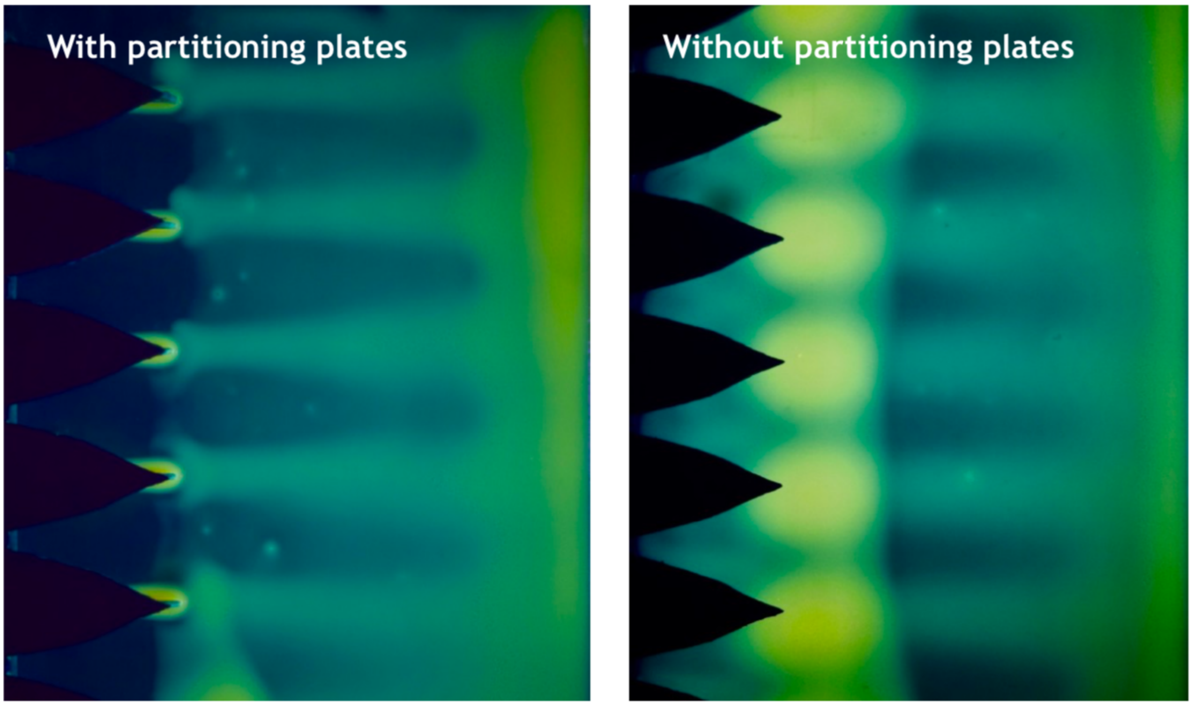

With partitioning plates

Without partitioning plates

Figure 3.17: The flow-visualization comparison of with and without the partitioning plates

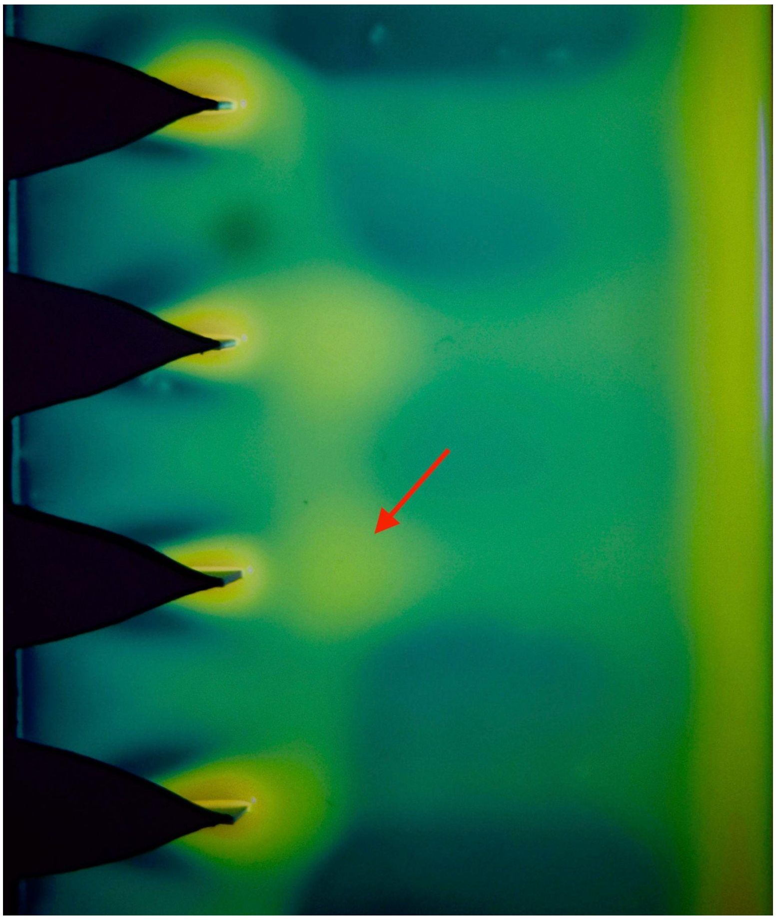

Figure 3.18: The stagnation points after the flow leaving the partitioning plates

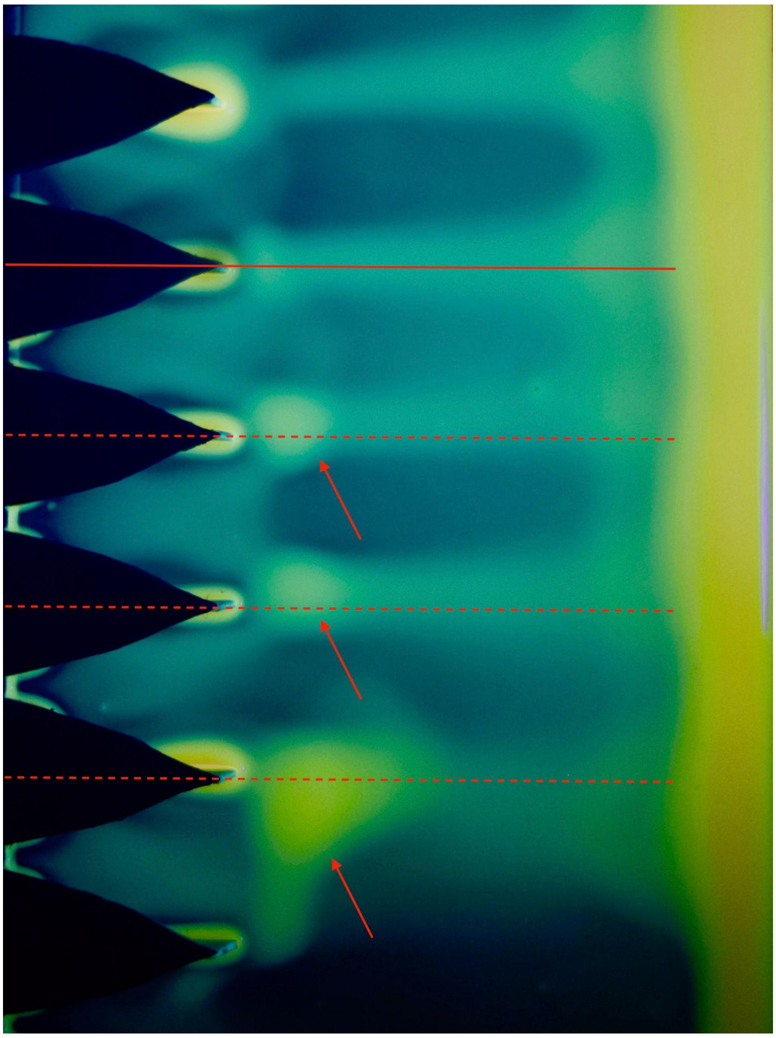

Figure 3.19: The inboard displacement of the stagnation points

3.5 Device improvement by tip treatments on 15° Ramp

It is also worthy to ask if there are other methods to prevent the tip stagnation region without using the partitioning plate. To answer this question and also try to generalize it, the sharp delta geometry at $\xi = 0.25$ was selected as the baseline model. The cut tip and the slotted tip modifications were studied. (Figure 1.18). In the following plots, Case 1 represents the baseline ramp without any serrations. Case 2 is the regular sharp delta serrations. Case 3 is the sharp delta serrations with cut tips. Case 4 is the sharp delta serrations with slotted tips. Case 5 is sharp delta serrations with partitioning plates.

Figure 3.20(A) shows that the cut tip has a +0.36% $C_{l,n}$ increment, which is much more than the -0.17% of the one without any change. It is also better than the +0.16% increment of the sharp delta serration with partitioning plates. The slotted treatment only gains a +0.02% $C_{l,n}$ increment, which is close to the baseline uncertainty.

In Figure 3.20(B), both the cut tip and the slotted tip have higher $C_{d,n}$ increments than the baseline serration, +0.50% and +0.52% respectively. The $C_{d,n}$ variation of the serration with plates has -0.48% reduction. This result in the serration with plates has a much higher lift-to-drag ratio of +4.65%. The cut tip treatment has a -0.9% lift-to-drag ratio reduction. The slotted tip performance is similar to the baseline serration of -3.12%. (Figure 3.20(C))

From the flow visualization, the cut tip has a smaller, circular stagnation spot, which is similar to the behavior of the slotted tip. However, the cut-tip treatment has a longer attached distance. The sharp delta serration with a partition plate has a teardrop-like invigorated flow field, which covers a broader ramp surface and extends further downstream. Similar to the divergent delta case, some vortex pairs did not stay apart toward the downstream and formed the brighter region as shown in Figure 3.21, which could be resulted from surface imperfection or the wall interference. The flow visualization images are presented at Appendix D.

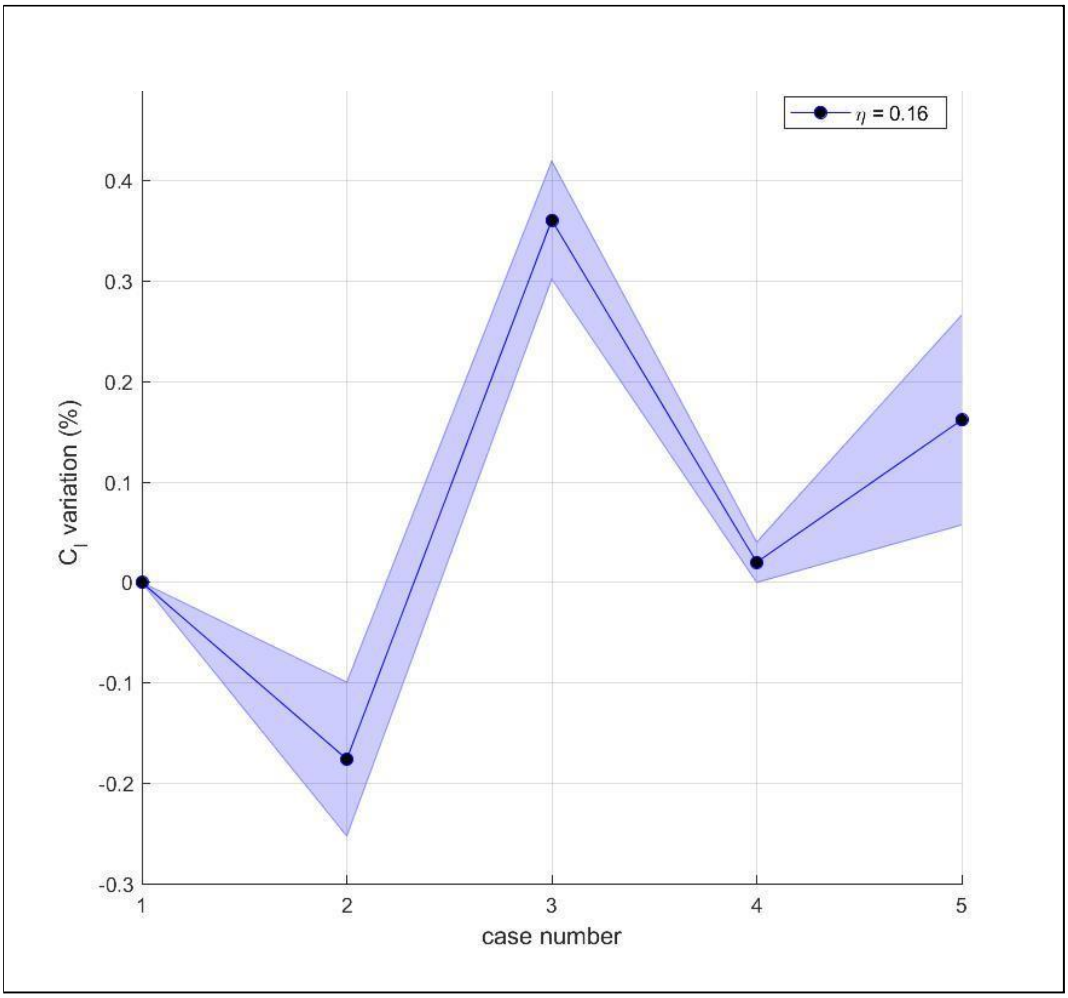

Figure 3.20(A): Normalized C_l variation of sharp delta serrations with tip treatments on 15° ramp

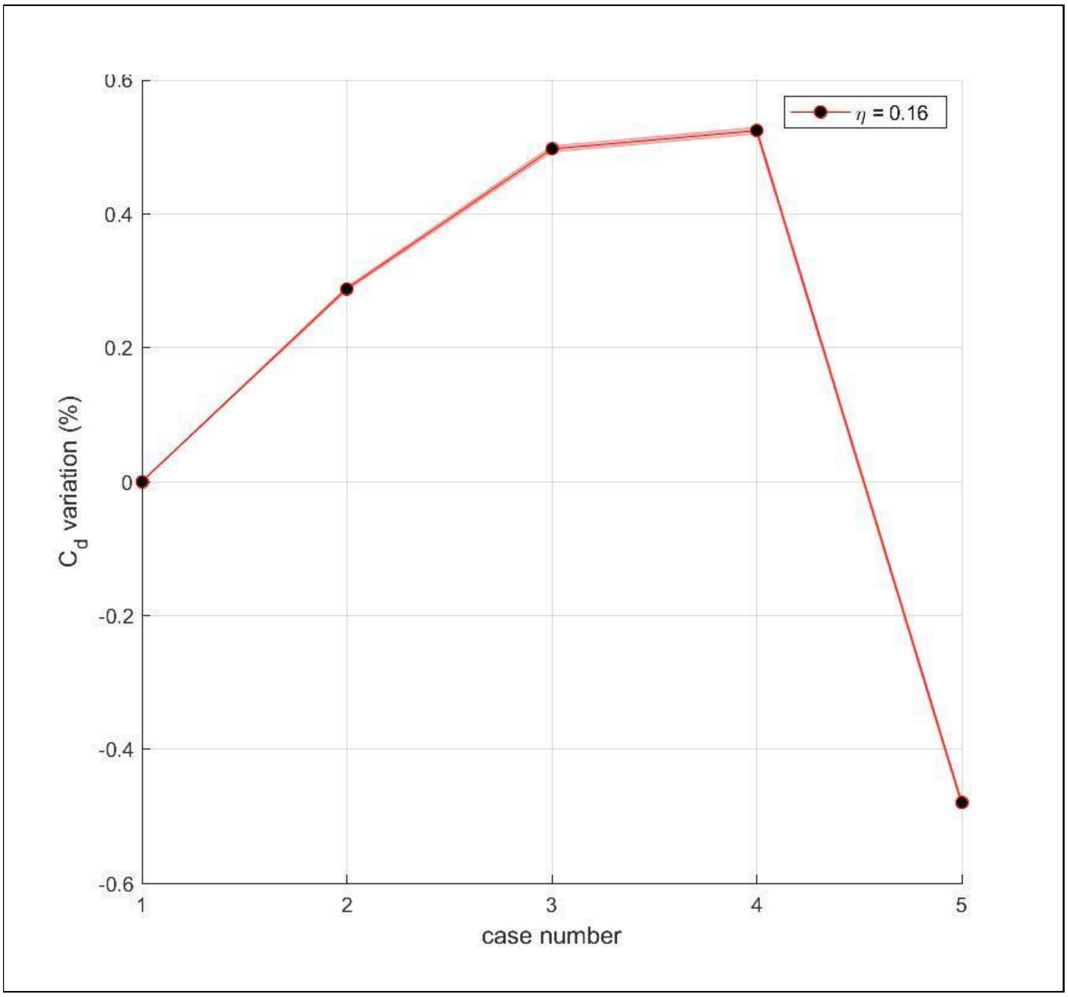

Figure 3.20(B): Normalized C_d variation of sharp delta serrations with tip treatments on 15° ramp

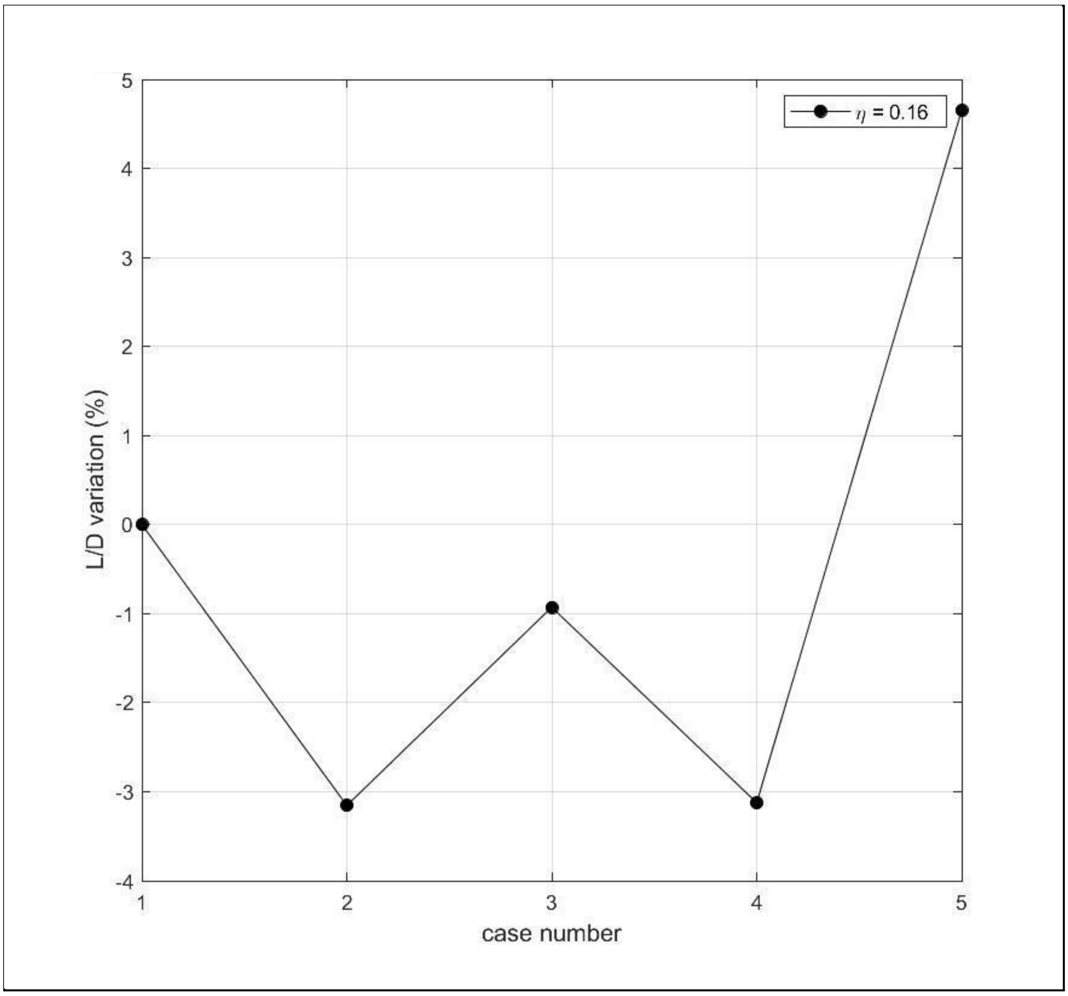

Figure 3.20(C): Lift-to-drag ratio variation of sharp delta serrations with tip treatments on 15° ramp

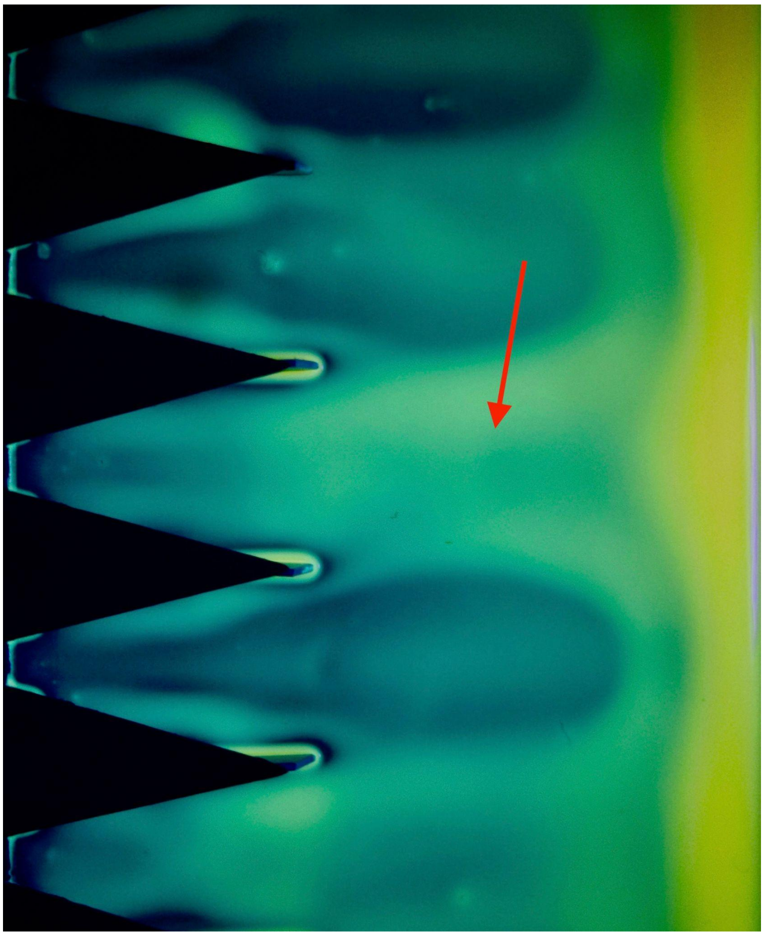

Figure 3.21: The flow imperfection

Chapter 4

CONCLUSIONS AND FUTURE WORKS

The experimental investigation tested three serration-device shapes with two geometrical parameters on 15° and 30° salient edge, back-facing ramp in low Reynolds number, laminar flow condition. Besides the regular serrations, the partitioning plates and the tip treatments are also tested on the 15° ramp to investigate further performance improvements. It was found that all geometrical parameters, ramp angles and device shapes contribute to the variation of the device performance. From the observation of flow visualization images, the stagnation points forming near the serration tips are the main contributor to the device efficiency loss. Both the partitioning plates and the cut-tip treatment show promising results to reduce the stagnation regions over the ramp. The partitioning plate keeps the vortex pair apart from each other near the serration tip. The cut-tip treatment reduces the magnitude of energy cancelation by stopping the vortex pair forming near the serration tip. The experiment conducted in section 3.4 also proved that the NACA duct analogy mentioned in section 1.2 is applicable to the serration devices with partitioning plates.

For 15° ramp, when the spacing ratio, ξ, is between 0.25 to 0.50, the lift-to-drag ratio increased about 3 to 5 % using the small devices. Furthermore, when ξ is 0.50, both the small sharp-delta and the small double-delta devices achieved about 0.07 % and 0.15 % $C_{d,n}$ reduction, respectively, while other sizes and spacings resulted in drag increment. We conclude that $\xi = 0.25$ to 0.50 is the recommended spacing for the serration devices to start the design optimization. As the η increases, devices tend to exert more drag, and therefore the lift-to-drag ratio decreases. However, for the double delta and the divergent delta devices with $\xi =$ 0.25 to 0.50 , the large devices gain more $C_{l,n}$ increment up to 1 %. The performance of serrations is also found to highly depend on the plan form geometry. The large and medium divergent-delta devices have larger lift-to-drag ratios than the sharp delta and the double delta. The large divergent delta also has an appreciable 0.6 % $C_{l,n}$ increment, which is about 4 times larger than the baseline uncertainty. The divergent delta balances the lift-to-drag ratio performance and the maximum C_l. The double delta is found hard to predict the performance. The medium double delta device has a trend of $C_{l,n}$ increment as ξ increases.

For the 30° ramp, only the medium double delta device ($\eta = 0.08$, $\xi = 0.75$) has a significant lift-to-drag ratio increment (~3%) and 0.5% $C_{l,n}$ increment. The rest of the devices all show a reduction in $C_{l,n}$, especially the divergent delta serrations. The divergent delta serrations lost the maximum $C_{l,n}$ and the lift-to-drag ratio for all values of η ($\eta = h/c$) and ξ. Different from the 15° ramp, the large devices reduced more $C_{d,n}$. From the flow visualization, the momentum transport of the vortices can not reach the ramp surface when the delecting angle is 30°.

Some general design guidelines and observations can be provided here. With partitioning plates, an adoption of the NACA duct experience optimizes the performance ($\xi = 0.25$ in this research). Without the partitioning plates, $\xi = 0.5$ is generally a safe parameter to ensure increment of the lift-to-drag ratio. The large divergent device is encouraged to use. The cut tip geometry is a promising method to increase the maximum C_l, but less improvement on the lift-to-drag ratio.

It is worthwhile to investigate the serration devices at high Reynolds numbers in turbulent flow. Due to the laminar separation bubble on the baseline ramp, the attached distance can reach up to $0.43r$ (r is the ramp length), which is close to or even greater than that of some serration devices, and therefore the variation of the comparisons are not quite significant. According to Winslow et al. [37], in even smaller Reynolds numbers of laminar flow (10,000 to 50,000), the separated flow will not immediately reattach. The performance improvement brought by the serrations could be more significant. It is also interesting to find that the small devices increase the lift-to-drag ratio on the 15° ramp, since the small devices are ingesting a relatively thicker boundary layer compared to the large devices. This question might require an even thicker boundary layer over the front plate to verify the susceptibility of the device η.

The partitioning plate method might be susceptible to the spanwise-flow effects, which causes stagnation spots to restore. If the partitioning plates can be replaced by solid walls along the serration edges, we could reduce the total pressure lost in the interstitial spaces between the partitioning plate and the serration. Since the solid wall geometry is similar to the forward wedge and the wishbone VGs, we could possibly improve the vortex pairs' structure to eliminate the cancellation near the tips.

There might be a debate of normalizing the lift and drag coefficients with the amount of the device's valleys. Even some devices have inferior normalized performance (i.e. the small double delta $\xi = 0.50$, on 15° ramp comparing to the large device), they could actually provide more performance improvement if we look at the plot of the unit-span data. This discrepancy is due to the difference in the sizes and the geometry, and therefore results from the amount of a specific device per unit span. While useful for practical applications, the data plots per unit span do not help us understand the fundamentals of the devices. The unit-span plots are attached in Appendix E for reference.

Lastly, since the serration device can be made by thin sheets of materials, it is light weight and cost effective to install on light aircraft or UAVs. The device is similar to the VG that can be seen as an independent add-on to the aircraft. This feature gives aircraft manufacturers additional design freedom, and can be easily retrofitted to existing aircraft. By obtaining a general rule of thumb of the device parameters, we can simplify the design process of high-lift systems. The serration device might be able to work with single-slotted flaps like the micro VGs in Lin et al. 's research [17]. Because the serration device is an external device, unlike VGs stored between the space of the flap and the main wing, we will find it easier to be placed on the skin and stay submerged all the time. The challenge would be: To maximize the device efficiency, the partitioning plates should be adopted, but it will not be as simple as just adding sheets of serrations due to the storage of the plates.

BIBLIOGRAPHY

[1] Van Dam, C.P. "The Aerodynamic Design of Multi-element High-lift Systems for Transport Airplanes." Progress in Aerospace Sciences 38, no. 2 (2002): 101-44.

[2] J. Roskam. New airfoils and higher wing loadings: a new look at general aviation airplane design. TU Delft, 1974.

[3] Dave Daniel. (October 23, 2017). "All in a Flap". <https://ultralightdesign.wordpress.com/2017/10/23/all-in-a-flap/>

[4] Thacker A, Aubrun S, Leroy A, Devinant P. "Effects of sup- pressing the 3D separation on the rear slant on the flow structures around an ahmed body." J Wind Eng Ind Aerodyn (2012): 107–108:237–243

[5] Debien A, Aubrun S, Mazellier N, Kourta A. "Salient and smooth edge ramps inducing turbulent boundary layer separa- tion: flow characterization for control perspective." C R Méc (2014): 342(6):356–362

[6] Chris Heintz, Official Guide to Experimental Aircraft, 2000

[7] Andy Lennon, R/C model aircraft design, 1996

[8] Photo of a SkyRanger. <bydanjohnson.com/pilotreport/sky-ranger-defines-a-new-niche/.jpeg>

[9] Photo of a Kitfox S7. <www.kitplanes.com/kitfox-vs-kitfox/.jpeg>

[10] Schubauer, G. B, and Spangenberg, W. G. "Forced Mixing in Boundary Layers." Journal of Fluid Mechanics 8, no. 1 (1960): 10-32.

[11] Stephens AV, Collins GA. Turbulent boundary layer control by ramps or wedges. ARL (Australia), Report A.85, 1954.

[12] Tanner LH, Pearcey HH, Tracy CM. Vortex generators; their design and their effects on turbulent boundary layers. ARC (UK) Report 16487, 1954.

[13] Wheeler GO. Means of maintaining attached flow of a flow medium. U.S. Patent Number: 4 455 045, June 1984.

[14] Wheeler GO. Low drag vortex generators. U.S. Patent Number: 5 058 837, October 1991.

[15] Howard, F. G, Lin, J. C, and Selby, G. V. Exploratory Study of Vortex-generating Devices for Turbulent Flow Separation Control, 1991.

[16] Lin, John Ching-Nien. Control of Low-speed Turbulent Separated Flow over a Backward-facing Ramp, 1992.

[17] Lin, John C, Robinson, Stephen K, McGhee, Robert J, and Valarezo, Walter O. "Separation Control on High-lift Airfoils via Micro-vortex Generators." Journal of Aircraft 31, no. 6 (1994): 1317-323.

[18] Jukes, Timothy N, and Choi, Kwing-So. "Dielectric-barrier-discharge Vortex Generators: Characterisation and Optimisation for Flow Separation Control." Experiments in Fluids 52, no. 2 (2012): 329-45.

[19] Kourta, Azeddine & Thacker, Adrien & Joussot, Romain. "Analysis and characterization of ramp flow separation." Experiments in Fluids. 56. (2015) 10.1007/s00348-015-1968-9.

[20] Howe, M.S., “Noise produced by a sawtooth trailing edge,” The Journal of the Acoustical Society of America, Vol.90, No.1, 1991, pp. 482.

[21] Gruber, M., Azarpeyvand, M., andJoseph, P., “Airfoil trailing edge noise reduction by the introduction of sawtooth slotted trailing edge geometries,” Proceedings of 20th International Congress on Acoustics, 2010, pp. 1–9.

[22] Jones, L. and Sandberg, R., “Numerical Investigation of Airfoil Self-Noise Reduction by Addition of Trailing-Edge Serra- tions,” 16th AIAA/CEAS Aeroacoustics Conference, 2010, pp. 1–23.

[23] Sandberg, R.D. and Jones, L.E., “Direct numerical simulations of low Reynolds Number Flow Over Airfoil With Trailing-edge serrations,” Journal of Sound and Vibration, Vol. 330, No. 16, 2011, pp. 3818–3831.

[24] Moreau, D., Brooks, L., and Doolan, C., “On the noise reduction mechanism of a flat plate serrated trailing edge at low-to- moderate Reynolds number,” 18th AIAA/CEAS Aeroacoustics Conference (33rd AIAA Aeroacoustics Conference), 2012, pp. 1–20.

[25] Liu, Xiao, Kamliya Jawahar, Hasan, Azarpeyvand, Mahdi, and Theunissen, Raf. "Aerodynamic Performance and Wake Development of Airfoils with Serrated Trailing-Edges." AIAA Journal 55, no. 11 (2017): 3669-680.

[26] The group meeting with Dr. Robert E. Breidenthal

[27] Mossman, Emmet A., Randall, Lauros M., and United States. National Advisory Committee for Aeronautics. An Experimental Investigation of the Design Variables for NACA Submerged Duct Entrances. NACA Research Memorandum ; A7I30. Washington, D.C.: National Advisory Committee for Aeronautics, 1948.

[28] Gault, Donald E. An Experimental Investigation of NACA Submerged Air Inlets on a 1/5-scale Model of a Fighter Airplane, 1947.

[29] Delany, N.K., 1948, “An Investigation of Submerged Air Inlets on a -Scale Model of a Fighter-Type Airplane,” NACA RM A8A20, National Advisory Committee on Aeronautics.

[30] Hime, Leticia & CELIS, Cesar & Figueira da Silva, Luís Fernando & Ferreira, Sandro & Batista de Jesus, Antonio & Takase, Viviam & Vinagre, Harry. (2005). A Review of the Characteristics of Submerged Air Intakes.

[31] Mossman, Emmet A, Davis, Wallace F, Randall, Lauros M, and Frick, Charles W. An Experimental Investigation of NACA Submerged-Duct Entrances, 1945.

[32] Taylor, Robert A. Some Effects of Side-wall Modifications on the Drag and Pressure Recovery of an NACA Submerged Inlet at Transonic Speeds, 1952.

[33] Spreiter, John R, and Sacks, Alvin H. Theoretical Investigation of Submerged Inlets at Low Speeds, 1951.

[34] Anderson, John D. Introduction to Flight. 6th ed. Boston: McGraw-Hill, 2008.

[35] Mudimeli, Dakalo. (2018). Boundary Layer Separation from a Circular Cylinder. 10.13140/RG.2.2.36111.84642.

[36] Rütten, Markus & Wendland, Holger. (2012). Performance Enhancement of Auxiliary Air Intakes Using Vortex Generators. 10.2514/6.2012-57.

[37] Winslow, Justin, Otsuka, Hikaru, Govindarajan, Bharath, and Chopra, Inderjit. "Basic Understanding of Airfoil Characteristics at Low Reynolds Numbers." Journal of Aircraft 55, no. 3 (2018): 1050-061.

[38] Yang, Zifeng, and Hu, Hui. "Laminar Flow Separation and Transition on a Low-Reynolds-Number Airfoil." Journal of Aircraft 45, no. 3 (2008): 1067-070.

[39] Gad-el-Hak, Mohamed. "Micro-Air-Vehicles: Can They Be Controlled Better?" Journal of Aircraft 38, no. 3 (2001): 419-29.

Appendix A

Data of the experimental results

A-1: The sharp delta devices on 15° ramp

Experimental Data (15 degree ramp)					
η	ξ	Sharp delta serration			
		Normalization factor	Normalized Baseline Uncertainty (%)	Cl variation (%)	Cd variation (%)
0.16	0.00	9	0.11	-0.16	0.79
	0.25	7	0.14	-0.17	0.26
	0.50	6	0.17	-0.30	0.90
	0.75	4	0.25	-0.43	0.97
	1.00	3	0.33	-0.37	1.29
0.08	0.00	19	0.05	0.07	0.29
	0.25	15	0.07	-0.03	0.12
	0.50	12	0.08	0.13	0.31
	0.75	10	0.10	-0.02	0.19
	1.00	9	0.11	0.19	0.21
0.04	0.00	39	0.03	0.03	-0.05
	0.25	30	0.03	0.10	0.00
	0.50	25	0.04	-0.05	-0.07
	0.75	22	0.05	-0.01	0.08
	1.00	19	0.05	0.01	0.09

A-2: The double delta devices on 15° ramp

Experimental Data (15 degree ramp)					
η	ξ	Double delta serration			
		Normalization factor	Normalized Baseline Uncertainty (%)	Cl variation (%)	Cd variation (%)
0.16	0.00	2	0.50	0.04	1.80
	0.25	2	0.50	-0.00	2.70
	0.50	2	0.50	1.02	0.87
	0.75	2	0.50	-1.73	0.87
	1.00	2	0.50	-1.94	0.00
0.08	0.00	9	0.11	0.05	1.02
	0.25	7	0.14	0.44	0.25
	0.50	6	0.17	0.51	0.61
	0.75	5	0.20	0.92	0.37
	1.00	4	0.25	1.07	0.85
0.04	0.00	19	0.05	0.02	0.20
	0.25	15	0.07	-0.01	0.12
	0.50	12	0.08	0.24	-0.15
	0.75	12	0.08	0.18	0.00
	1.00	10	0.10	0.02	0.00

A-3: The divergent devices on 15° ramp

Experimental Data (15 degree ramp)					
η	ξ	Divergent delta serration			
		Normalization factor	Normalized Baseline Uncertainty (%)	Cl variation (%)	Cd variation (%)
0.16	0.00	N/A	N/A	N/A	N/A
	0.25	8	0.13	-0.03	0.74
	0.50	6	0.17	0.57	0.25
	0.75	6	0.17	0.23	1.27
	1.00	N/A	N/A	N/A	N/A
0.08	0.00	N/A	N/A	N/A	N/A
	0.25	19	0.05	0.09	0.49
	0.50	15	0.07	0.17	0.00
	0.75	12	0.08	0.00	0.13
	1.00	N/A	N/A	N/A	N/A
0.04	0.00	N/A	N/A	N/A	N/A
	0.25	N/A	N/A	N/A	N/A
	0.50	N/A	N/A	N/A	N/A
	0.75	N/A	N/A	N/A	N/A
	1.00	N/A	N/A	N/A	N/A

A-4: The sharp delta devices on 30° ramp

Experimental Data (30 degree ramp)					
η	ξ	Sharp delta serration			
		Normalization factor	Normalized Baseline Uncertainty (%)	Cl variation (%)	Cd variation (%)
0.16	0.00	9	0.11	-0.34	0.15
	0.25	7	0.14	-0.47	-0.41
	0.50	6	0.17	-0.35	0.44
	0.75	4	0.25	-0.39	0.42
	1.00	3	0.33	-0.78	0.54
0.08	0.00	19	0.05	-0.04	0.00
	0.25	15	0.07	-0.13	-0.15
	0.50	12	0.08	-0.09	-0.41
	0.75	10	0.10	-0.08	0.00
	1.00	9	0.11	-0.10	0.08
0.04	0.00	39	0.03	-0.01	0.02
	0.25	30	0.03	-0.00	-0.06
	0.50	25	0.04	-0.02	-0.05
	0.75	22	0.05	0.01	0.09
	1.00	19	0.05	-0.03	0.17

A-5: The double delta devices on 30° ramp

Experimental Data (30 degree ramp)					
η	ξ	Double delta serration			
		Normalization factor	Normalized Baseline Uncertainty (%)	Cl variation (%)	Cd variation (%)
0.16	0.00	2	0.50	-2.67	2.03
	0.25	2	0.50	-0.71	-1.29
	0.50	2	0.50	-0.07	-0.96
	0.75	2	0.50	-0.31	-0.94
	1.00	2	0.50	-0.32	-0.65
0.08	0.00	9	0.11	-0.05	0.00
	0.25	7	0.14	-0.14	-0.19
	0.50	6	0.17	-0.19	-0.22
	0.75	5	0.20	0.50	-0.19
	1.00	4	0.25	-0.22	-0.64
0.04	0.00	19	0.05	0.12	0.03
	0.25	15	0.07	-0.09	-0.09
	0.50	12	0.08	-0.18	-0.16
	0.75	12	0.08	-0.02	0.11
	1.00	10	0.10	-0.00	0.13

A-6: The divergent devices on 30° ramp

Experimental Data (30 degree ramp)					
η	ξ	Divergent delta serration			
		Normalization factor	Normalized Baseline Uncertainty (%)	Cl variation (%)	Cd variation (%)
0.16	0.00	N/A	N/A	N/A	N/A
	0.25	8	0.13	-0.68	-0.16
	0.50	6	0.17	-0.30	-0.11
	0.75	6	0.17	-0.72	0.45
	1.00	N/A	N/A	N/A	N/A
0.08	0.00	N/A	N/A	N/A	N/A
	0.25	19	0.05	-0.06	0.00
	0.50	15	0.07	-0.08	0.09
	0.75	12	0.08	-0.36	0.00
	1.00	N/A	N/A	N/A	N/A
0.04	0.00	N/A	N/A	N/A	N/A
	0.25	N/A	N/A	N/A	N/A
	0.50	N/A	N/A	N/A	N/A
	0.75	N/A	N/A	N/A	N/A
	1.00	N/A	N/A	N/A	N/A

Appendix B

Flow visualization images

B-1: The sharp delta devices on 15° ramp

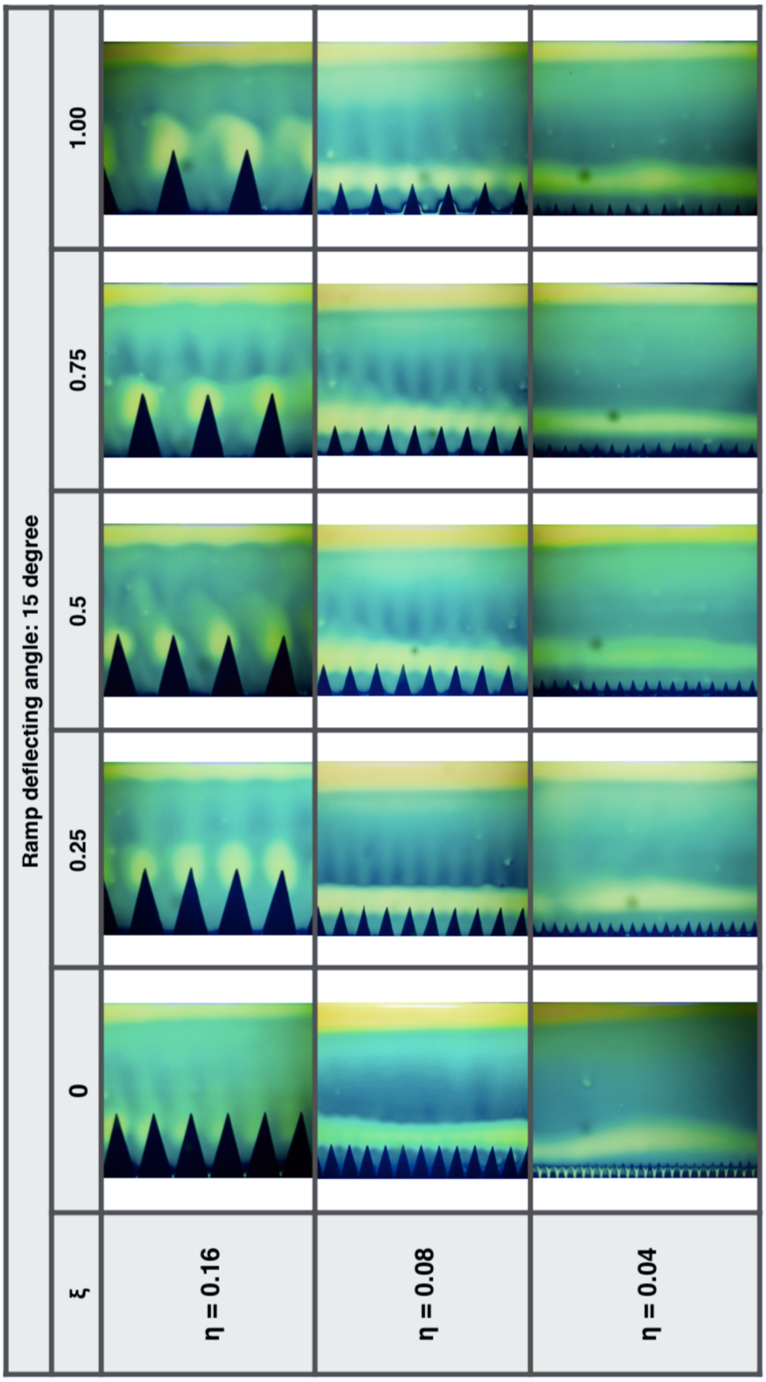

B-2: The double delta devices on 15° ramp

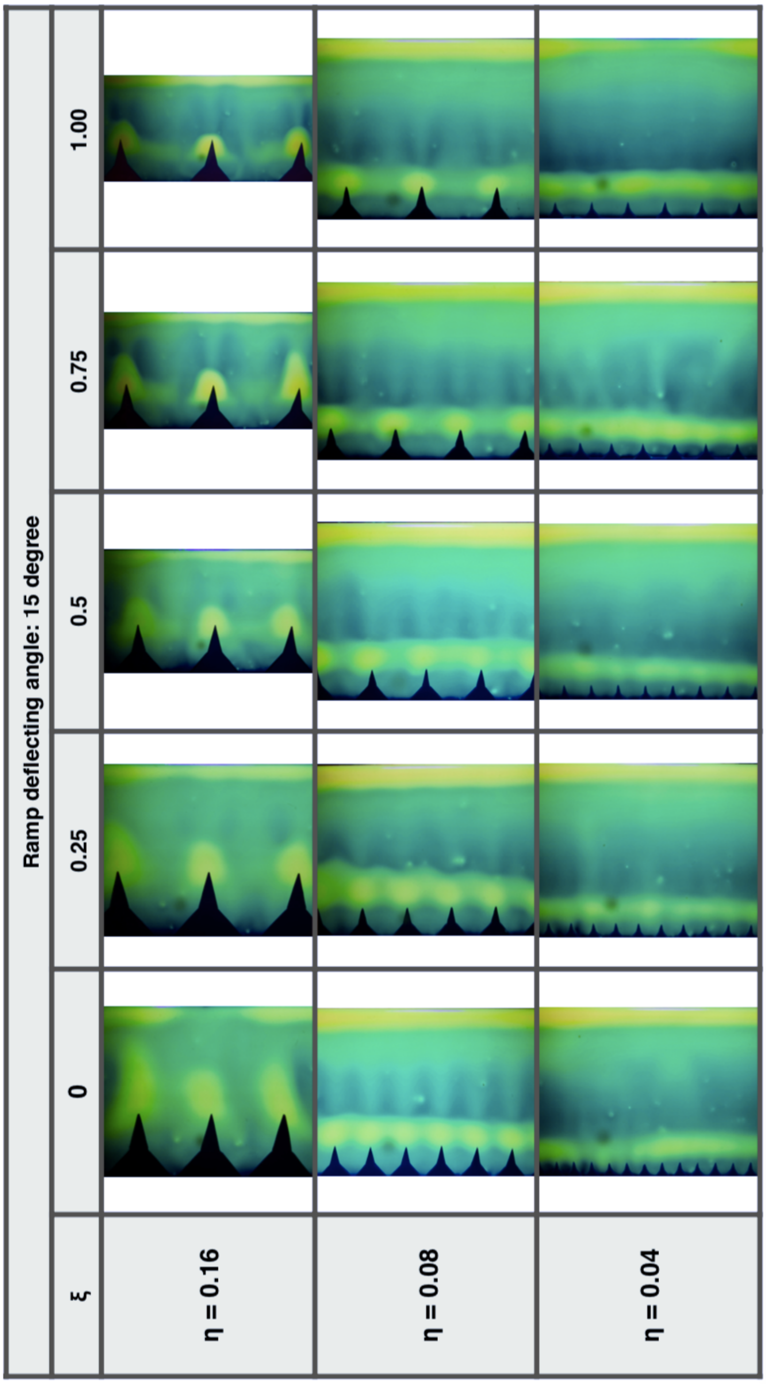

B-3: The divergent devices on 15° ramp

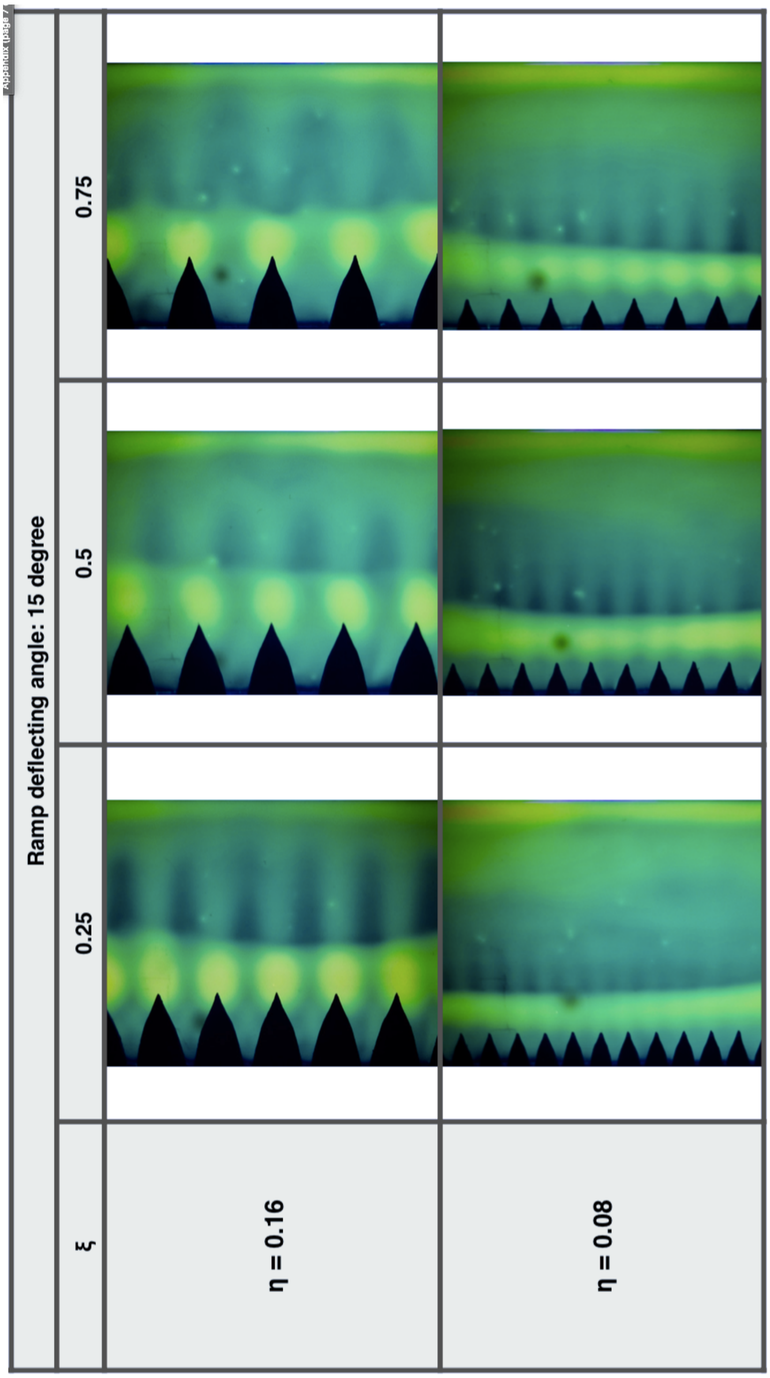

B-4: The sharp delta devices on 30° ramp

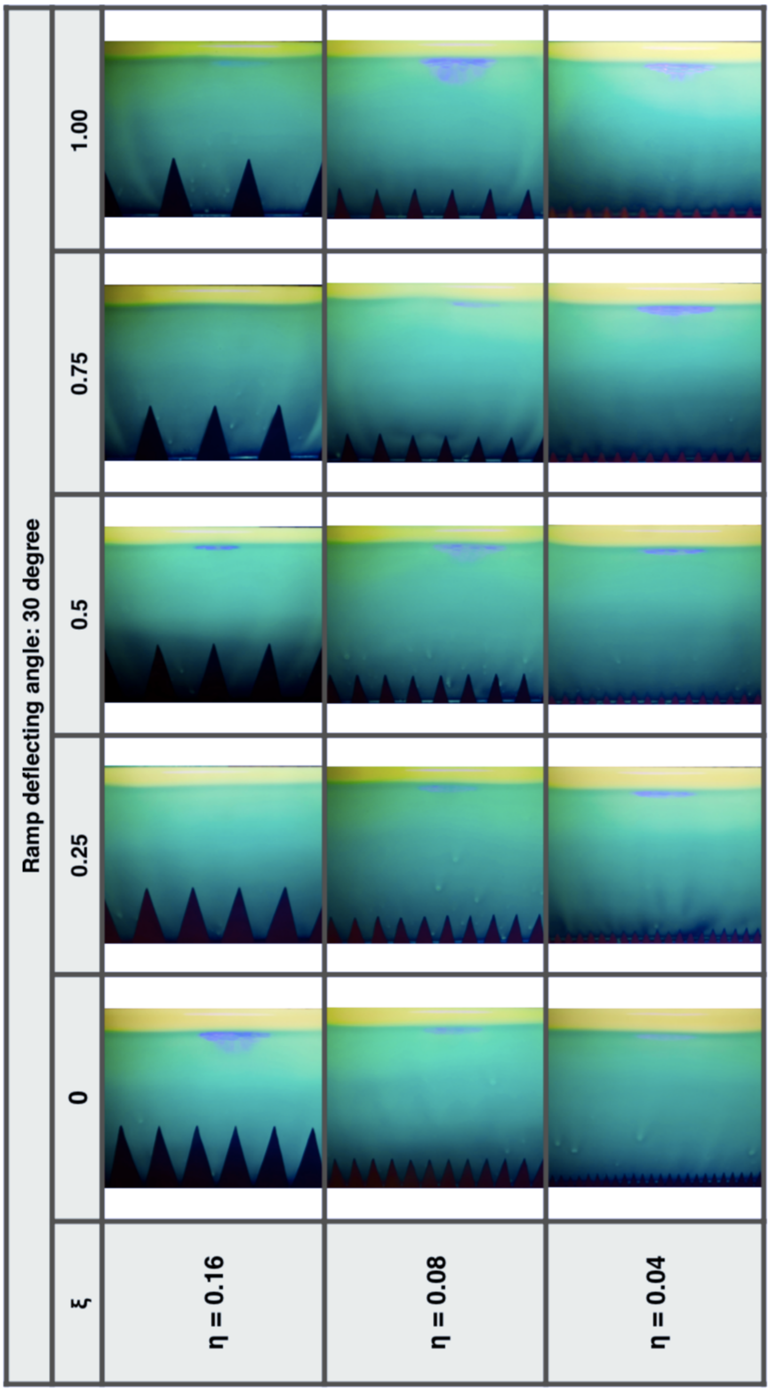

B-5: The double delta devices on 30° ramp

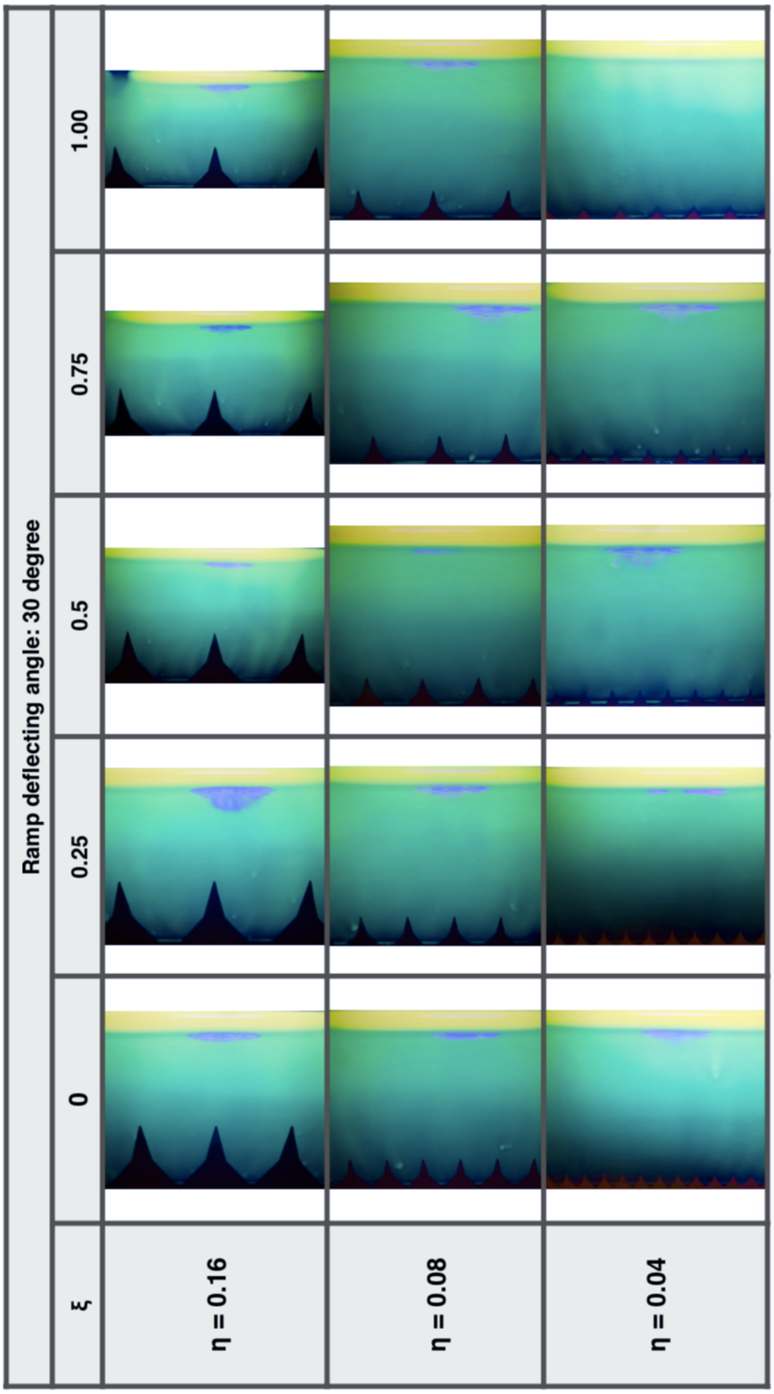

B-6: The divergent devices on 30° ramp

Ramp deflecting angle: 30 degree			
ξ	**0.25**	**0.5**	**0.75**
η = 0.16	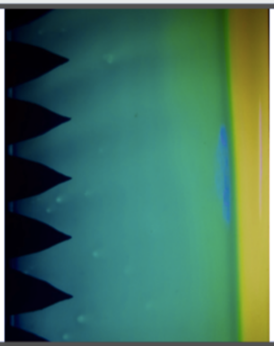	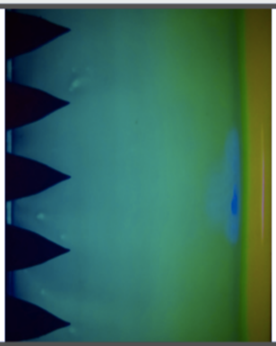	
η = 0.08		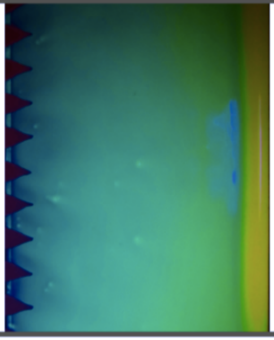	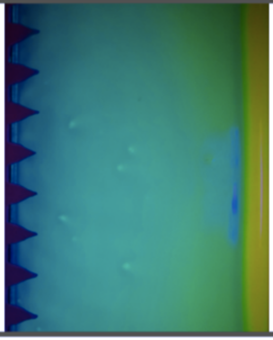

Appendix C

Flow visualization images of the improvement by partitioning plates

Ramp deflecting angle: 15 degree			
ξ	0.25	0.5	0.75
Divergent delta serration ($\eta = 0.16$) with the partitioning plate installed	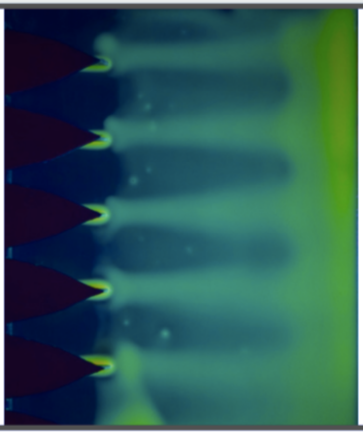	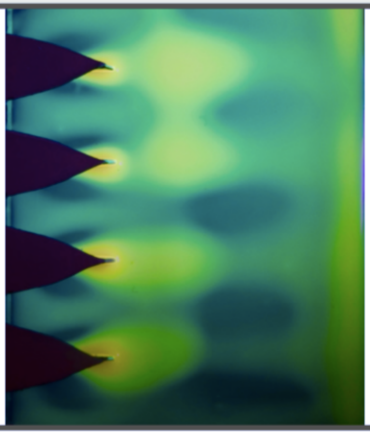	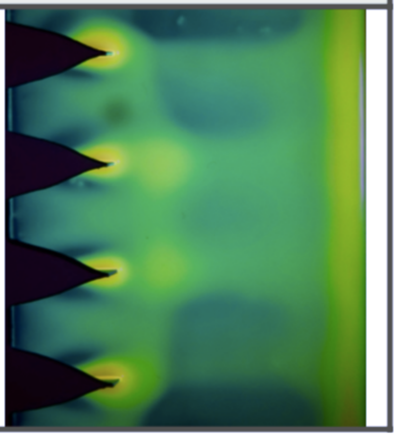

Appendix D

Flow visualization images of the improvement by tip treatments

Ramp deflecting angle: 15 degree				
Treatments on the sharp delta serrations ($\eta = 0.16$)	**No treatments**	**Cut tips**	**Slotted tips**	**Partitioning plates**
ξ: 0.25	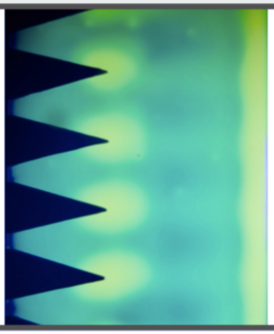	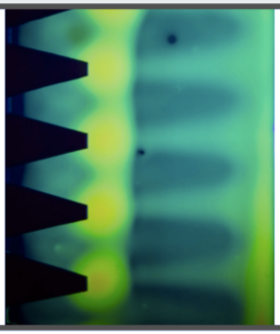	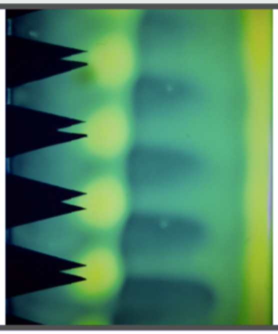	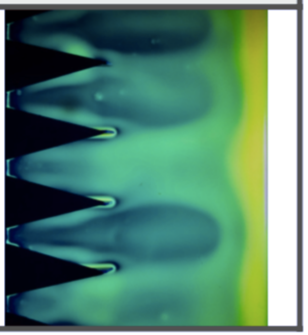

Appendix E

Lift and drag variation plots per unit span

E-1: The sharp delta devices on 15° ramp

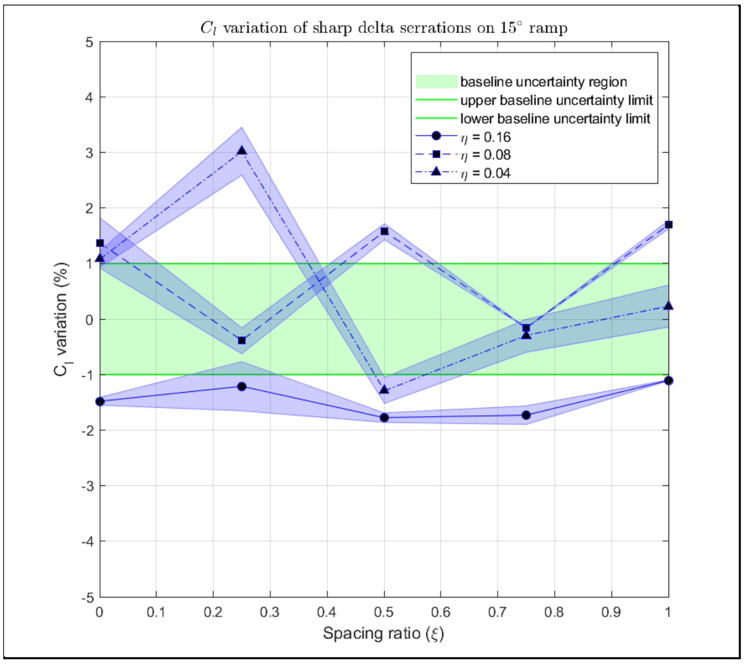

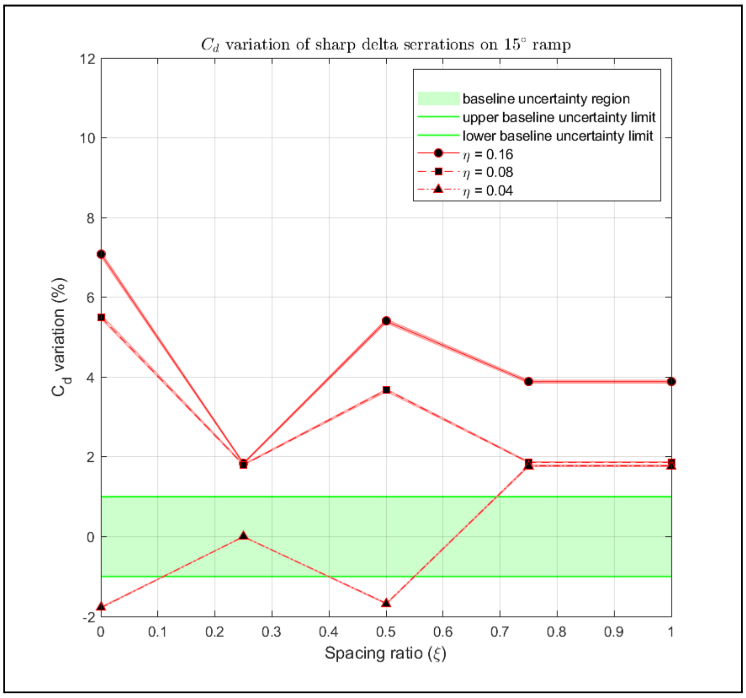

E-2: The double delta devices on 15° ramp

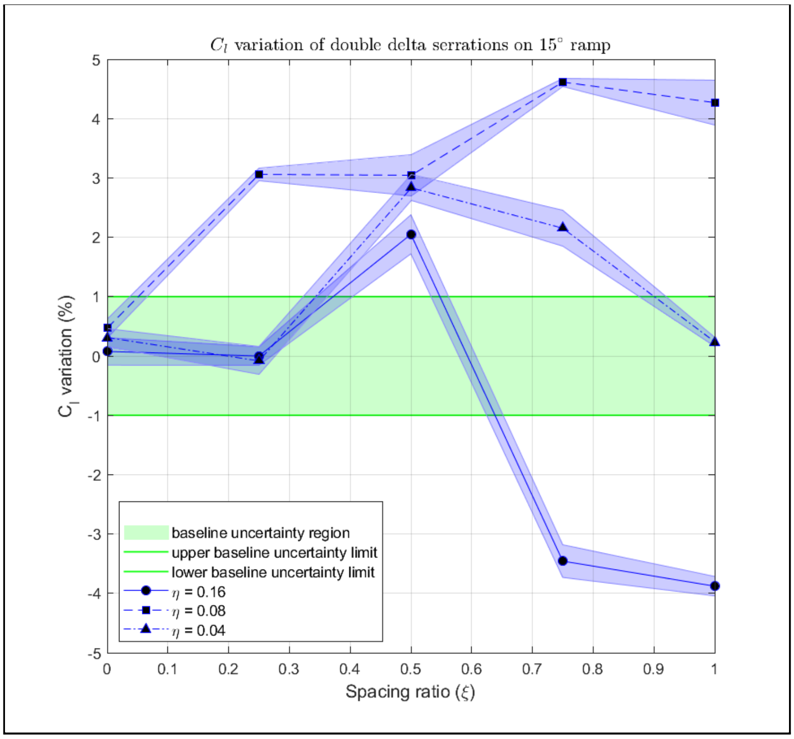

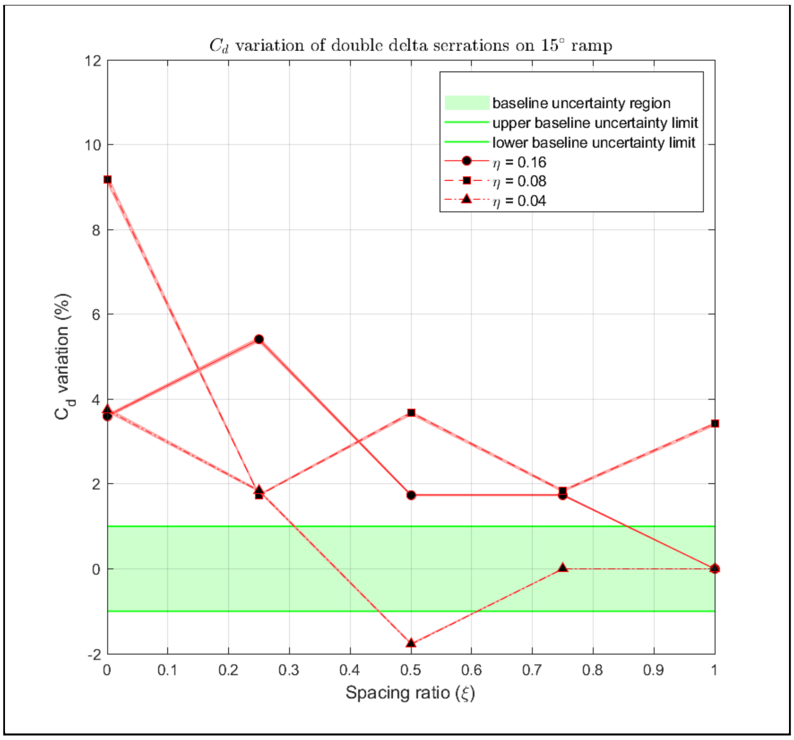

E-3: The divergent delta devices on 15° ramp

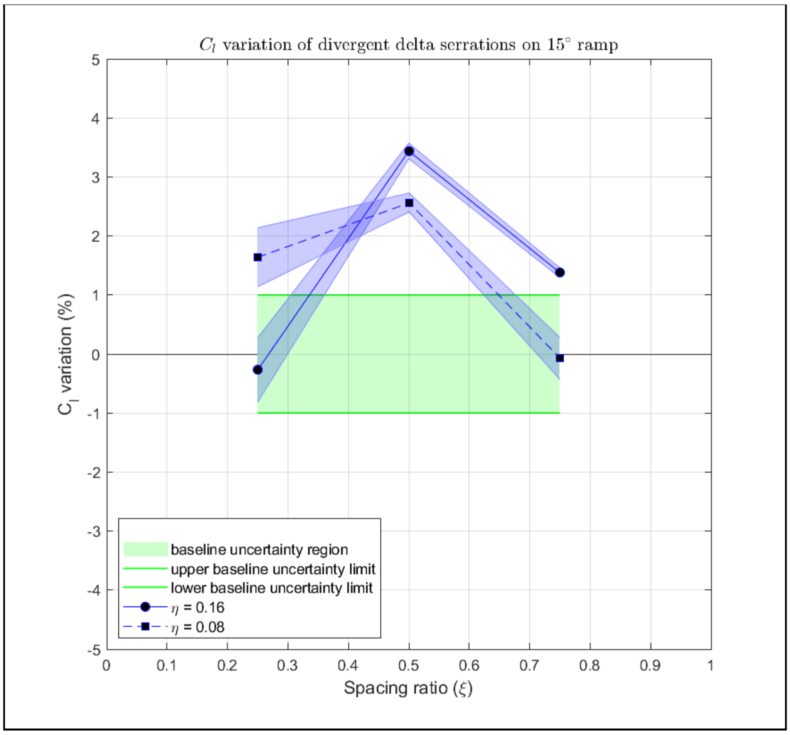

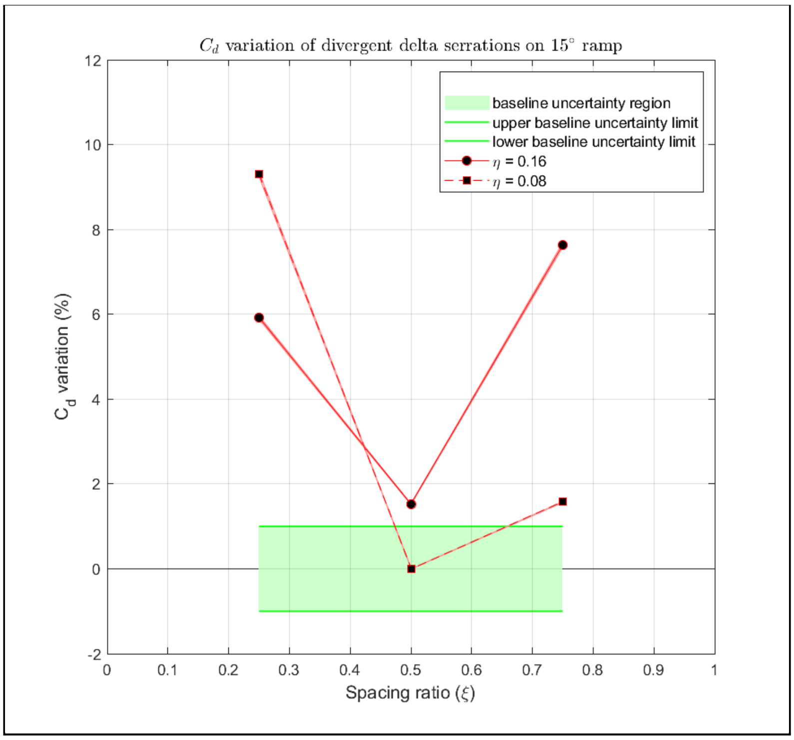

E-4: The sharp delta devices on 30° ramp

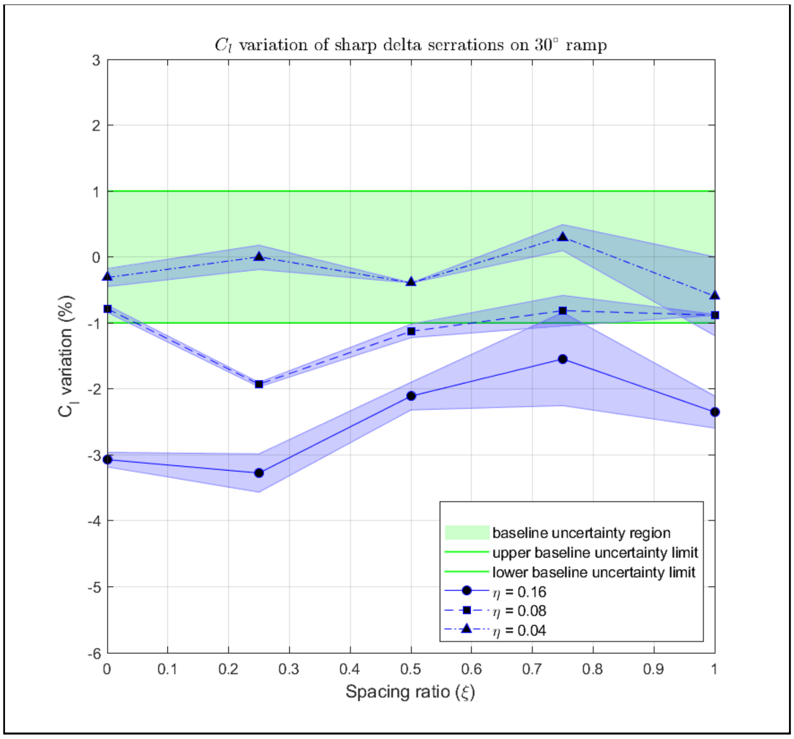

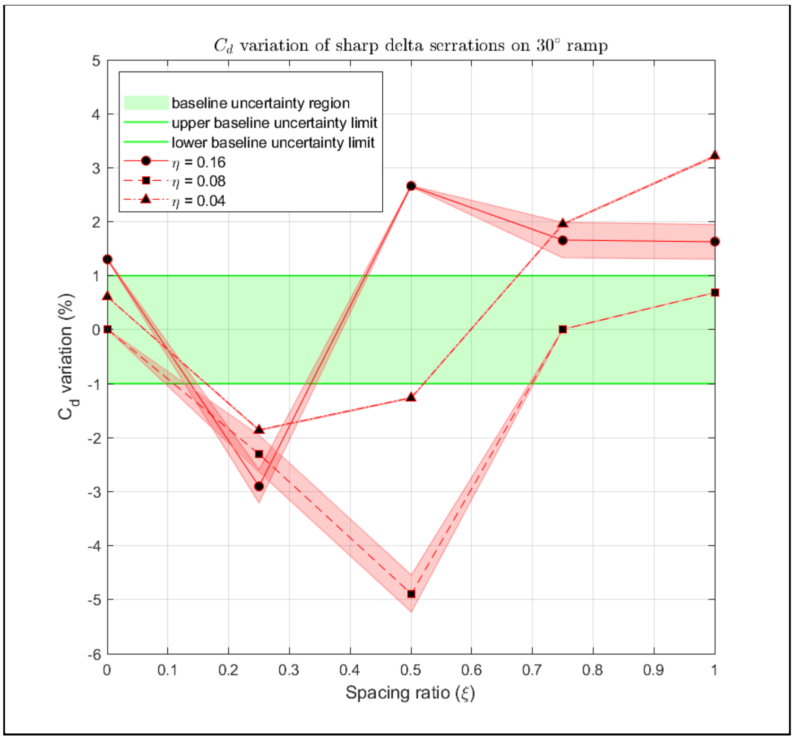

E-5: The double delta devices on 30° ramp

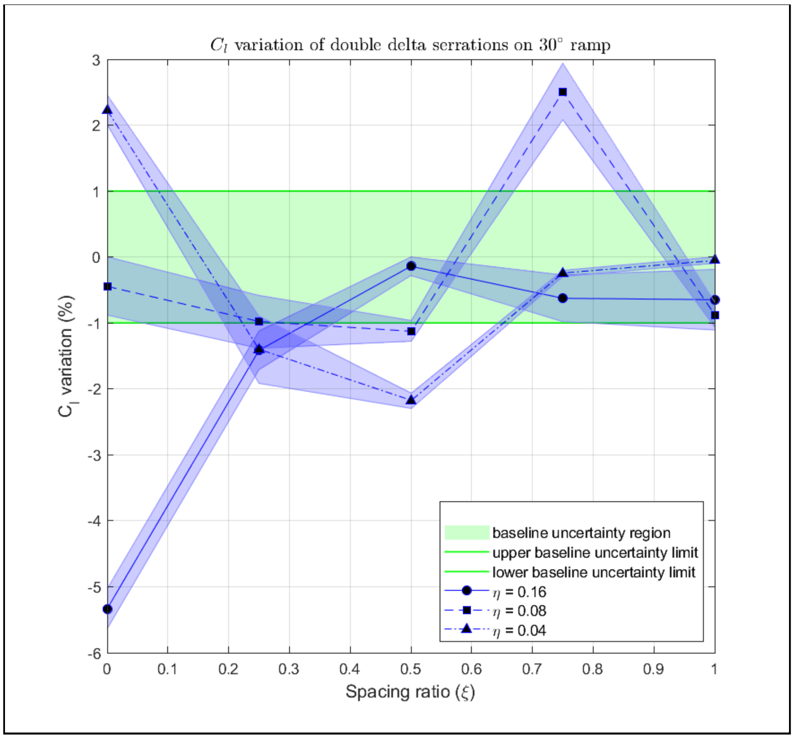

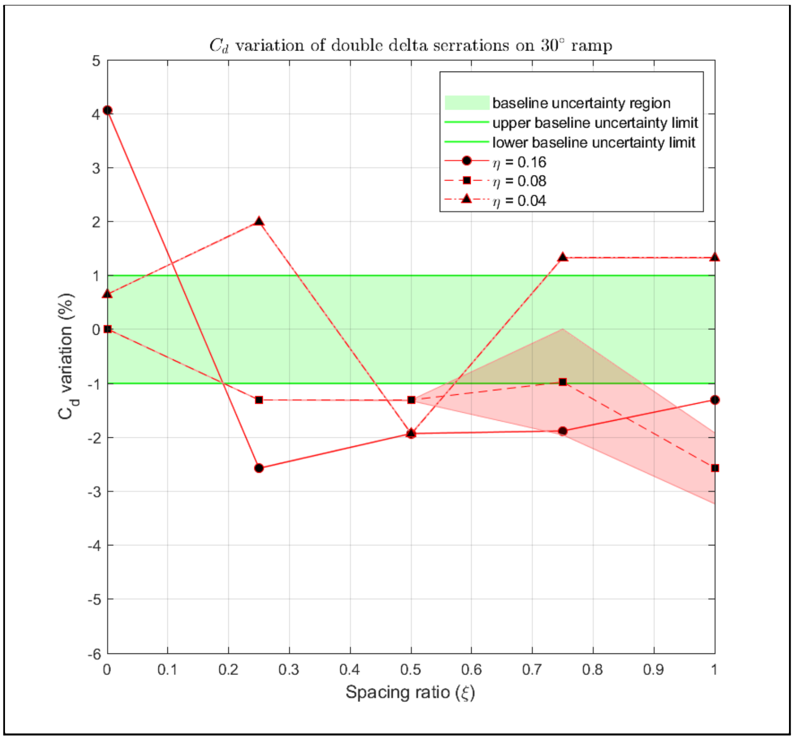

E-6: The divergent delta devices on 30° ramp

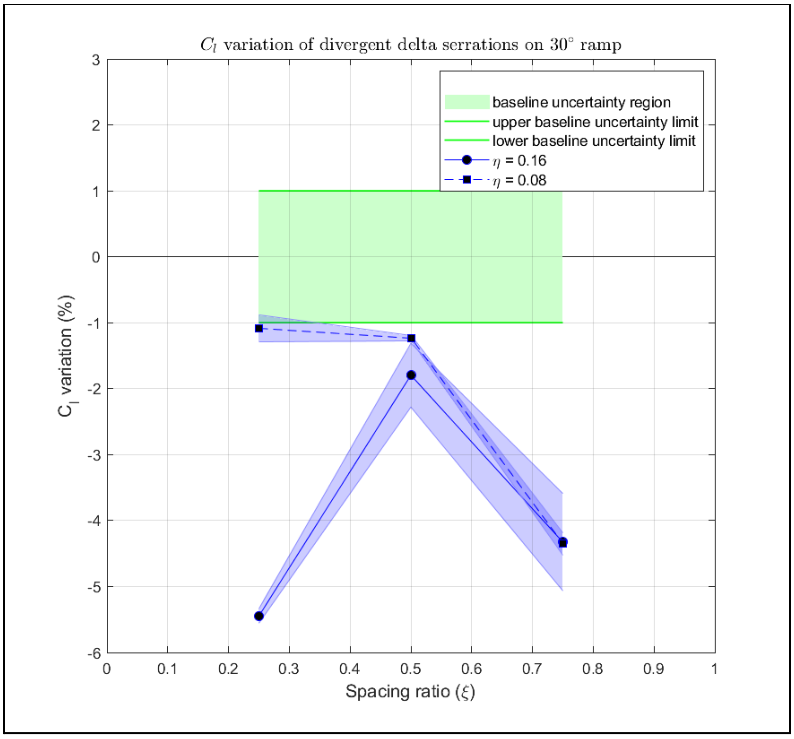

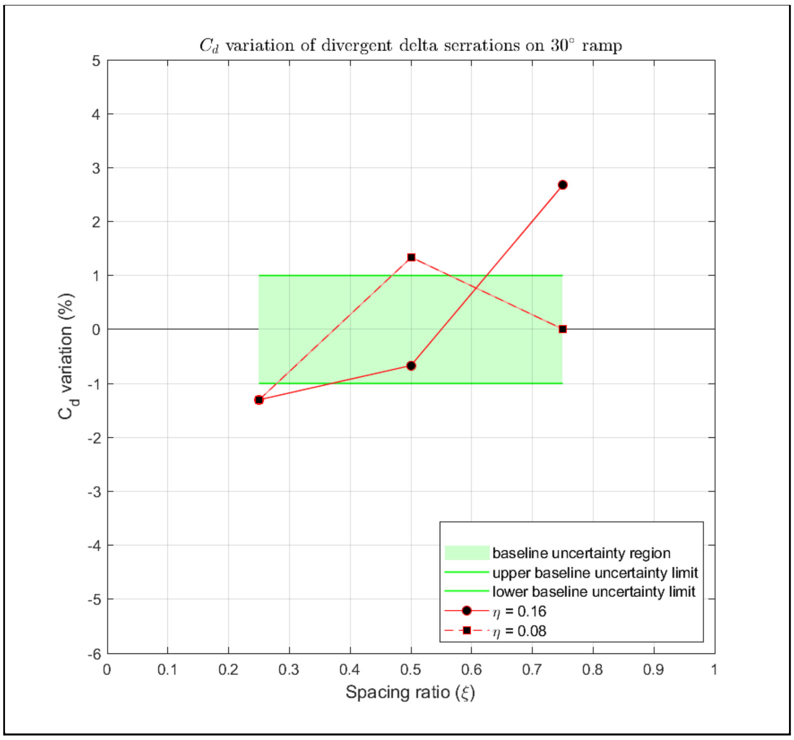

E-7: The divergent delta devices on 15° ramp with partitioning plates

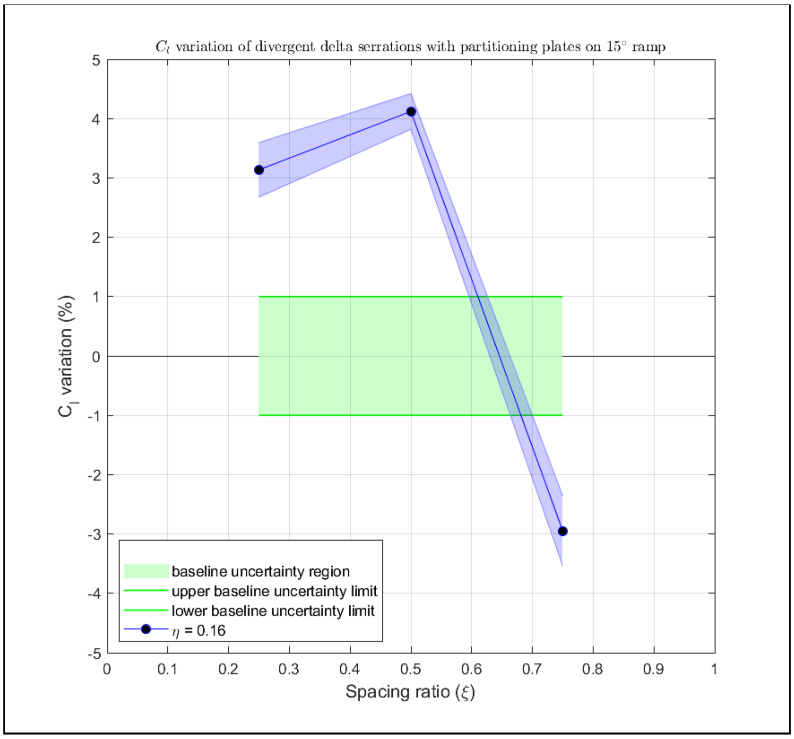

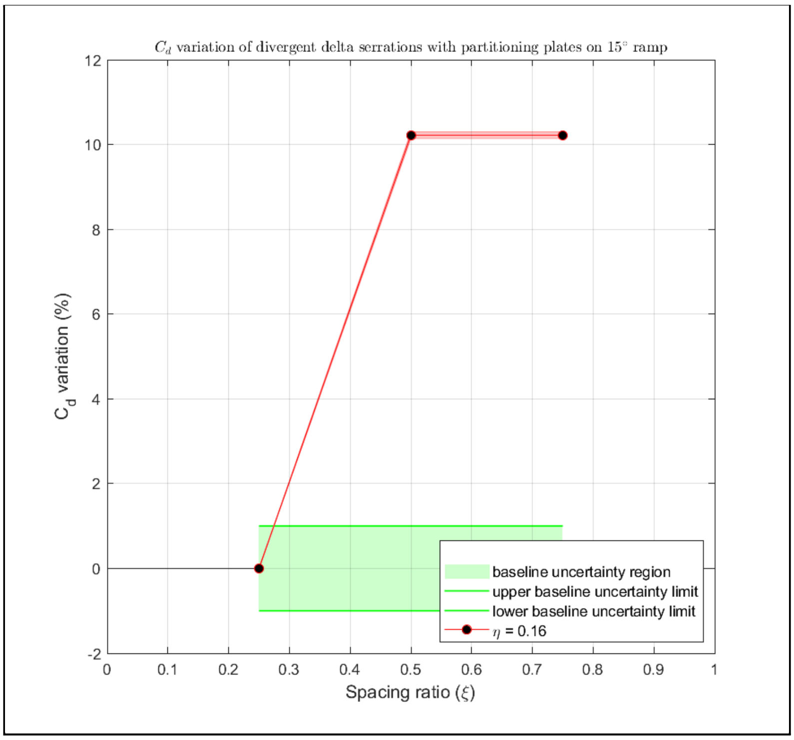

E-8: The sharp delta devices on 15° ramp with tip treatments